A Methodology to Predict the Impact Behavior of Automotive Components made of Carbon Fiber/Epoxy Composite

A thesis submitted in partial fulfillment
of the requirements for the degree of
Doctor of Philosophy

by

Ravin Garg

Politecnico di Torino

2021

33rd Cycle

Supervisors: Prof. Giovanni Belingardi and Prof. Davide Paolino (PoliTo)

Additional Supervisor: Lucio Cascone (CRF)

Abstract

Fiber reinforced polymers (FRPs) are known to have tailorable and superior mechanical properties as compared to metals and can, therefore, be used to construct components with equal or better performance at a lower mass. This has led to their increased use in the automotive industry as vehicle manufacturers rush to comply with stricter emission norms. Composite materials can also be used to manufacture primary crash structures such as crash boxes that absorb energy in case of crash preventing it from being transmitted to the passengers on account of their superior specific energy absorption capabilities. However, the lack of standardization of testing protocols and efficient predictive capability amongst the upper levels of the building block approach hampered their integration into these primary crash structures. Although, numerical capabilities do exist they require either a trial-and-error approach in calibrating the numerical model or an analytical approach, which are expensive, time consuming and subjective. Subjectivity of analytical approaches is limited to the assumptions and can be eliminated if the same set of assumptions are followed between different approaches. Off-late optimization techniques have gained traction, but calibration of the numerical model is limited to certain parameters of the force-displacement curve and not its entirety. Additionally, calibrations conducted with optimizations have only shown limited predictive capability for large scale composite components.

This dissertation presents a numerical methodology that takes advantage of element level crashworthiness tests, finite element analysis and parametric optimization to predict component level damage automatically and efficiently. Element level crashworthiness tests were performed by impacting flat composite plates made of carbon-fiber reinforced epoxy material (GG630T-37 2x2 twill) in the in-plane direction in collaboration with another researcher within the same group in order to obtain information about the crashworthiness properties of the material, hence widening the quality of experimental data beyond characterization tests that are typically performed. A new anti-buckling fixture that can be seamlessly integrated with the impact testing machines developed by Instron was designed with the use of finite element analysis, which was used to test the aforementioned flat composite plates. The effects of various design parameters such as unsupported heights and anti-buckling column diameters and distances were studied as a part of the design process of the fixture. Additionally, the impactor thickness was optimized in order to avoid any plastic deformation at the maximum energy level of 1800 J of the Instron testing apparatus. The robustness of the fixture under this energy level was also studied by numerically testing a specimen of the same material with the maximum allowable thickness. The fixture was designed to address some of the major deficiencies of the ones designed previously and reported in literature, such as inabilities to: test specimen with different thicknesses and unsupported heights, initiate frond formation or allow multiple failure modes, test specimens with dimensions equal to those of specimens used for compression after impact tests and to conduct testing with ease.

Macroscale and mesoscale models were developed to ensure methodologies provided the required information quickly and in detail, respectively, for use in both the industry and academia. Entire force-displacement curves

obtained from the tests conducted on composite flat plates were used to calibrate numerical models, especially the material card, using the HyperWorks suite. Calibrations were performed through the use of two parametric optimization techniques and response functions each. The optimization algorithms and response functions were compared to arrive at the most accurate and robust combination. Optimizations were conducted for three numerical parameters, values of which could not be obtained directly from typical crashworthiness tests. The resulting virtual model was able to predict, both qualitatively and quantitatively, the crushing behavior of a Formula SAE crash box impacted at 9700J under a drop tower. Macroscale and mesoscale models were, both, able to predict the mean crush force, stroke displacement and energy absorbed within 10% of the experimental results and accurately predict the post-impact damage. The use of automated optimization techniques significantly reduced the model calibration time. The resulting timesaving combined with the predictive capability could speed up the implementation of composite materials for use in primary crash structures by reducing component level testing. This would help automakers reduce the mass of future vehicles making them safer and more environment friendly.

Keywords: crashworthiness; impact behavior prediction; automated parametric identification; composite materials; finite element analysis

Dedicated to my beloved parents, dear wife and lovely sister who have always supported and inspired me through every step of the way.

Acknowledgements

I wish to express my deepest gratitude to my supervisors, Prof. Giovanni Belingardi and Prof. Davide Salvatore Paolino, who have guided me through the last three years and provided their sincere and invaluable technical advice. Their guidance was key towards the successful completion of this dissertation. I would, also, like to thank Lucio Cascone for his unflinching support and motivation throughout these years. His mentorship was key not just to this research, but also towards my professional development. I would like to acknowledge the support of Francesco Russo and the team at Altair Italy for their support in helping me understand their tools. I would like to thank Dr. Andrea Calzolari and Dr. Giuseppe Galizia for opening the doors for the collaboration with Instron to develop the fixture and supporting us in whichever way possible towards the successful design of the same and beyond.

I owe gratitude to all my professors, teachers and colleagues thus far. I thank Iman Babaei for all the discussions we had, for his friendship and the synergies we developed to bring justice to this research. I thank everyone who was involved with this project at Centro Ricerche Fiat, Politecnico di Torino, DLR Stuttgart, University of Patras and Instron for their contributions and assistance.

This research was, in part, carried out within the framework of the ICONIC project funded by European Union's Horizon 2020 research and innovation program under the Marie Skłodowska-Curie grant number 721256. I thank all the people involved with this project and their insights during the meetings, workshops and seminars.

Table of Contents

Abstract ii

Acknowledgements v

Table of Contents vi

List of Tables ix

List of Figures x

List of Abbreviations xiii

List of Notations xv

Superscripts xv

Subscripts xv

1. Introduction 1

1.1. Background 1

1.2. Objectives and aims 4

1.3. Thesis outline 4

2. Literature Review 6

2.1. Composite failure under crushing 6

2.2. Anti-buckling fixtures 10

2.3. Modelling of impact behavior 16

3. Numerical Modelling 25

3.1. Overview of the fixture design 25

3.2. Numerical models 26

3.2.1. Flat-plate model 26

3.2.1.1. Mesoscale model 30

3.2.1.2. Trigger design 31

3.2.1.3. Mesh dependency 32

3.2.2. Impact attenuator model 33

3.2.2.1. Macroscale model 34

3.2.2.2. Mesoscale model 36

3.3. Material cards 37

3.3.1. Law 2 – Johnson-cook elastoplastic 37
3.3.2. Law 1 – Hooke's elastic (simplified law 2) 38
3.3.3. Law 25 – Composite shell (CRASURV formulation) 39
3.3.3.1. Calibration and validation of physical parameters 48
3.3.4. Law 59 – Cohesive material 50
3.4. Property cards 51
3.4.1. Property type 1 (shells) – for metallic components 51
3.4.2. Property type 11 (shell sandwich) – for composite components 53
3.5. Contact modelling 54
3.5.1. Type 7 (node-to-element) 55
3.5.2. Type 19 (node-to-element and edge-to-edge) 59
3.5.3. Type 24 (surface-to-surface) 59
4. Fixture Design 61
4.1. Identification of the thickness of the top plate 61
4.2. Identification of the parameters relating to the anti-buckling columns 62
4.2.1. Column spacing 62
4.2.2. Column diameter 65
4.2.3. Unsupported height 67
4.3. Assessment of the robustness of the fixture 68
5. Material Card Calibration 70
5.1. Overview of the calibration setup 71
5.2. Comparison of response objectives 76
5.3. Comparison of optimization algorithms 78
5.4. Determination of the tensile formulation for the composite material 80
5.5. Determination of the contact stiffness combination 82
5.6. Final optimization run 84
6. Validation of Modelling Methodology 90
6.1. Activation of $Inacti$ flag 91
6.2. Activation of the AMS flag 92
6.3. Numerical prediction comparison with experimental results 94

7. Conclusions and Outlook 102
8. References 105
9. Appendix 113
9.1. Comparison between calibrated and uncalibrated flat-plate macroscale model 113
9.2. Impact attenuator force-displacement results at all impact velocities 113

List of Tables

Table 2.1: Crushing modes as defined by Farley, Jones and Hull (30) (31) 8
Table 3.1: C40 Steel material parameters and properties for Johnson-Cook Elastoplastic material card (102) 38
Table 3.2: C40 Steel material parameters and properties for Elastic material card (102) 39
Table 3.3: GG630T-37 Carbon Fiber Epoxy setup parameters for the composite material card..... 42
Table 3.4: GG630T-37 Carbon Fiber Epoxy elastic material properties and parameters for the composite material card..... 44
Table 3.5: GG630T-37 Carbon Fiber Epoxy plastic material properties and parameters for the composite material card..... 45
Table 3.6: GG630T-37 Carbon Fiber Epoxy softening material properties and parameters for the composite material card..... 47
Table 3.7: GG630T-37 Carbon Fiber Epoxy failure material properties and parameters for the composite material card..... 48
Table 3.8: Cohesive material and failure parameters and properties 51
Table 3.9: Property type 1 (metals) parameters and inputs..... 52
Table 3.10: Property type 11 (composites) parameters and inputs 53
Table 3.11: Contact types used for the models 55
Table 3.12: Input parameters, their determination and input values for type 7 contacts 57
Table 4.1: List of final parameters for the fixture design..... 67
Table 5.1: Convergence limits for ARSM technique..... 73
Table 5.2: Comparison of available algorithms according to their advantages, disadvantages, accuracy and efficiency (126) 75
Table 5.3: Comparison of post-optimization variable and response values..... 77
Table 5.4: Comparison of the different contact stiffness formulation combinations based on their respective damage behavior and an overview of the cases selcted to be optimized 83
Table 5.5: Optimal values of all four parameters for both the approaches 86
Table 5.6: Correlations between the optimized parameters and the response values 87
Table 6.1: Impact velocity and energy levels..... 90
Table 6.2: Displacement and mean crush force prediction comparison of numerical values with experimental results for the impact attenuator..... 97

List of Figures

Figure 1.1: Composite components in vehicles: chassis (a, b) and other small components (c) (10) (11) (12) 2
Figure 1.2: Metallic crash box of a car (circled in red) (13) 2
Figure 1.3: Building block approach as described by Rouchon (17) 3
Figure 2.1: Typical force-displacement graph upon impact on composite materials 6
Figure 2.2: Damage after frontal crash test conducted by Euro New Car Assessment Program (29) 7
Figure 2.3: Crushing modes as described by Farley and Jones: transverse shearing/fragmentation (a), brittle fracturing (b), lamina bending/splaying (c), and buckling (d) (30) 9
Figure 2.4: Debris wedge (34) 10
Figure 2.5: Self-supporting composite geometries – a: square (38), b: circular (38), c: sinusoidal (24), d: c-shaped (39), e: angular (40), f: omega (27) 11
Figure 2.6: First ever anti-buckling fixture to test flat composite plates; Developed at NASA (41) 12
Figure 2.7: Anti-buckling fixture developed at University of London (44) 13
Figure 2.8: Fixture developed at University of Tennessee (a); Constrain and failure propagation profile of the fixture (b); Specimen after impact (c) (45) (46) 13
Figure 2.9: Fixture developed by Engenuity (21) (a); Illustration of unsupported height (b) 14
Figure 2.10: Feraboli fixture (41) 15
Figure 2.11: Testing jig at Swerea SICOMP for small composite coupon crashworthiness testing (49) 15
Figure 2.12: A 2D (a) and 3D (b) RVE (51) 17
Figure 2.13: Finite element model made of shell and spring (a) elements and shell and solid (b) elements; stacked shell approach (c) (64) (65) (27) 18
Figure 2.14: Non-homogeneous mesoscale modelling of WF composites (69) 18
Figure 2.15: In- (a) and out-of-plane (b) impact tests (27) (81) 21
Figure 2.16: Numerical trigger introduced by DLR (a) (87), SAE filter applied to raw simulation data by Feraboli et al. (b) (21) (24) 22
Figure 3.1: Final design iteration of the anti-buckling fixture 26
Figure 3.2: Cuboidal (a) and rectangular (b) impactors 27
Figure 3.3: Mesh refinement for the top plate 28
Figure 3.4: First iteration of numerical flat-plate model (used to optimize the top plate thickness) 28
Figure 3.5: Top plate numerical model 29
Figure 3.6: Cross-section of the composite flat plate (98) 30
Figure 3.7: Sawtooth trigger (a) (48); numerical boxed trigger (b); isometric view of the trigger in the macroscale model (c); isometric view of the trigger in the mesoscale model (d); bottom view of the trigger in the macroscale model 32
Figure 3.8: 2 mm mesh with a boxed trigger (a) and 2 mm mesh with a boxed trigger and node offset (b) .. 32
Figure 3.9: Comparison of force-displacement curves for two different mesh sizes with experimental results 33

Figure 3.10: CFRP impact attenuator (98) 34
Figure 3.11: Macroscale model of the impact attenuator (a); Symmetry plane for the impact attenuator (b) 35
Figure 3.12: Cross-section of the impact attenuator (98) 36
Figure 3.13: Energy absorbed failure parameter and softening with residual stress (a); softening without residual stress (b) 41
Figure 3.14: Stress-strain results of material characterization tests under tension (a) and compression loading (b) (95) 43
Figure 3.15: Stress-strain curves of material characterization tests under shear loading 44
Figure 3.16: Constrains applied to single element test elements 48
Figure 3.17: Displacements applied to single element test elements 49
Figure 3.18: Comparison of numerical and experimental characterization test results under a tensile load .. 49
Figure 3.19: Comparison of numerical and experimental characterization test results under a compressive load 50
Figure 3.20: Comparison of numerical and experimental characterization test results under a shear load 50
Figure 3.21: Illustration of slave nodes and master elements in a type 7 contact (a); Self-contact with slave nodes and masterelements on the same component (b) (113) 56
Figure 3.22: Illustration of adding an edge-to-edge contact 59
Figure 3.23: Illustration of slave and master nodes and elements in a type 24 contact (113) 59
Figure 4.1: Comparison of the deformation response of top plates with different thickness (10, 20 and 30 mm) to an 1850 J impact (48) 62
Figure 4.2: Front view of a time lapse (0, 2, 4, 6, 8 and 10 ms) comparing the response of a 4-ply thick (2.56 mm) CFRP flat plate supported by anti-buckling columns spaced at three different distances (50 (left), 65 (center) and 80 (right) mm) to a 550 J impact 64
Figure 4.3: Side view of a time lapse (0, 2, 4, 6, 8 and 10 ms) comparing the response of a 4-ply thick (2.56 mm) CFRP flat plate supported by anti-buckling columns spaced at three different distances (50 (left), 65 (center) and 80 (right) mm) to a 550 J impact 65
Figure 4.4: Time lapse (0, 2, 4, 6, 8 and 10 ms) comparing the response of a 4-ply thick (2.56 mm) CFRP flat plate supported by anti-buckling columns of three different diameters (5 (left), 10 (center) and 20 (right) mm) to a 550 J impact 66
Figure 4.5: Force-displacement curve comparison of a 4-ply thick (2.56 mm) CFRP flat plate impacted at 550 J supported by anti-buckling columns placed at different unsupported heights (5, 10, 20 and 30 mm) (48) 68
Figure 4.6: Time lapse (0, 2, 3.5, 4 and 5 ms) comparing the response of a 24-ply thick (15.36 mm) CFRP flat plate to an 1850 J impact from the front (left) and side (right) views 69
Figure 5.1: Overview of the calibration approach with GRSM optimization algorithm 76
Figure 5.2: Comparison of the experimental force-displacement curve with those obtained from optimized runs with the squared and absolute difference response objectives 77

Figure 5.3: Comparison of the ADMF values for all iterations of the optimization approach for the absolute and squared difference response functions 78
Figure 5.4: Comparison of the experimental force-displacement curve with those obtained from optimized runs with the GRSM and ARSM algorithms 79
Figure 5.5: Response values for different runs using GRSM (a) and ARSM (b) algorithms 80
Figure 5.6: Side-view comparison of final damage using the elastoplastic and purely elastic tensile formulation 81
Figure 5.7: Force-displacement comparison of the two tensile formulation 82
Figure 5.8: Post-calibration comparison of the E, F and G cases (side-view) 84
Figure 5.9: Comparison of the experimental force-displacement curve with the final optimization runs for the macroscale and mesoscale approach (98) 85
Figure 5.10: Progression of the variables for the macroscale and mesoscale approaches 86
Figure 5.11: Time-lapse comparison of the macroscale and mesoscale models (side view) 88
Figure 5.12: View from the bottom of the final plastic strains observed in the macroscale and mesoscale models 88
Figure 5.13: Comparison of the fronding observed in the mesoscale model with that observed in the experiments (98) 89
Figure 6.1: Final damage of the impact attenuators at all four impact velocities 90
Figure 6.2: Effect of the activation of the $Inacti$ flag 92
Figure 6.3: Time step for the macroscale and mesoscale (with and without AMS flag activation) models 93
Figure 6.4: Qualitative comparison of the impact attenuator final damage with and without activation of the AMS flag 94
Figure 6.5: Force-displacement result comparison at 7.097 m/s impact velocity 95
Figure 6.6: Comparison of final damage using the macroscale (a) and mesoscale (with AMS) (b) approaches at all four energy levels 100
Figure 6.7: Time lapse of damage progression for the numerical macroscale and mesoscale (complete model and cohesive elements only both with AMS) models at an impact velocity of 8.04 m/s 101
Figure 9.1: Force-displacement data comparison of calibrated and uncalibrated flat-plate macroscale model with experimental results 113
Figure 9.2: Force-displacement result comparison at 7.101 m/s impact velocity 114
Figure 9.3: Force-displacement result comparison at 7.77 m/s impact velocity 114
Figure 9.4: Force-displacement result comparison at 8.04 m/s impact velocity 115

List of Abbreviations

1D	:	One-Dimensional
2D	:	Two-Dimensional
3D	:	Three-Dimensional
ADMF	:	Average Deviation from Experimental Mean Force
AMS	:	Advanced Mass Scaling
ASTM	:	American Society for Testing and Materials
ARSM	:	Adaptive Response Surface Methodology
BBA	:	Building Block Approach
CAI	:	Compression After Impact
CFRP	:	Carbon-Fiber Reinforced Polymer(ic)(s)
CLT	:	Classical Laminate Theory
CRASURV	:	Commercial Aircraft – Design for Crash Survivability
CRF	:	Centro Ricerche Fiat
DLR	:	Deutsches Zentrum für Luft- und Raumfahrt e.V. (German Aerospace Center)
DCB	:	Double Cantilever Beam
DoF(s)	:	Degree(s) of Freedom
EA	:	Energy Absorbed
EAL	:	Engineering Analysis Language
ENF	:	End Notched Flexural Beam
EU	:	European Union
F1	:	Formula 1
FCA	:	Fiat Chrysler Automobiles
FEA	:	Finite Element Analysis
FRP	:	Fiber-Reinforced Polymer(ic)(s)
GA	:	Genetic Algorithm
GFRP	:	Glass-Fiber Reinforced Polymer(ic)(s)
GHG	:	Greenhouse Gas(es)
GRSM	:	Global Response Surface Methodology
HPC	:	High Performance Computing
MFD	:	Method of Feasible Directions
NASA	:	National Aeronautics and Space Administration
NDT	:	Non-Destructive Testing
NOFV	:	Nominal Objective Function Value
QUB	:	Queen's University Belfast
RSM	:	Response Surface Methodology

RVE	:	Representative Volume Element(s)
SAE	:	Society of Automotive Engineers
SQP	:	Sequential Quadratic Programming
SEA	:	Specific Energy Absorption
WF	:	Woven Fabric

List of Notations

A	:	Cross-sectional Area
F	:	Force (SEA equation) or Tsai-Wu coefficients (Tsai-Wu equation)
G_{IC}	:	Mode 1 Critical Strain Energy Release Rate
G_{IIC}	:	Mode 2 Critical Strain Energy Release Rate
K, St	:	Stiffness
W	:	Plastic Work (Energy Absorbed) per unit volume
a	:	Yield Stress
b	:	Hardening Parameter
c	:	Strain-Rate Parameter
l	:	Displacement
m	:	Shape Function
t	:	Thickness
α	:	Reduction factor in Tsai-Wu equation
ε	:	Strain
ρ	:	Density
σ	:	Stress

Superscripts

c	:	Compression
m	:	Temperature Exponent
n	:	Hardening Exponent
t	:	Tension
$u\ or\ ult.$	:	Ultimate

Subscripts

0	:	Reference Strain
1 *or* 11	:	0º Direction
2 *or* 22	:	90º Direction
12 *or* 6 *or* 66	:	Shear Direction
abs	:	Absolute
f	:	Failure/Deletion (strain)
p	:	Plastic
m	:	Maximum (strain) or master segment
rel	:	Relative

rs	:	Residual Stress
s	:	Slave segment
t	:	Initial (softening strain) or time (optimization)
y	:	Yield

1. Introduction

This chapter gives a background on the need for conducting the research works covered under this dissertation. It separately mentions the objectives and aims of the same and an outline of the entire thesis.

1.1. Background

Automobiles have come a long way since their advent in 1769 by French engineer Nicolas-Joseph Cugnotand have played a crucial part in our lives since Karl Benz and the Ford Motor Company introduced the first production (1885) and mass production (1908) vehicles respectively (1) (2) (3). For all the benefits they offer and communities they have transformed, passenger vehicles contribute around 15% to global GHG emissions, which are generally considered responsible for global warming (4) (5). In light of this, the EU in 2012 decided to reduce average automotive emissions by 27% from 2015 to 2021 and using 2021 as a baseline further reduce them by 15% by 2025 and 37.5% by 2030 (6). The National Highway Traffic Safety Administration in the US also published new Corporate Average Fuel Economy regulations that require vehicle manufacturers to increase the average fuel economy to 54.5 mpg for cars and light-duty trucks by 2025 (7). Every 100 kg reduction in mass, directly or indirectly reduces fuel consumption by 0.7 liters per 100 km so in addition to electrifying and downsizing their powertrains, automotive manufacturers are optimizing assemblies and components as well (8). However, as a part of this optimization they must ensure that the vehicles they produce not just follow the safety standards prescribed by the respective national authorities but exceed them in order to curb the 1.35 million deaths that occur as a result of road traffic crashes every year across the world (9). In order to optimize structural performance, use of composite materials has been steadily increasing due to their higher specific mechanical properties and advantages such as higher impact resistance, higher energy absorption, lower noise and vibrations, manufacturability of assemblies with less subcomponents when compared with metallic materials (8). FRP composite materials are being widely used to push manufacturing innovation for components such as chassis, door, seat, beam, joint, flooring and other small components shown in Figure **1.1**.

(a)

(b)

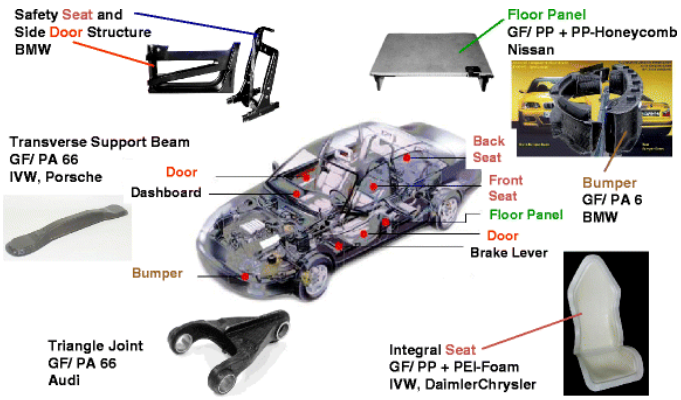

(c)

Figure 1.1: *Composite components in vehicles: chassis (a, b) and other small components (c) (10) (11) (12)*

Primary crash structures such as crash boxes, shown in Figure **1.2**, were introduced to absorb the kinetic energy of a vehicle as sacrificial components in case of a crash and prevent it from being transmitted to other parts of the vehicle structure that have higher repair costs such as the engine or even to the passengers and, potentially, hurting them.

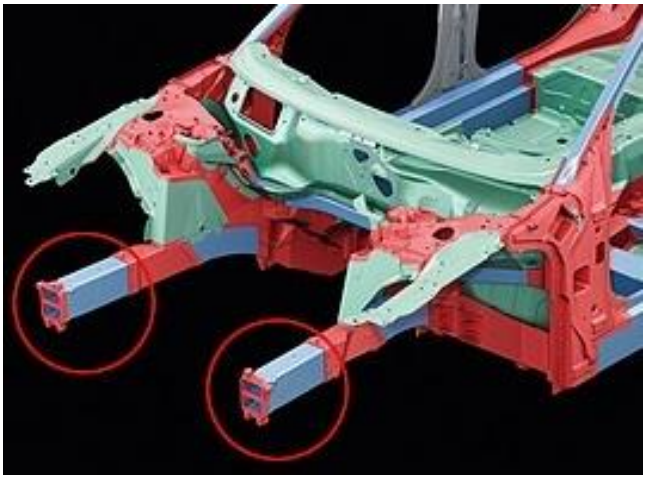

Figure 1.2: *Metallic crash box of a car (circled in red) (13)*

FRPs are known to have 6 – 8 time the specific energy absorption (SEA) capability of metals and in order to take advantage of their improved SEA capabilities primary crash structures could be made from these materials instead of metals, which have traditionally been used (14). Although, FRP composites have replaced metals as preferred materials for use in these structures in F1, the same has not occurred for mass production vehicles, due to the costs and resources involved, factors which are not the primary concern in F1. It is already known from F1 that the use of composite materials for crash boxes significantly reduced driver fatality and injuries in case of a crash (15). Since BMW pioneered the use of FRPs in the automobile industry in the i3 cars in 2013, not many manufacturers have followed suite at an equivalent scale (16). With the exception of Lexus LFA, which has some frontal crash components made of carbon-fiber reinforced polymers (CFRP), other high-end cars such as Alfa Romeo 8C, Alfa Romeo 4C, McLaren 12C, Lamborghini Aventador and Bugatti Veyron only use these materials sparingly for frontal primary crash structures but use them extensively for other structures that enhance passenger safety such as monocoques, underbodies etc. (16). Use of FRP composites

in future vehicles would not only make them safer for travel, but also reduce their mass and, subsequently, fuel consumption and emissions.

Availability of resources in F1 permit F1 teams to test FRP composites along the entire chain of the building block approach (BBA): from coupons, to component, to assemblies and finally through to full-scale testing. The BBA was suggested by Rouchon (17). It entails a pyramid approach that starts with tests on small coupons used for material characterization that eventually led to full-scale tests, with each level of the pyramid testing considerably fewer parts.

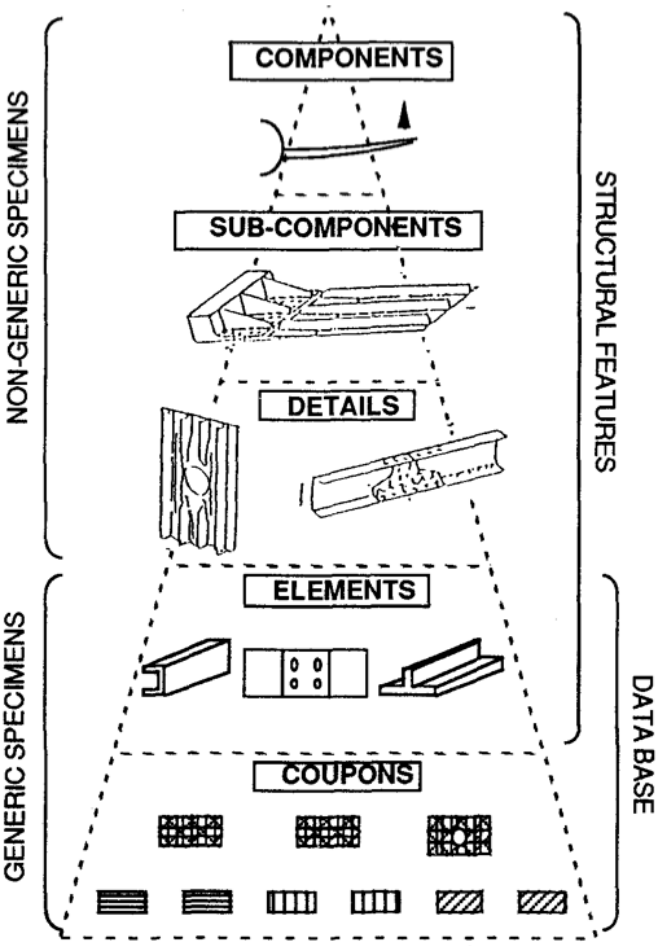

Figure 1.3: *Building block approach as described by Rouchon (17)*

The approach was designed keeping in mind the aerospace industry, which at the time was increasingly using composite materials. Although the approach provides for analyzing and mitigating risks, in order to do so extensive testing needs to be conducted. Following the approach for integration of composite materials was not possible for mass production vehicles due to the time and monetary restrictions involved and following the budgetary and time constrains lead to restriction of the design space, which further hampered the integration of composite materials into crash structures (18). Additionally, use of composite materials in critical components comes with large safety margins as compared to those used for metallic materials due to the lack of predictive capability of their failure behavior (18). Hence, a part of the process needed to be conducted virtually in a way that information available from lower-level physical testing can aid prediction of middle

level components and assemblies by the use of numerical tools. This is akin to creating a “digital-twin” on which “virtual testing” is conducted. Results obtained from this prediction could be used to design full-scale models, saving resources, time and money, spent on testing, thereby allowing faster implementation of composite materials in primary crash structures. Moreover, doing so results in an expansion of the design space as more permutations and combinations of different material systems and topographies can be conducted with less resources, which can help develop superior products. Published studies have already shown that numerical analysis can simulate damage of components and assemblies, but the analysis involves a trial-and-error approach in calibrating the material card and other numerical parameters, which is neither accurate nor efficient (19) (20) (21) (22) (23) (24) (25). Analytical models have also been tested, but they require significant amounts of experimental data, which can only be obtained from an exhaustive experimental campaign, thereby reducing efficiency (26). Therefore, there existed a need for a methodology that replaced parts of the BBA with numerical analysis that worked in conjunction with a simplified experimental campaign and could automate and predict the response of composite crash structures for use in the automotive industry.

1.2. Objectives and aims

The objective of this thesis was to fill the above-mentioned gaps in prediction of composite component behavior to enable faster implementation of composite materials in the automotive industry by developing a methodology that can be used universally to automatically calibrate numerical models that can predict composite crash behavior at component levels, in the hope of pushing towards a standardized procedure. The aim was to first assess the published methodologies currently being used in the industry and assess areas of improvement in the same. Post-assessment, a need was felt for an anti-buckling fixture that could test flat composite plates to provide critical material crashworthiness information not available from standardized coupon tests. The same was to be developed to support the numerical methodology in calibrating numerical parameters. The numerical methodology hence developed would be able to predict crush behavior of primary and secondary composite crash components. Ultimately, the methodology developed was to be validated both qualitatively and quantitatively using the available experimental data.

1.3. Thesis outline

A summary of the subsequent chapters is as follows.

Chapter 2 goes over the published literature and its review and is divided into three parts. The first part goes over the energy absorption capabilities and failure modes of composite materials under axial impact conditions. This is followed by an overview of the state-of-the-art anti-buckling fixtures that are currently in use to test flat composite plates. The chapter ends by going over various modelling and numerical methodologies that either model or predict the crash behavior of composite components.

Chapter 3 provides a detailed description of the numerical processes involved. It describes the material and property laws used to define various components and the procedures used to populate the parameters within these models. It also explains the contact modelling between these components and the determination of the

final contact model used. Additionally, it explains the integration of cohesive models in order to model the crush behavior using both the macroscale and mesoscale approach.

Chapter 4 highlights the numerical analysis conducted to design an anti-buckling fixture developed to aid the numerical methodology. It provides information on the optimizations conducted to obtain and assess the effect different impactor thicknesses, anti-buckling column distances, diameters and unsupported heights. It also showcases the robustness of the developed fixture. The chapter also presents the boundary conditions used for each case.

In Chapter 5, the optimization procedure followed to automate the material card calibration is presented. It details and compares the optimization algorithms and response functions that were available and used for both the macroscale and mesoscale approach. It details the optimization procedure, bounds and target parameters and explains the correlation between input variables and the output response. Boundary conditions used for the simulations and their respective run times are also highlighted.

In Chapter 6, the calibrated material model obtained is used to predict the impact behavior of a Formula SAE crash box and the results are then compared with the available experimental data to validate the modelling methodology. The process is done for both the macroscale and mesoscale approaches. Boundary conditions and model specific information are also provided.

Chapter 7 concludes the dissertation by summarizing the methodology and results and also presents its applications. It highlights its limitations and presents an outlook for further research that can be conducted to make the methodology more robust.

2. Literature Review

This chapter presents an overview relevant literature of the topics covered in this dissertation. It goes over the basics of composite crushing behavior and the related failure modes before delving into the description and limitations of anti-buckling fixtures that have been used thus far for conducting testing on flat composite coupons. Finally, it presents the modelling methodologies used to model composite crush behavior and presents the state-of-the-art numerical methodologies that have been developed to predict composite crush behavior.

2.1. Composite failure under crushing

Due to their anisotropic nature, composite materials absorb energy through a variety of failure modes and their energy absorption behavior can be assessed both quantitatively and qualitatively. Qualitative analysis is conducted by visually inspecting, through use of instruments or through the naked eye, the damage during and after the impact, whilst quantitative analysis is conducted by analyzing the force-displacement curve and information derived thereof, such as peak force, mean crush force, stroke displacement, EA and SEA. Peak force is the force obtained as a result of crush initiation, or alternatively the force required to initiate crushing, whilst the mean crush force is the force obtained during the progressive crushing phase. These parameters allow comparison of energy absorption capabilities of different materials and geometries. Figure **2.1** below shows a typical force-displacement curve upon impact. Energy absorbed is the area under the graph, while SEA is calculated by dividing the energy absorbed by the mass of crushed region as shown from Equations 2.1 and 2.2 below.

$$EA = \int F \, dl \tag{2.1}$$

$$SEA = \frac{EA}{\rho \, A \, l} \tag{2.2}$$

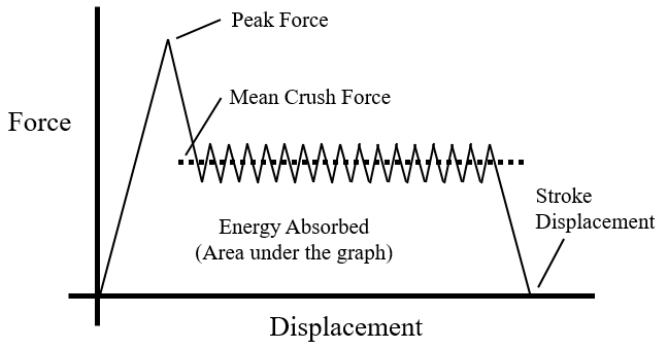

Figure 2.1: *Typical force-displacement graph upon impact on composite materials*

Composite materials absorb energy either through catastrophic or progressive failure during crushing. Catastrophic crushing results in a very high peak force until which the material is able to take the load followed by a sudden drop in the force as a result of a break in the material. Progressive failure results in the material

being damaged gradually. The peak force is lower for progressive crushing as compared to a catastrophic failure and is followed by a force plateau, during which most of the energy is absorbed, before it approaches zero. A progressive crush is desired in crash scenarios such as the ones shown in Figure **2.2** as it leads to lower force being transmitted to the passengers and more energy being absorbed. Peak force for an ideal crash absorber equals the mean crush force, to lessen the immediate impact (impulse) on the passengers (27). Progressive crushing leads to the formation of the crush front, a localized area where the crushing progressively takes place that gradually moves along the length of the structure being crushed. Depending on several factors, the crash front for a composite structure might exhibit only fragmentation or splaying, or a mix of both, which are entirely different energy absorbing mechanisms than the plastic folding observed during crushing of metallic structures. A trigger mechanism is typically added to the part of the structure that is expected to first experience the impact in order to reduce the peak force and initiate progressive crushing. Regulations dictate the length and level of the mean crush force in terms of time and gravitational units, respectively, to ensure an acceptable level of deceleration for the passengers (28).

Figure 2.2: *Damage after frontal crash test conducted by Euro New Car Assessment Program (29)*

Efficiency of crushing can be adjudged by the crushing mode of the composite coupon or component (30). Farley and Jones, in their pioneering work, described four crushing modes: transverse shearing, brittle fracturing, lamina bending and local buckling. Hull categorized transverse shearing as fragmentation and lamina bending as splaying (31). These modes typically occur as a combination during crushing and are a function of the material properties and coupon/component geometry. They are described in Table **2.1** and shown in Figure **2.3**.

Table 2.1: *Crushing modes as defined by Farley, Jones and Hull (30) (31)*

Crushing Mode	Failure Initiation	Energy Absorption	Failure Control
Transverse Shearing/Fragmentation	Short interlaminar and longitudinal cracks with lengths smaller than laminate thickness	Transverse shearing of the edges of the lamina resulting in the most efficient crushing	Lamina bundle formation as a result of the crack growth until the edge of the bundle
Brittle Fracturing	Long interlaminar and longitudinal cracks with lengths equal to several laminate thicknesses	Failure of the lamina bundles	Occurs repeatedly: Cracking leading to bundle formation followed by further cracking and so forth
Lamina Bending/Splaying	Very long interlaminar, intralaminar and parallel-to-fiber cracks with lengths greater than ten laminate thicknesses	Crack growth without failure of lamina bundles	No control: Occurs till complete energy absorption or geometry exhaustion
Local Buckling	Formation of local buckles	Plastic deformation and delaminations	Plastic deformation without fracture, interphase destruction and fiber splitting

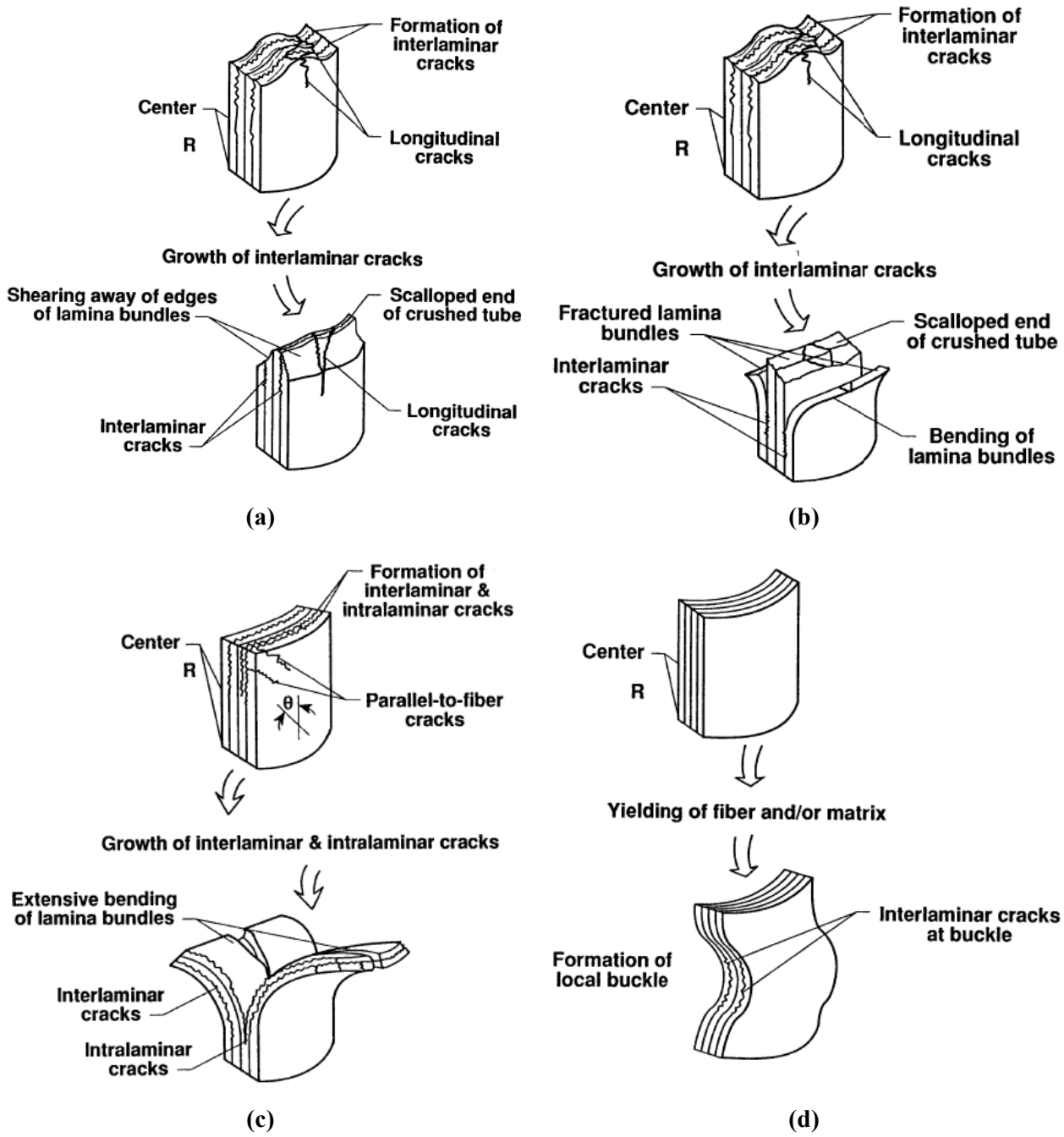

Figure 2.3: *Crushing modes as described by Farley and Jones: transverse shearing/fragmentation (a), brittle fracturing (b), lamina bending/splaying (c), and buckling (d) (30)*

These four crushing modes encompass other failure modes such as fiber breakage, matrix cracking, delamination etc. that occur during the initiation or the energy absorption phase of crushing. Delamination is caused as a result of interlaminar stresses that act on weak interlaminar connections (32). During lamina bending or splaying mode, a debris wedge, as shown in Figure **2.4**, starts to form as a result of the friction between the lamina bundle and the impactor as explained by Mamalis et al. and it exerts a force on the lamina causing them to splay on either side of the geometry (33).

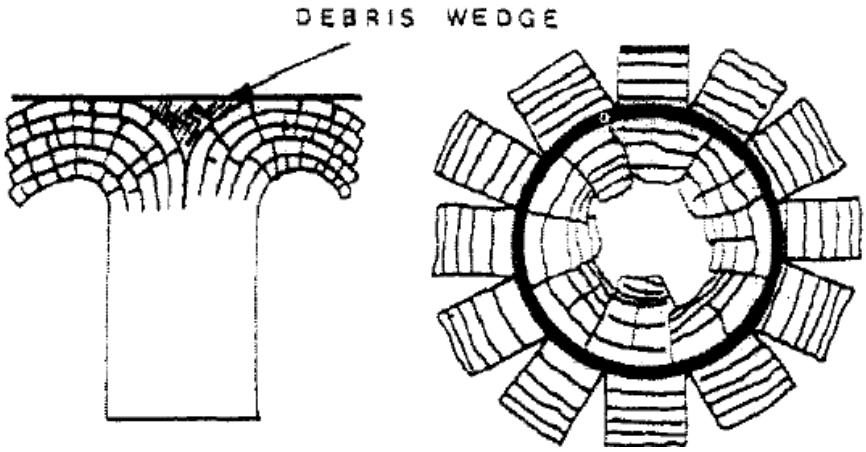

Figure 2.4: *Debris wedge (34)*

Since these initial studies, several others have been conducted to understand the effect of different trigger mechanisms (35), geometries (36), reinforcement and matrix combinations (37), and manufacturing techniques (38) on the factors affecting crushing behavior.

2.2. Anti-buckling fixtures

Integration of composite materials into larger structures such as car bodies has always followed the BBA that starts with testing of coupons and finishes with full-scale tests while passing through stages of element, component and assembly tests. Results from each stage provide critical information to help develop and design the next one. Standardized testing protocols have already been established to characterize composite materials at a coupon level by conducting tension, compression, shear, flexure etc. tests. However, at the element level no such standardized testing protocol exists for testing crashworthiness of composite materials. Self-supporting geometries such as those with square or rectangular, circular, sinusoidal, c-shaped, L-shaped, and omega cross sections, as shown in Figure **2.5**, can be tested with ease under a drop tower apparatus, as they do not need any additional supports, to understand the combined or individual influence of geometry, material and other parameters on the crashworthiness of composite structures.

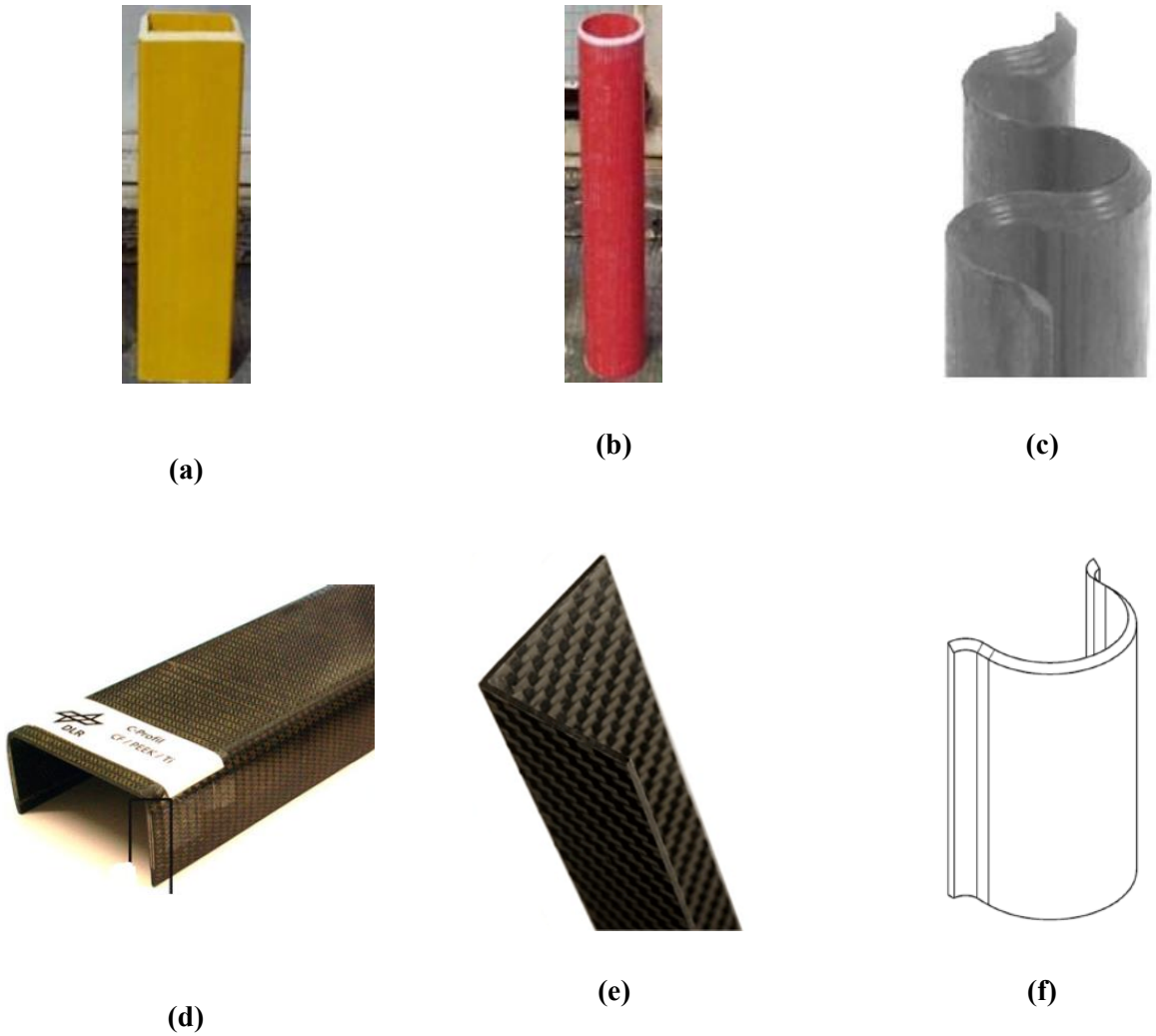

Figure 2.5: *Self-supporting composite geometries – a: square (38), b: circular (38), c: sinusoidal (24), d: c-shaped (39), e: angular (40), f: omega (27)*

However, to assess the influence of only the material or the manufacturing process on the crashworthiness of composite structures, crashworthiness tests on flat plate coupons need to be conducted. Without any lateral support or constrains, when impacted in the in-plane direction flat composites plates tend to slip laterally. Also, there exists a tendency for them to buckle and fail catastrophically if not supported laterally, ultimately defeating the purpose of testing them to understand the in-plane crashworthiness properties of the inherent material systems. Hence, to promote progressive failure under in-plane impact, flat composite plates need to be constrained using a fixture. Such a fixture was first developed at NASA in the early 1990s and is shown in Figure **2.6**. The fixture composed of an impactor plate that was guided by four vertical rods with linear roller bearings. Two versions of the fixture were developed that could tests plates with two different dimensions: 102 x 152 x 4 mm and 51 x 76 x 2 mm. The composite plates were supported by four knife-edge columns extending along the entire length of the plates.

Figure 2.6: *First ever anti-buckling fixture to test flat composite plates; Developed at NASA (41)*

The pioneering effort was able to generate force-displacement curves similar to those obtained from previous published studies on tubular specimen. However, in an investigation by Bolukbasi and Laananen it was discovered that the specimens tested using the NASA fixture resulted in higher SEA values, which they attributed to the over constraining of the specimen at the bottom (42).

A modification of the NASA fixture was developed at University of London in the late 1990s. The fixture, shown in Figure **2.7**, could test specimen with varied widths and thicknesses and the knife-edged supports could be adjusted to reduce friction between the specimen and the supports (43). Researchers observed local tearing at the knife edges in the composite specimens tested, which could result in higher SEA values being obtained as a secondary failure mode is artificially added to the primary failure mode, which was the objective of investigation. The secondary failure mode would not have occurred had the geometry been different (44). Additionally, as the specimen was constrained along the entire length, the crush front was probably not uniform along the entire width of the specimen due to tearing at the knife edges.

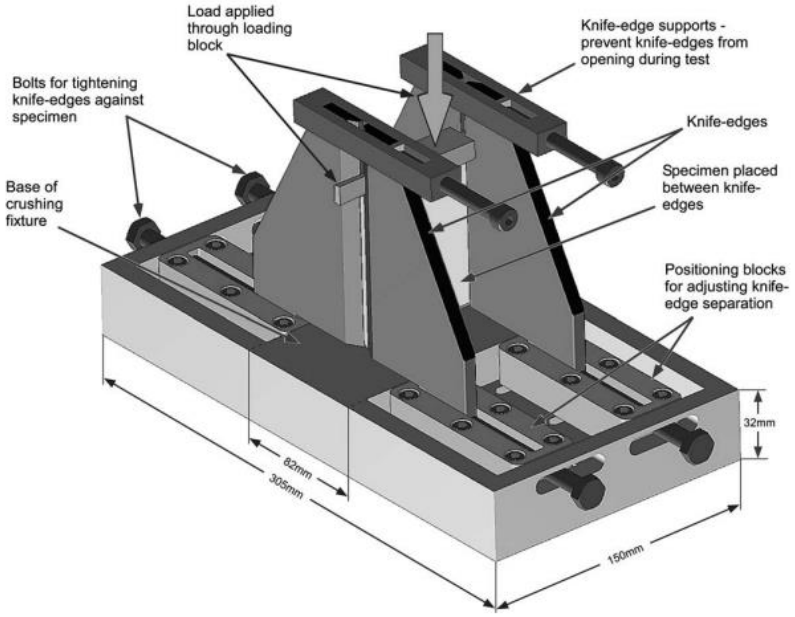

Figure 2.7: *Anti-buckling fixture developed at University of London (44)*

Around the same time, another fixture was developed at University of Tennessee as shown in Figure **2.8**a (45). The fixture could test plates with widths up to 50 mm and thicknesses up to 4.55 mm. The constrained profile permitted only one type of deformation upon impact, as can be seen from Figure **2.8**c. Results being forced towards a specific failure mode were not representative of what naturally occurs during a real crash scenario and in case the round constraint shown in Figure **2.8**b was not applied the results were not considered as reliable. However, the curved geometry of the constrained profile allowed the specimen to be tested without an inbuilt trigger, which was not the case for the fixtures described above.

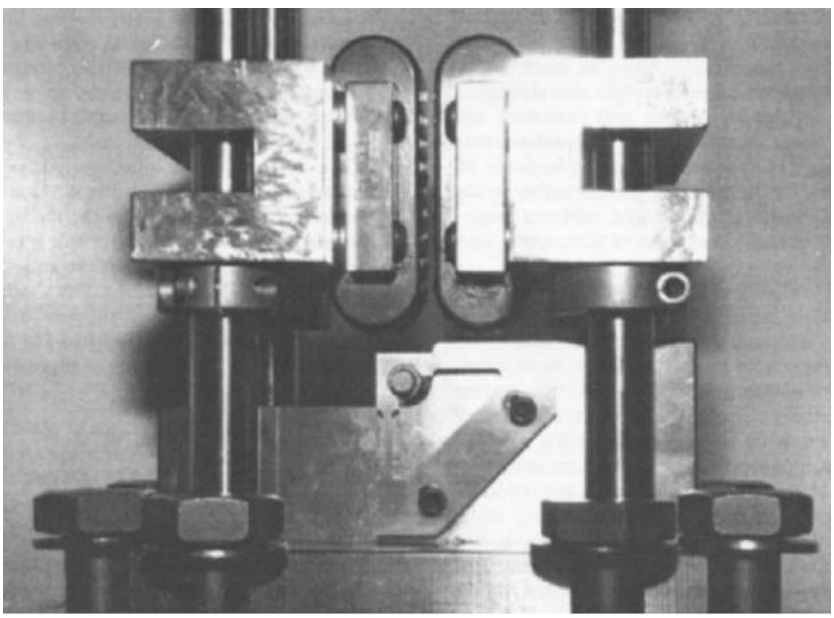

(a)

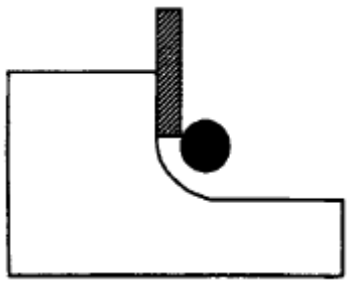

(b)

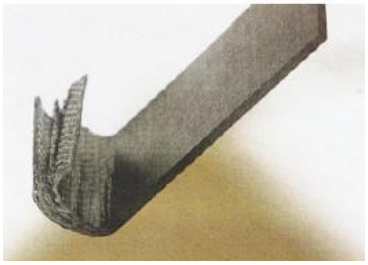

(c)

Figure 2.8: *Fixture developed at University of Tennessee (a); Constrain and failure propagation profile of the fixture (b); Specimen after impact (c) (45) (46)*

Another fixture developed by Engenuity in the early 2000s build up on predecessors and could constrain the lateral and out-of-plane deformation of flat plates, restricting the deformation only in the proximity of the crash front. The main advantage of the Engenuity fixture, shown in Figure **2.9**a, was that the deformation at the crash front was unrestricted, unlike that of the fixtures it succeeded, due to the absence of knife edged or any other columns near the unsupported height (47). Unsupported height is the length of the specimen that is not constrained in any direction, extending from the point on the base plate where the specimen touches to the point on the anti-buckling supports that is closest to the base plate and the specimen as illustrated in Figure **2.9**b. The complexity of the fixture required extensive calibration and post-crushing, the specimen would occasionally jam due to fronds and debris making egress difficult and damaging the specimen further, which would make post-failure analysis using NDT techniques difficult (48).

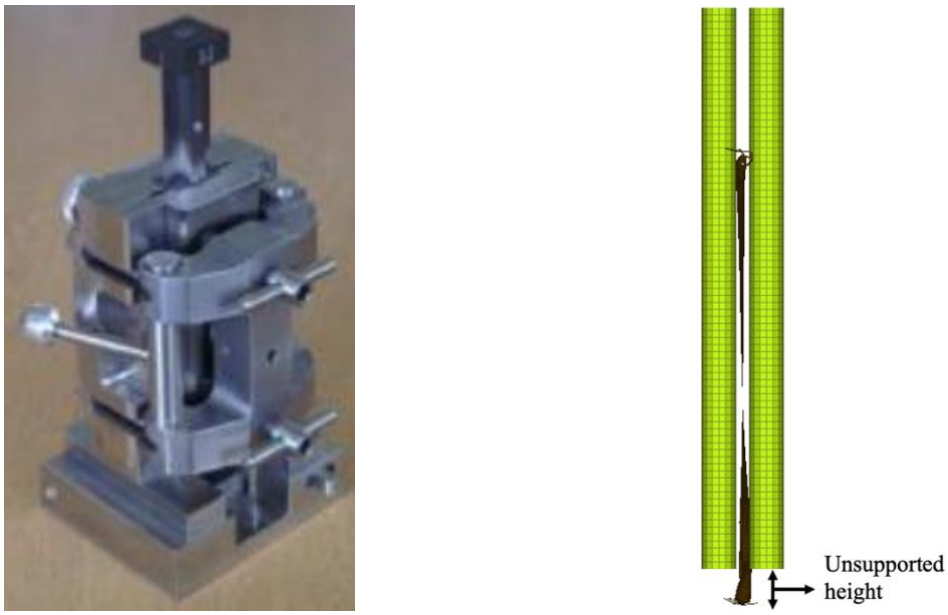

(a) **(b)**

Figure 2.9: *Fixture developed by Engenuity (21) (a); Illustration of unsupported height (b)*

Researchers at the University of Washington in the late 2000s developed the so-called Feraboli fixture (named after the researcher who led the fixture design and development), which built upon the NASA fixture by inculcating a screw mechanism to adjust the lateral supports, thereby allowing specimens with different thicknesses to be tested. In addition, a region of unsupported height was included to allow unrestricted crash front propagation leading to uniform frond formation and an assessment of the effect of different unsupported heights on the SEA capabilities of composite materials. The unsupported height also prevented the accumulation of a debris wedge between the knife-edges. The unsupported height could be increased up to 25.4 mm in increments of 3.2 mm. Apart from these changes, the fixture's functioning was similar to that of NASA's (41). The Feraboli fixture is shown in Figure **2.10**. As the fixture continued to use knife-edged anti-buckling supports, tearing was still observed at the edges. Also, the impactor was specifically designed to test a 2 mm thick CFRP composite, which limited its abilities in testing thicker plates or materials with higher SEA capabilities. Since the fixture was built along the lines of the smaller NASA fixture that could test specimen

with 51 x 76 mm dimensions, testing of bigger specimens, such as those mandated for use in compression after impact (CAI) tests, was not possible.

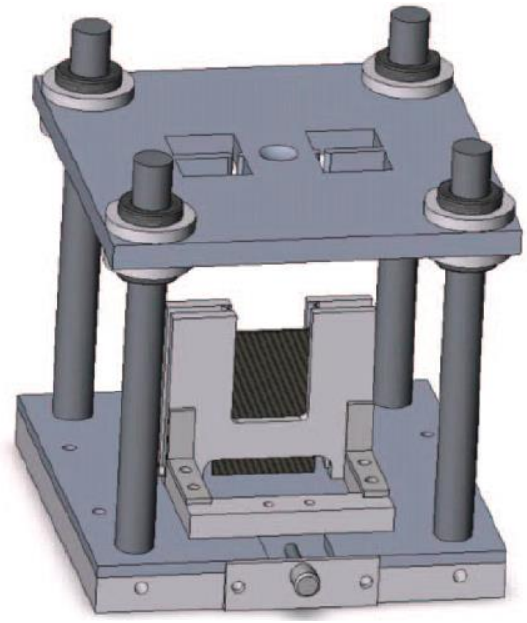

Figure 2.10: *Feraboli fixture (41)*

Due to the constant development of anti-buckling fixtures, an absence of standardized methodology for testing flat plates, and the costs involved with testing larger composite plates, some researchers began characterizing the crashworthiness behaviors of composite materials using much smaller specimens, to use the data for numerical studies. Researchers at Swerea SICOMP conducted tests with 10 x 22 x 1.9 mm specimen in a simple fixture as shown in Figure **2.11**. The size of the specimen resulted in only 3 mm of displacement over which the mean crush force could be obtained and only slight fronding to be observed (49).

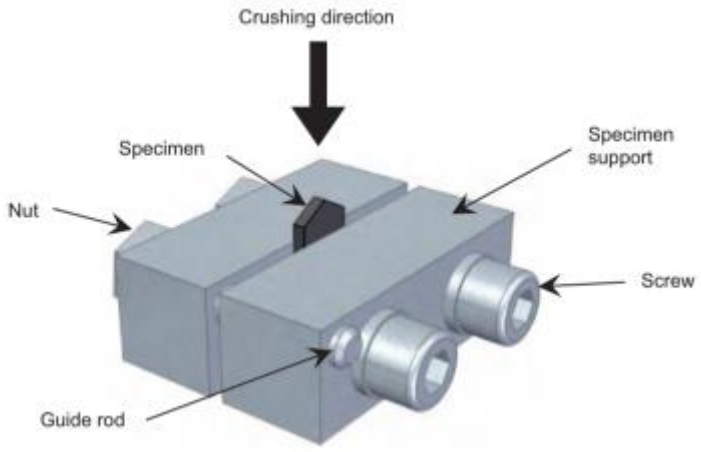

Figure 2.11: *Testing jig at Swerea SICOMP for small composite coupon crashworthiness testing (49)*

Similar tests were conducted at Queens University Belfast (QUB) on specimen measuring 30 x 79 (of which 15 mm was the length of the trigger region) mm. Like the previous case, only slight fronding was observed and the region of sustained crushing lasted only 7 mm (50).

Therefore, in order to be able to test flat composite plates that were large enough to obtain sustained progressive crushing over a longer displacement and time a new fixture was needed, one that was robust enough to test specimen with varied thicknesses and unsupported heights, permit both quasi-static and dynamic testing, permit uninterrupted crash front and frond propagation and allow for easy egress of the damage specimen for non-destructive test (NDT) inspection. Such a fixture would allow for standardization of composite flat plate testing.

2.3. Modelling of impact behavior

As seen from section 2.1, composite behavior under crushing is a complex phenomenon because of the interactions of different failure mechanisms that are a factor of various conditions such as manufacturing process, reinforcement and matrix constituents, loading conditions etc. In order to capture these behaviors four different approaches that depend on the level of detail required and the available data can be followed. These approaches are microscale, mesoscale, macroscale and multiscale.

Microscale approach entails modelling each fiber within the matrix in a representative volume element (RVE) as shown in Figure **2.12**. An RVE is an enclosed volume that represents the fiber volume fraction of the entire composite material by placing individual fibers within the matrix either randomly or by following a set algorithm, depending on the adopted manufacturing procedure (51). Occasionally, where resources permit, digital image analysis of a real composite cross-section is conducted to obtain the distribution of fibers within the matrix (52) (53). Due to the possibility of higher kinematic freedom microscale models are able to describe the behavior of the fiber, matrix, and interface under different loading conditions with high resolution (18). However, models require the desired information about constituents that require an extensive experimental campaign involving testing on the fibers, matrix and interface separately. A microscale analysis models behaviors such as matrix cracking, fiber debonding, fiber breakage, etc. that accrue towards meso- and macroscale damages such as those described in section 2.1 (54) (55). Additionally, it can predict the effect of micromechanical defects and spatial distribution of constituents on the composite behavior. Although, micromechanical studies have been conducted to show and predict these microscale damages under several loading conditions, none have been conducted for large-scale high energy dynamic crashworthiness tests due to the computational effort required (56) (57) (18).

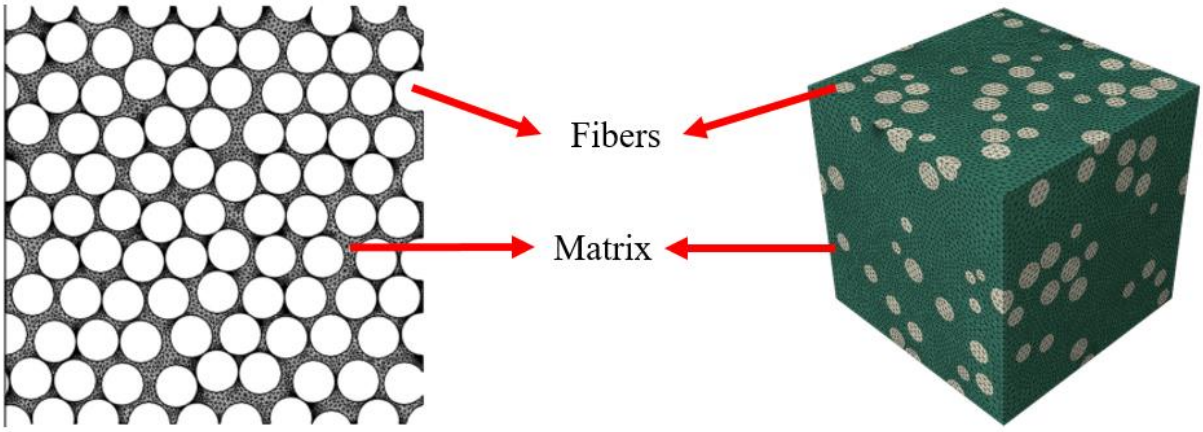

Figure 2.12: A 2D (a) and 3D (b) RVE (51)

Mesoscale approach, first introduced by Ladeveze et al. in the late 1980s, seeks to model the reinforcement and matrix that constitute a composite at "a structural analysis scale" by modelling each ply into "a homogeneous single layer in the thickness" connected by "an interface which is a two-dimensional medium connecting two adjacent layers" into a laminate (32). Including an interface allows for delamination failure mode to be modelled, as it is a crucial to for energy absorption during splaying. The behavior of the laminate and its individual plies is typically computed using the Classical Laminate Theory (CLA), although other theories such as Carrera Unified Formulation, Zigzag Theory etc. can also be used to model composite behavior (58) (59). However, CLA has typically used for crash applications. Ply-by-ply discretization is able to model laminate behavior, whilst microstructural damage such as matrix cracking, brittle failure of fibers and fiber-matrix debonding are included at the ply level using various damage variables, such as homogenized stress or strain, energy absorption etc., or models, such as CRASURV, Puck, Hashin, Ladaveze etc. (60) (61) (62). The mechanical properties of the plies and the interface can be obtained from experimental tests or from micromechanical models. Ply properties are derived using standardized ASTM tests for tension, compression, shear, flexure etc. and interface properties from DCB and ENF testing. Plies can be modelled using either 2D shell or 3D solid elements that represent a ply each. The interface is modelled using 1D spring or 3D solid elements as shown in Figure **2.13**a and Figure **2.13**b respectively. The figure represents four plies connected using three layers of elements. Initiation and growth of crack is obtained by the deletion of these elements that act as "zero-length" springs. Failure is evaluated based on limit values for strain, force, energy, or stress. Occasionally, a stacked shell approach, as shown in Figure **2.13**c, is used, wherein an element represents several plies under perfect bonding. This extended mesoscale model was proposed by Johnson et al. as a method to obtain numerical efficiency by increasing the time step as a result of larger elements, whilst ensuring that the delaminations were still modelled (63). It allows the flexibility to tailor the model according to the level of detail needed. The figure shows four UD plies in a laminate that are stacked into two layers of shell elements consisting of two plies each that are connected using spring elements.

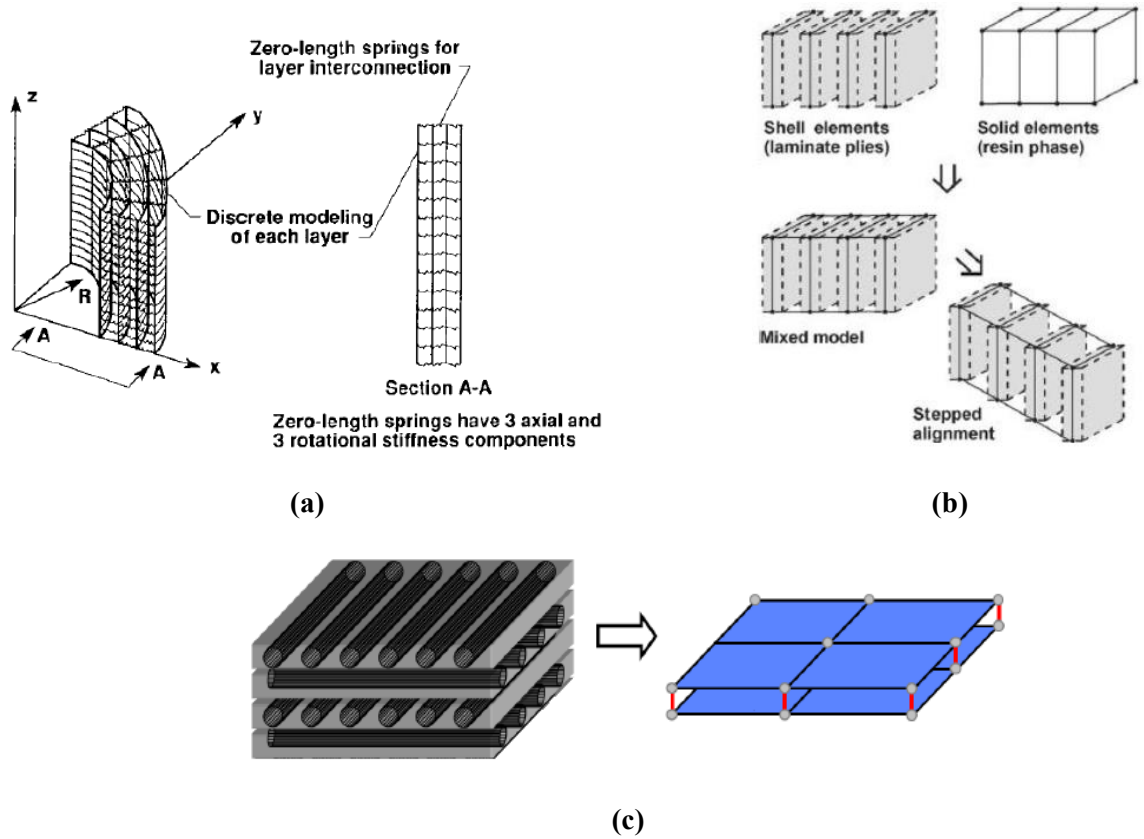

Figure 2.13: *Finite element model made of shell and spring (a) elements and shell and solid (b) elements; stacked shell approach (c) (64) (65) (27)*

Over the years, woven fabric (WF) reinforcements have found use in composite materials and have steadily replaced UD laminates due to their drapability that allows realization of complex geometries and increased resistance to delamination due to a significant reduction of transverse ply cracking (66). Pre-formed fibers are embedded into a matrix in different weave patterns such as plain (warp and weft yarns pass over alternately over and under each other), twill (warp and weft yarns pass over alternately over and under two or more yarns), satin (warp and weft yarns pass over alternately over and under a predetermined number of yarns) etc. depending on the number of yarns in the warp (0º) and weft (90º) directions. The mechanical interlocking of the yarns protects the integrity of the pre-form. The growing interest in WF composites has led to the development of non-homogenous mesoscale modes, such as that shown in Figure **2.14**, to understand and model the effects of interlocking and other factors on the crashworthiness of WF composites (67) (68).

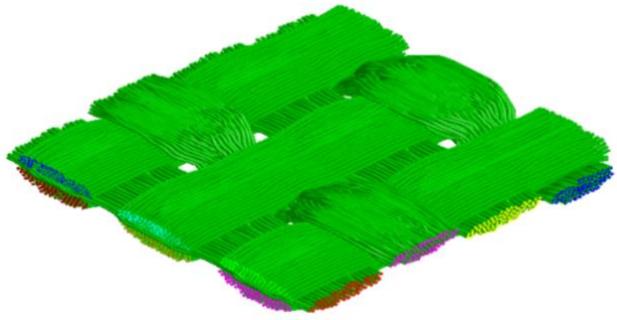

Figure 2.14: *Non-homogeneous mesoscale modelling of WF composites (69)*

Although mesoscale modelling provides computational efficiency as compared to microscale models, when a laminate is composed of several plies or the structure being simulated is large like a car chassis, mesoscale models still become computationally expensive. The minimum element size requirement in order to accurately represent the physical geometry and obtain numerical objectivity to model the damage mechanisms further contribute to the increase in computational effort. Therefore, full-scale or preliminary analysis and topology and layup optimizations require the use of a macroscale approach. In a macroscale model, the building block is the laminate that is assumed to have homogenous material properties that are representative of its constituents. Due to the level of simplification, material properties of the laminate need to be determined for each new material system or layup either through an experimental campaign or through a combination of virtual testing using mesoscale models and experimental results (18). However, as the laminate is considered as a homogenous structure, the number of material parameters required are significantly lower as compared to those required for the microscale and mesoscale approach, which in turn reduces the material characterization testing (70) (71). In order to further reduce experimentation, physically based modes are used as opposed to analytical models to measure and predict laminate strength and fracture toughness (18).

Macroscale models for crash simulations typically consist of an elastic model and one or more failure criterion and post-failure damage models that permit progressive failure, ultimate material failure and deletion of failed elements. Elastic models use stress-strain relations based on Hooke's Law, adapted for orthotropic materials, and properties derived from experiments. Maximum stress and strain are the simplest of failure criterion used. Others include Hashin, Chang and Chang and Puck failure criteria that were based on in-plane tension, compression and shear terms (61) (60) (72). Wolfe and Butalia in late 1990s introduced an energy-based criterion that could be used to model composite failure (73). Their criterion is based on the strain energy obtained from the axial tension and compression, transverse tension and compression and shear stress-strain experimental graphs, wherein axial refers to along the fiber direction and transverse refers to perpendicular to the fiber direction. The criterion is the area under the stress-strain curves under tension, compression and shear loading divided by the ultimate strain-energy value and raised by a power of the shape function. The shape function value determines the shape of the failure surface and depends on the material used. Shape functions are determined by biaxial tests and curve-fitting and remain same regardless of the laminate configuration, but within an upper bound of 2. The sum of the three components, axial, transverse and shear loadings, becomes the Wolfe and Butalia's strain-energy failure criterion as shown in Equation 2.3.

$$\left(\frac{\int_{\varepsilon_1} \sigma_1 \, d\varepsilon_1}{\int_{\varepsilon_1^u} \sigma_1 \, d\varepsilon_1}\right)^{m_1} + \left(\frac{\int_{\varepsilon_2} \sigma_2 \, d\varepsilon_2}{\int_{\varepsilon_2^u} \sigma_2 \, d\varepsilon_2}\right)^{m_2} + \left(\frac{\int_{\varepsilon_6} \sigma_6 \, d\varepsilon_6}{\int_{\varepsilon_6^u} \sigma_6 \, d\varepsilon_6}\right)^{m_6} = 1 \qquad 2.3$$

Around the same time, as a part of European research project funded within the framework of the EU's Brite Euram program, CRASURV failure criterion was developed as a modified form of the one developed by Tsai-Wu. In addition to strain-based failure CRASURV formulation also included an energy-based criterion, which was one of the main differences as compared to the Tsai-Wu formulation. This criterion was validated on

various composite materials and the underbelly and airframe of the A320 family of aircrafts (74) (75). It was used extensively in this study and is further explained in section 3.3.3.

To model the post-failure behavior of the elements, a damage model should be specified, which reduces the material performance in a process called softening. Damage models follow either the continuum or progressive damage approach (76). Continuum damage mechanics (CDM) approach, first introduced by Talreja in mid 1980s, models material damage using internal state variables, that degrade the material performance as the damage progresses, contained in continuous field equations that allow the material to remain in continuum (77) (78). CDM models degrades the material structural properties until the residual stress bearing capacity is zero or another condition is specified (21). Progressive damage models, on the other hand, degrades a material property or property set upon failure at the ply level until the degradation of all plies in the laminate. This results in a non-continuous damage, albeit a more computationally efficient one that is able to model the quasi-brittle nature of FRP composites accurately (76). A progressive damage model was used in this study, which is further explained in sections 3.3.3 and 5.

As can be seen, each of the three approaches, microscale, mesoscale and macroscale, have their advantages and disadvantages. Hence, **multiscale** approaches in the space domain were proposed that could communicate between the scales and overcome their shortcomings. Use of multiscale approaches became increasingly common as computational power increased (79). Multiscale approaches typically model micromechanical failures such as matrix cracking etc. and their respective damage and failure theories within mesoscale or macroscale models to either gauge the effect of these microscopic behaviors on properties such as strength and strain or to conduct in-depth structural scale analysis (80) (81).

Due to the computational efficiency and ability to represent most major failure modes, mesoscale modelling has been used extensively to model failure of composite materials under impact loading (27) (23) (82) (83) (50). Typically, two types of impact tests have been modelled in published studies: in-plane (axial) and out-of-plane (transverse), both of which are schematically shown in Figure **2.15**. Transverse tests are used to simulate bird, tool-drop, or runway debris impact on airplane underbelly or car bonnet, whilst axial impact simulations are conduced to model car crashes such as the ones shown in Figure **2.2**, which is the focus of this work. Such an impact is representative of a car crash, although there have been incidents that have resulted in oblique loading during car crashes. F1 certification for side impact structures is also performed at oblique loading angles, but few published studies exist on oblique loading of composite structures, one of which was conducted in 2019 by a group of researchers in India and Portugal, who conducted numerical and experimental tests on circular CFRP tubes at 10°, 20°, 30° and 40° impact angles (84) (50).

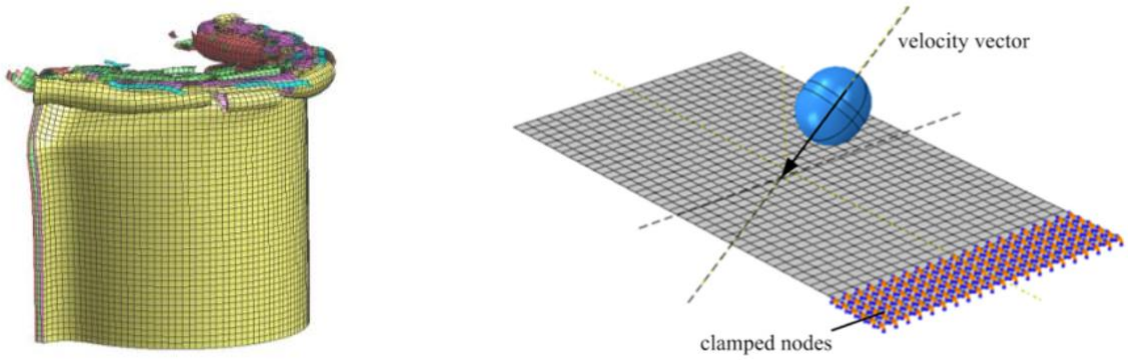

(a) **(b)**

Figure 2.15: *In- (a) and out-of-plane (b) impact tests (27) (81)*

Several studies have been conducted that model composite crushing behavior, first of which was done using the Engineering Analysis Language (EAL) finite element program by Farley and Jones in 1989 subsequent to the experiments they conducted on circular composite tubes. They modelled the tube as a quarter symmetric section of four layers modelled using 2D elements connected using "zero-length" springs (tie-break contacts) with axial and rotational stiffness to model interlaminar behavior in a manner similar to that shown in Figure **2.13**a (30). They were able to capture lamina bending, brittle fracture and interlaminar cracks also observed in experiments, but recorded significant deviations from experimental SEA values. They attributed the deviations to a lack of reliable compression testing methodology that can be used to calibrate the numerical model and a mismatch between the batch of material used to produce the tubes and the specimens used to characterize the material properties. However, their simulations showed that composite crash behavior could be reasonably modelled, the effect of different ply orientations on the SEA captured and better correlations with experimental data obtained by a refinement of the models. Since then, a standardized experimental test method was published by ASTM that has been modified several times to D6641/D6641M, which is presently used to characterize compressive properties of polymeric composite laminates (85). Additionally, various numerical models, failure models and criterions were also developed to more accurately capture the crushing behavior of composite materials as a part of multiple worldwide failure exercises, some of which were implemented in commercial software such as Abaqus, LS-Dyna, Radioss, Pam-Crash (86).

Researchers at DLR introduced the concept of adding a numerical trigger to simulation models to initiate fronding and progressive failure. The trigger was made by adding a rigid body known as a "separation wedge" that mimicked debris formed in between the plies during crushing and offsetting two row of elements in the impact area, which upon impact would separate the middle two shell layers into fronds, as shown in Figure **2.16**a (87). They used a stacked-shell approach with shell elements measuring 1 x 1 mm connected using spring elements to model a self-supporting semi-circular CFRP tube using Pam-Crash. They calibrated the delamination model by curve fitting the force-displacement results from the DCB and ENF models with the results obtained from experiments in order to determine the G_{IC} and G_{IIC} values, which were used as failure thresholds for damage modelling of the cohesive springs. They set the damage parameters for shell elements as 0.90, 0.50 and 0.65 for tension, compression and shear loadings respectively that ensured that stress carrying

capacity of the material post failure was reduced by 90%, 50% and 65% respectively. The numerical trigger resulted in "a central delamination interface, which then caused frond formation and petalling" similar to that observed in experimental tests. However, they discovered that extending the methodology to beams with different cross-sections required modifications to be made to the trigger (27). Additionally, they obtained crush forces and SEA within 10% of the experimental results, albeit by using an SAE 1000 filter to flatten out the peaks and troughs caused due to each row of elements absorbing energy until the peak and damaging until the trough that bottom out at zero force after which the subsequent row of elements would begin absorbing the energy, hence the wavelength of the wave was equal to the element size. The SAE filter was also used by researchers at the University of Washington and other due to a similar behavior as shown in Figure **2.16**b. They modelled a composite beam with a sinusoidal cross-section using a macroscale approach (only shell elements measuring 2.54 x 2.54 mm) but modified the chamfer trigger by modelling it using a stepwise approach in numbering the plies (2, 6, and 10 plies) that increased gradually as the elements approached the main part of the sinusoidal component composed of 12 plies. Their simulation model using LS-Dyna was able to model the experimental force and SEA as the damage parameters used were first calibrated using the experimental SEA before being inputted into the final model. Due to the use of shell elements only they could not capture the fronding behavior (24) (21) (88). They also conducted a sensitivity study that concluded that the crushing behavior mostly depends on the compression strength, compression strain-to-failure and the softening post-failure, all of which need extensive calibration, an observation echoed in sensitivity studies conducted by Boria et al. on composite tubes with circular and square cross-sections using the same material model in LS-Dyna (89) (23) (21). Boria et al. were then able to model the crushing behavior of a Formula SAE crash box, similar to the one used for the validation of this study, using the same methodology and obtain SEA and crushing force values within 10% of the experimental results (82).

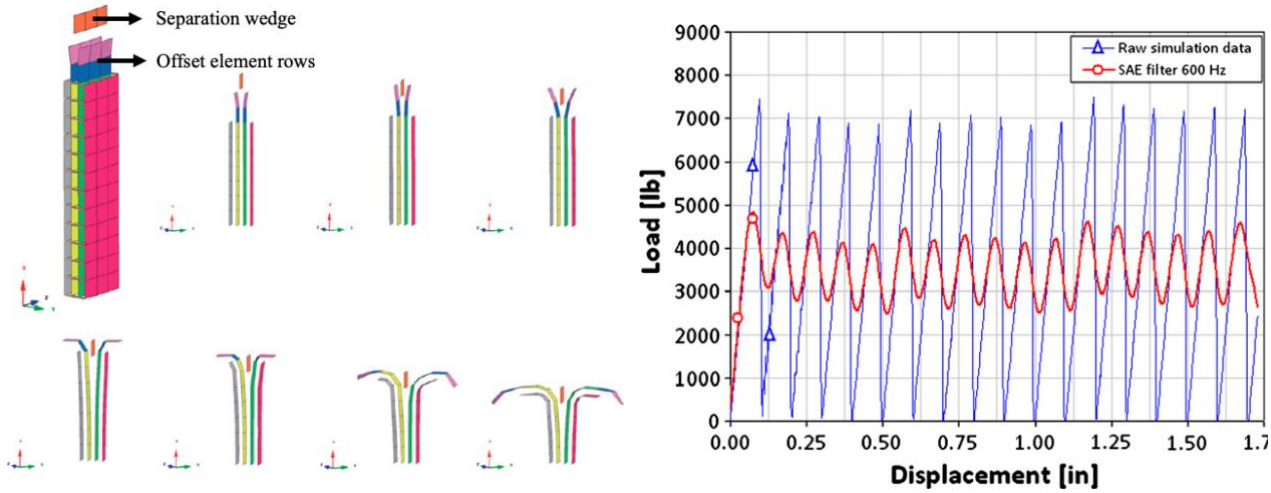

Figure 2.16: *Numerical trigger introduced by DLR (a) (87), SAE filter applied to raw simulation data by Feraboli et al. (b) (21) (24)*

Ren et al. further experimented with different numerical triggers by testing five double coupled triggers (DCT) (chamfer/hole, chamfer/slit, chamfer/sawtooth, chamfer/plug and chamfer/slit) and four triple coupled triggers (TCT) (chamfer/hole/plug, chamfer/slit/plug, chamfer/saw tooth/plug, and chamfer/gradient material

degradation/plug) to arrive at a trigger mechanism that could better predict crush properties and understand their effects on the peak load and SEA. They concluded that using a DCT reduces the peak load, whilst a TCT increases the SEA, and a chamfer/gradient material degradation/plug trigger offers the best compromise between the two (35).

In a modification of the above-mentioned methodologies, Joosten et al. and Fleming replaced spring elements between plies with 3D 8-noded solid elements to model the cohesive layer on complex structures such as a cruciform specimen and a composite beam with a hat-shaped cross-section. They used data obtained from DCB and ENF testing to model the damage and were able to obtain a similar degree of correlation with experimental results as obtained using tie-break contacts (90) (91). Andersson and Liedberg compared the ability of the tools available in LS-Dyna and Radioss to accurately model crushing behavior of a corrugated specimen. They concluded that both software were able to model the behavior accurately, but the methodology involving LS-Dyna is much simpler as fewer physical parameters are needed which reduces the amount of physical testing that needs to be conducted. However, this results in many non-physical parameters that are should be tuned in order to stabilize the model and obtain convergence. On the other hand, Radioss allows for several physical parameters to be inputted requiring an extensive material characterization campaign. However, it is more robust as it allows greater control over the deletion of elements and flexibility to specify stress-strain behavior in different directions and loading scenarios (19).

The methodology developed at DLR was later improved to include state-of-the-art damage criteria, 3D solid elements for cohesive zone modelling and a mesh inclined at 15°. The model was calibrated using the omega shaped beam and the calibrated model was then used to predict the crushing behavior of an aircraft cargo area component. Using the exact same numerical model, instabilities were observed in the component level model because of which some cohesive input parameters had to be modified, after which the model was able to predict component damage (26). Since the modelling methodology was not similar for the specimen and the component, the predictive ability of the methodology was below par. Additionally, the model was calibrated using a trial-and-error approach, which had also been used in the studies mentioned thus far. A trial-and-error approach for calibration is known to be cumbersome, expensive (time and resources) and relatively subjective. Hence, once it was established that the crushing behavior of specimens or components made of composite materials could be accurately modelled numerically, methodologies that either involved automatic calibration using optimization and identification algorithms or numerical methods that completely eliminated the need of calibration were developed.

Researchers at QUB developed a multiscale 3D composite damage model integrated with Abaqus that included damage characterization for intralaminar, matrix and interlaminar damage that could model the primary failure mechanism during crush. They validated the model only on small CFRP specimens with the following maximum dimensions: 10 x 60 x 4 mm with the unclamped length extending up to approximately 50% of the length and were able to predict both qualitatively and quantitatively the damage response of the specimens to a reasonable degree of accuracy under quasi-static loading conditions (92). The methodology was later

validated on 76 x 50 mm corrugated CFRP specimens and tulip triggered cylinders under quasi-static conditions and the response was predicted accurately (93). It was then used to predict the damage in a side impact structure placed on the McLaren F1 car under dynamic loading conditions (10 m/s) and the accuracy of the prediction was not as high as was observed under quasi-static loading conditions and additional inputs and calibrations were required to achieve a reasonable level of correlation (50). In a juxtaposition of the QUB approach that eliminates the need of any calibration, Reuter et al. calibrated their models until the difference in the experimental and numerical mean force level was less than 5% for flat CFRP plates with unclamped dimensions of 60 x 90 mm impacted at 3 m/s using a 60kg mass. They then used the calibrated parameters to predict the damage in a CFRP cylindrical tube and observed large deviations from the experimental results, which they attributed to the different mesh sizes used for the flat plate and cylinder model. After remeshing, they were able to obtain a good correlation between the experimental and numerical results. Although they did not consider the entire force-displacement curve for the calibration, instead concentrating on only one aspect of it, their methodology clearly showcased its predictive capability for small and less complex composite structures (94). Cherniaev et al. used a quadratic lagrangian gradient-based optimization technique instead of a trail-and-error approach to calibrate two non-physical parameters in their LS-Dyna material model to calibrate it using composite tubes with square cross-sections, but the predictive ability of their methodology was limited to tubes with similar geometry, albeit with a different layup (22).

As it is clear from the aforementioned overview of published literature relating to modelling of impact behavior, there does not exist a methodology that can accurately and automatically calibrate the material card, which can then be used to predict the crash behavior of large components. Only parts of this have thus far been modelled, tested and validated. The methodology presented henceforth aims to plug these gaps to enable quicker implementation of composite materials for use as primary crash structures in automobiles.

3. Numerical Modelling

This chapter presents part of the numerical methodology related to setting up the simulation model that was used for the purposes of this work. Although, Altair's HyperWorks suite was used due to the ease of its integration with the design and development tools available at Centro Ricerche Fiat, the general framework of the methodology could possibly be used with other numerical commercial software. Within the HyperWorks suite, HyperMesh was used for pre-processing, HyperView and HyperGraph for post-processing and Radioss was used as a solver. All simulations were conducted using six cores of Intel i7 CPU @ 2.70 Hz unless otherwise stated.

Within the chapter the flat-plate model refers to the model developed to identify certain design parameters for the fixture developed and then to test flat composite plates. This model was used to calibrate the material card by comparing the force-displacement data with that obtained from experiments (95). It was also used to identify other numerical parameters that enabled progressive crush and accurate representation of the contacts between the various components. The impact attenuator model refers to the model developed to validate the methodology by testing a Formula SAE crash box under impact loading and comparing the results with those obtained from experiments (95). Each of the models was developed at a macroscale and mesoscale to compare the ability of the two approaches to accurately capture the crushing behavior and possibly obtain approaches that are efficient and sufficiently detailed to capture the major failure modes respectively. The following sections present an overview of the fixture design, followed by an overview of the models before detailing the material and property cards and models used. They also discuss the contact formulations used for both the models.

3.1. Overview of the fixture design

The final design iteration of the anti-buckling fixture was composed of a base plate onto which the specimen would crush and a top plate which would exert force on the specimen and crush it. The top plate would be impacted in the top center by a falling mass inside the Instron drop tower machine. Passing through the top plate and fixed onto the bottom plate were four guide columns that were fitted with bearings to ensure perfect alignment and stability of the top plate throughout duration of the impact. Underneath the bottom plate passed a screw mechanism assembly on top of which four triangular lateral supports were bolted to avoid deformation or opening up of the anti-buckling columns due to out-of-plane forces that occurred as a result of vibrations caused during impact and any lateral instability of the composite plate caused due to manufacturing or machining defects or those inherently present in the material or caused due to the chosen layup configuration. Two lateral support plates, one on each side, were bolted onto two triangular supports each to ensure alignment between the triangular supports when the screw mechanism was used to translate the anti-buckling columns. Two anti-buckling columns were screwed onto each of the lateral support plates, each of which had a provision for a third anti-buckling column to be placed in case the material tested was wider than 100 mm or of lower bending stiffness causing it to buckle under impact. Four rubber inserts were screwed on top of the lateral plate

edges, two on each plate, to absorb any unabsorbed energy from the impact and prevent any damage to the fixture. Inclusion of these inserts ensured a maximum stroke displacement of 47 mm, sufficient to sustain the mean crush force over a large displacement. Additionally, the plates also had a provision to change the unsupported height of the anti-buckling column by altering the height at which the anti-buckling columns were screwed at to test its effect on the crashworthiness of the specimen material. Unsupported height is the distance between the bottom plate and the lowermost point of the anti-buckling columns that allows for the fronds to propagate outwards and is known to have an effect on the crashworthiness results (21) (41) (96). A cavity was inserted in the top plate to allow the anti-buckling columns to pass through without any contact with the plate upon impact. The screw mechanism was used to translate the anti-buckling columns transverse to the composite specimen to adjust the distance between the two sets of columns and ensure that the columns merely "kissed" the composite specimen and do not excessively constrain it, causing it to tear during the impact. As the name suggests, the anti-buckling columns were placed to avoid buckling along the entire width of the specimen. The entire fixture sat on a platform that was developed to be integrable with Instron CEAST 9400 Series Droptower Impact Systems. Figure **3.1** shows the final design of the fixture as described above. The fixture was designed in close collaboration with Instron CEAST in Pianezza, Turin, Italy.

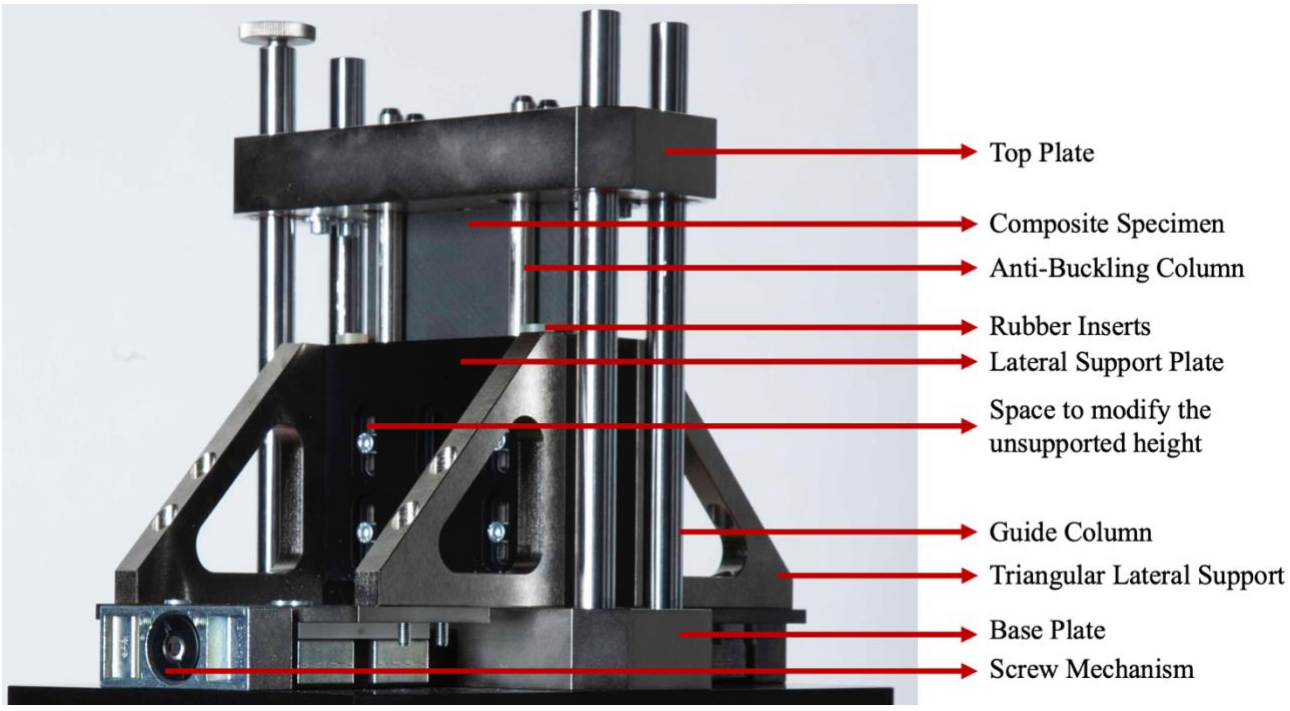

Figure 3.1: *Final design iteration of the anti-buckling fixture*

3.2. Numerical models

3.2.1. Flat-plate model

For both the numerical models (macroscale and mesoscale), the guide columns were replaced with boundary conditions on the rigid body element applied to the top plate that permitted only translation in the impact direction. The triangular supports and support plate were replaced with boundary conditions on the rigid body element applied to the anti-buckling columns that prevented any translation or rotational DoFs for the same.

The screw mechanism was not modelled as the anti-buckling columns could be translated using tools within HyperMesh. In keeping with the experimental setup, no DoFs were constrained numerically for the composite specimen.

The first iteration of the model was used to optimize the top plate thickness to ensure it exhibited only elastic deformations upon impact. The model was composed of a composite plate sandwiched between a top and bottom plate and supported by lateral anti-buckling columns. A cavity, similar to the one in the physical fixture, was modelled into the top plate to allow the anti-buckling columns to pass through and a type 7 contact was used to describe the interaction, if any, between the two components. An impactor was modelled, which would impact the top plate in a manner similar to the experimental campaign. Two types of impactors were modelled: a 15 x 20 mm cuboid with its edges (6 mm radius) rounded-off and a 17 x 50 mm rectangular plate, both of which are standard equipment for the Instron drop towers. The cuboid was modelled with a 1 mm mesh to capture its curvature, whilst the composite flat plate was modelled with a 4 mm mesh. Rigid body elements were applied to both the impactors to ensure that the elements moved synchronously. Only translational DoF was permitted for the impactor rigid bodies, similar to that in the physical drop tower. Rigid bodies were used to ensure that all the elements in the component move synchronously. The impactors are shown in Figure **3.2**.

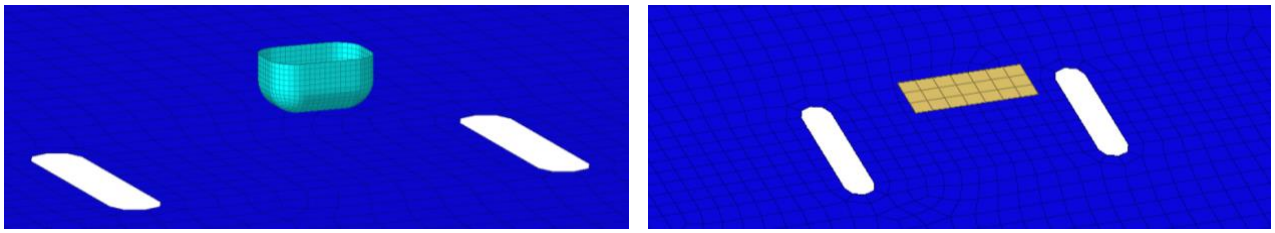

(a) **(b)**

Figure 3.2: *Cuboidal (a) and rectangular (b) impactors*

Element size for the bottom plate was 20 mm, whilst that for the top plate was 5 mm. A finer mesh was used for the top plate to better assess the boundaries of the region that undergoes plastic deformation upon impact at the highest energy level of 1850 J. To aid this assessment, mesh refinement was carried out on the top plate around the cavities and by splitting it along the red lines as shown in Figure **3.3** and ensuring a structured mesh with an element size of 4 mm in the center region, which was expected to undergo the highest deformation due to the concentration of the impact region, cavities and reaction forces from the impact on the composite specimen.

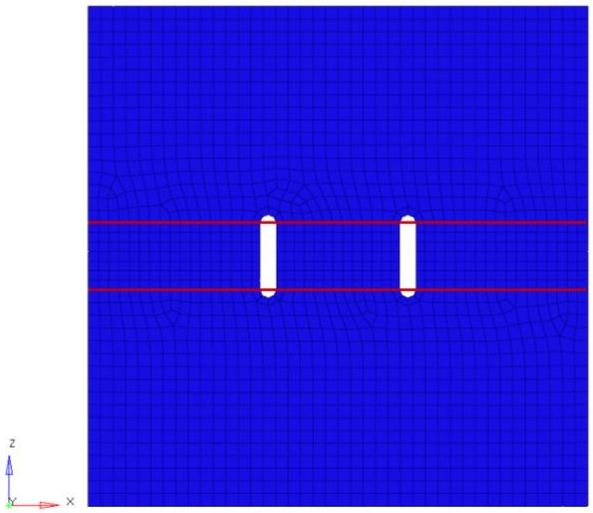

Figure 3.3: *Mesh refinement for the top plate*

The model, as shown in Figure **3.4**, was made of 3800 elements and 18,000 DoFs, of which the top plate was made of 1700 elements and 11,000 DoFs.

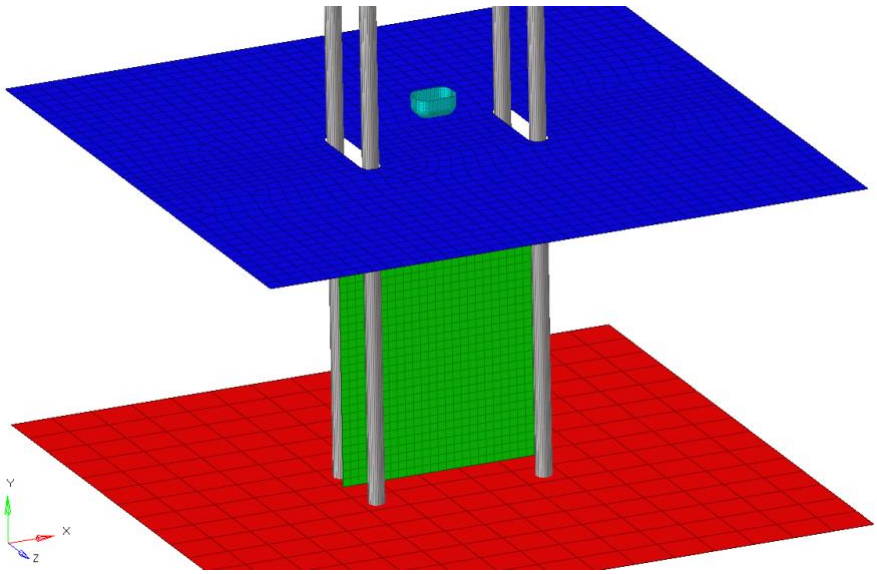

Figure 3.4: *First iteration of numerical flat-plate model (used to optimize the top plate thickness)*

After undergoing the process to determine the top plate thickness (see section 4.1) the fixture was optimized for weight to aid ingress and egress from the Instron drop towers. In doing so, the dimensions of the top and bottom plates were reduced from 300 x 300 mm to 200 x 78 mm. The model was redone accordingly. Since it was established that an impact of 1850 J led to only elastic deformations, the impactor was not modelled and the impact velocity, depending on the loading case, was applied, directly, to the top plate rigid body element to save computational resources. Additionally, the cavity in the top plates was omitted to obtain a structural mesh. Exclusion of the cavity did not affect the results as no contact model was defined between the columns and the plate, ensuring that their respective elements could pass through each other without any distortion or disturbance, a behavior similar to that obtained experimentally. Hence, the numerical model was made up of

the composite specimen sandwiched between four anti-buckling columns, all of which sat on the base plate and were impacted using the top plate as shown in Figure **3.5**.

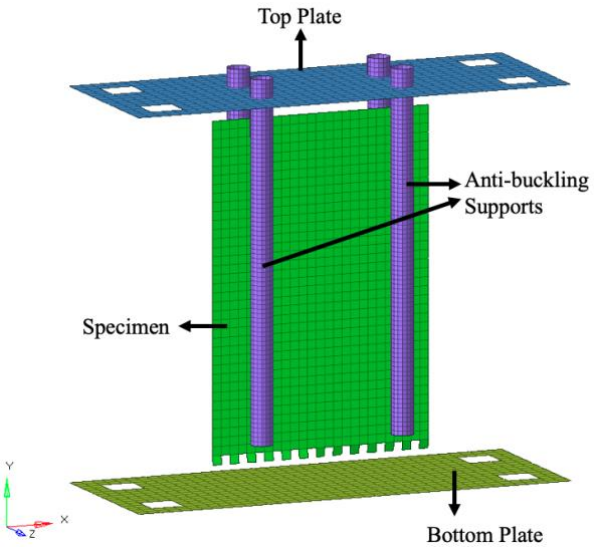

Figure 3.5: *Top plate numerical model*

An element size of 1 mm was used to mesh the anti-buckling columns in order to capture their curvature accurately, whilst a 5 mm mesh size was used for the top and bottom plates. A 4 mm mesh size was used to model the 150 x 100 mm composite specimen after conducting mesh dependency studies as explained, later, in section 3.2.1.3 Additionally, an element size of 4 mm was considered optimal considering the trade-off between accuracy and efficiency based on previous published studies on the crashworthiness of composite structures that have used a mesh size between 3 – 5 mm and obtained accurate results (82) (94) (22) (97). Moreover, a 4 mm mesh allows for scaling up of the methodology to component and full-scale testing without a significant increase in computation time or power when compared to finer meshes that have been used in literature studies involving tests on small specimens as computational time is dependent on the time step, which in turn is dependent on the mesh size for explicit analysis (92). The final macroscale model was made of approximately 12,500 elements and 6800 DoFs, of which the composite specimen was made of 940 elements and 6100 DoFs.

The anti-buckling supports and the base plate were both modelled using material law 1 (Elastic Material) and property type 1 (Shell), which are explained in sections 3.3.2 and 3.4.1 respectively. They were both made from C40 Steel, properties of which were obtained from the Total Materia database, all of which are mentioned in section 3.4.1. Total Materia database is an online repository that contains mechanical, thermal etc. properties of materials and their sub-architectures depending on international standards. The top plate, also made of C40 Steel, was modelled with the same property type as the other two metallic components, but was modelled using material law 2 (Johnson-Cook Elastoplastic), explained in section 3.3.1, for the case where its thickness was to be determined (section 4.1), after which it was modelled with law 1 as no plasticity was recorded at the highest energy level of 1800 J when the thickness was increased to 30 mm. The composite specimen was modelled with material law 25 (Composite Shell – CRASURV formulation) and property type 11 (Shell

Sandwich), which are explained in sections 3.3.3 and 3.4.2 respectively. A single shell layer of shell elements represented all four plies in perfect bonding. Contact type 7 (node-to-element) were used between the top and bottom plates and the specimen and amongst the elements of the specimen, whilst contact type 24 (surface-to-surface) were used between the anti-buckling columns and the specimen in order to accurately capture the crushing and sliding behaviors respectively. Both contact types are further explained in section 3.5. Since there was no interaction between the anti-buckling columns and the top plate, no contact was defined between the two.

3.2.1.1. Mesoscale model

In addition to the macroscale model described above, a mesoscale model was also created in order to capture delamination failure. There was no change in the metallic components. As the composite material used was composed of four plies, each 0.64 mm thick, four different layers of 4 mm shell elements were modelled 0.64 mm apart. Three layers of 3D solid elements 0.64 mm thick were modelled between them to form the cohesive layers, one each between two adjacent plies. All cohesive 3D elements were hexahedron in shape. The nodes between the solid and shell elements were merged, hence no contact modelling was required for cohesive elements as their deformation was dependent on the composite shell layers. Type 19 contacts (node-to-element and edge-to-edge) were used to model the interface between the four plied and between the plies and the anti-buckling columns. Type 19 contact is a combination of type 7 and type 11 (edge-to-edge) contacts and were preferred as numerical penetrations were observed when type 7 and type 24 contacts were used like in the case of the macroscale model. Type 19 contacts are further explained in section 3.5.3. Material laws 59 (Connect) and Fail_Connect and property type 43 (Connect) were used to model the cohesive behavior, which is explained in section 3.3.4. The model was made of 18,100 elements and 25,000 DoFs, of which the composite specimen was made of 6500 elements (3750 quadrilateral shells and 2750 hexahedron solids) and 24,300 DoFs. Figure **3.6** shows the cross section of the composite flat plate.

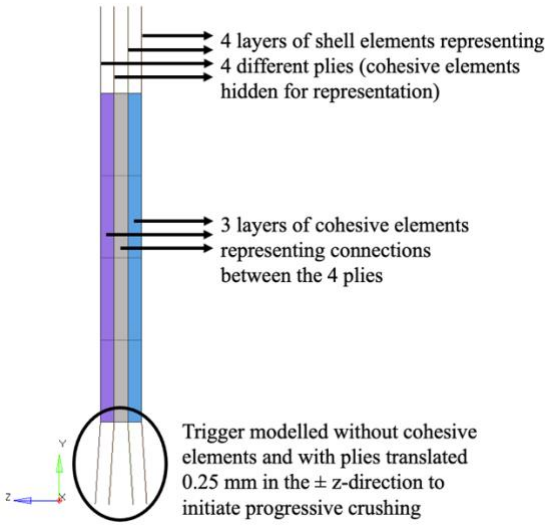

Figure 3.6: *Cross-section of the composite flat plate (98)*

3.2.1.2. Trigger design

As has been mentioned in section 2.3, trigger plays a crucial role in initiating crush behavior. A sawtooth trigger was machined into the physical composite plates as shown in Figure **3.7**a (48). Modelling such a trigger would require triangular elements, whilst a structured mesh, wholly made of the same type of element (quadrilateral, triangular, etc.) was desired for efficiency and stability of the numerical analysis, hence the sawtooth trigger was replaced with a boxed trigger for the numerical model as shown in Figure **3.7**b. Furthermore, in order to avoid deletion of subsequent row of elements one after another, which leads to force dropping to zero before increasing back again and to obtain progressive initiation of the crushing behavior, the bottommost nodes were translated 0.25 mm in the z-direction. For the macroscale model, half of the nodes were translated in the positive z-direction, whilst the other half were translated in the negative z-direction as shown in Figure **3.7**c and Figure **3.7**e. For the mesoscale model, the bottommost nodes of two of the plies were translated in the positive z-direction and those of the other two plies were translated in the negative z-direction as shown in Figure **3.7**d. In addition to this, the bottommost layer of cohesive elements was deleted in the mesoscale model to further aid progressive crush behavior. Modelling the trigger in the manner described above allowed for accurate representation of the physical failure modes and improved correlation with the experimental force-displacement data.

(a)

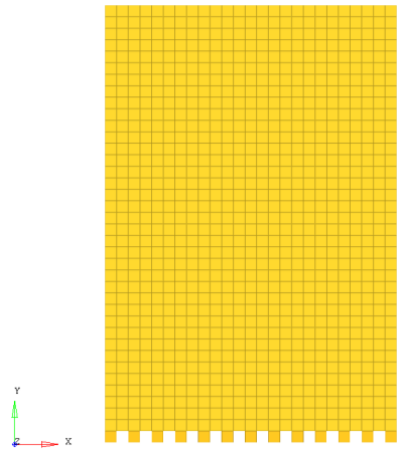

(b)

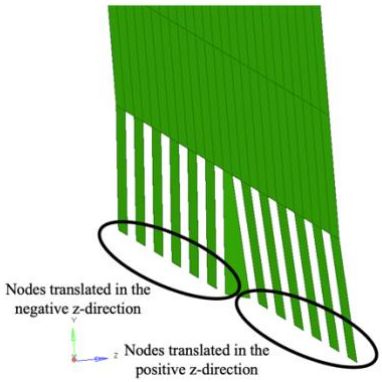

(c)

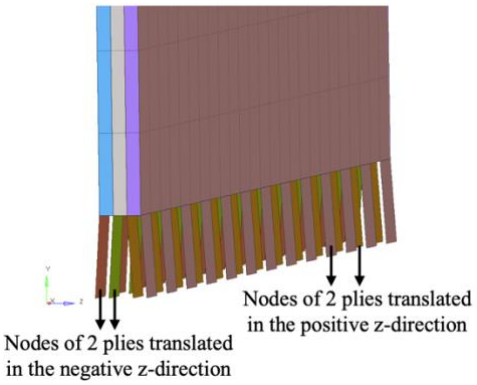

(d)

(e)

Figure 3.7: *Sawtooth trigger (a) (48); numerical boxed trigger (b); isometric view of the trigger in the macroscale model (c); isometric view of the trigger in the mesoscale model (d); bottom view of the trigger in the macroscale model*

3.2.1.3. Mesh dependency

An investigation was conducted to ascertain an optimum mesh size that was both accurate and efficient. Two different element sizes were considered: 2 mm and 4 mm. The model with a 2 mm mesh size was run with a boxed trigger and node offset into the plane similar to Figure **3.7**c and Figure **3.7**e (Figure **3.8**a) and with a boxed trigger with node offset in the y-direction wherein two columns of nodes were translated downwards by 2 mm (Figure **3.8**b). The mesh with node offset in the y-direction was created to investigate if such a "wavy" mesh could reduce the deletion of subsequent rows of elements thereby reducing the force oscillations in the results. Additionally, such an offset resulted in the boxed trigger being transformed into looking somewhat like the sawtooth trigger in the physical composite plate albeit with triangular elements needed to be modelled at the top of the plate. The 4 mm mesh is shown in Figure **3.7**b.

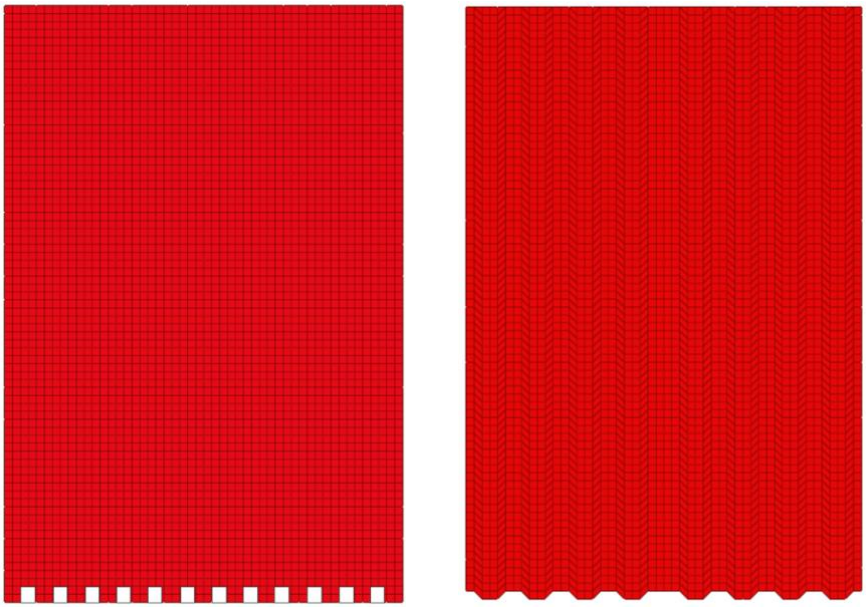

(a) **(b)**

Figure 3.8: *2 mm mesh with a boxed trigger (a) and 2 mm mesh with a boxed trigger and node offset (b)*

All models were benchmarked with an 850 J impact at an impact mass and velocity of 50 kg and 5.84 m/s respectively. The model with the wavy mesh encountered numerical issues due to the skewness of the elements. The time step for the model with a 4 mm mesh was approximately 0.0003 ms, which resulted in a total simulation time of approximately 10 minutes. Numerical parameters for this model were calibrated using the optimization methodology shown in section 5 (GRSM optimization algorithm and absolute difference response function) and the calibrated model showed good correlation with the experimental results as shown in Figure **3.9**. On the other hand, the time step for the model shown in Figure **3.8**a decreased by an order of magnitude

to approximately 0.00003 ms. Although progressive crush behavior was observed using this mesh geometry as well as shown in Figure **3.9**, the run time for the same loading case was in excess of 5 hours, which was significantly higher than that obtained using a 4 mm mesh. The parameters used for the 2 mm mesh size were the same as those used for the 4 mm mesh size and were not calibrated for the particular case, hence the correlation with experimental results was not as accurate as it was with the 4 mm mesh size. Calibrating the parameters for the 2 mm mesh, would have required running the optimization, which typically converged after 50 runs (250 hours running time). Given that the objective of the research was to use an optimization algorithm to determine certain numerical parameters, a process that requires several simulation runs to be undertaken by the software, and to have a methodology that could be used by FCA and other automobile manufacturers in the development of primary components made from composite materials, a 2 mm mesh size was considered inefficient as any resulting improvement in accuracy would have been offset by a manifold increase in computation time or power. Hence, a 4 mm mesh was used for the remaining part of the research. Typically a mesh size between 3 – 5 mm has been used in published literature to characterize the crashworthy behavior of large composite components and the same range of mesh sizes is used at FCA for full-scale numerical testing (22) (82) (94) (97).

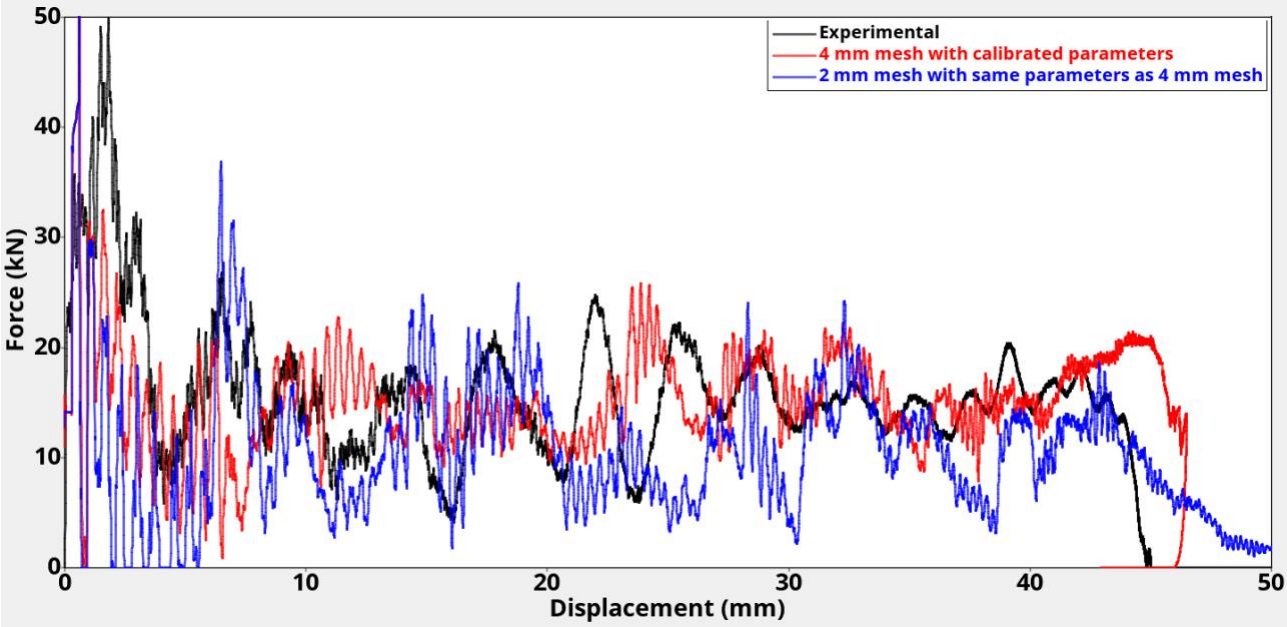

Figure 3.9: *Comparison of force-displacement curves for two different mesh sizes with experimental results*

3.2.2. Impact attenuator model

The impact attenuator was based on the crash box of a Formula SAE racing car that had been used extensively in published studies conducted at Politecnico di Torino and University of Camerino (82). The geometry was a truncated pyramid with rectangular cross-sections, round edges and increasing area. It was divided into three sections: 46 mm long top section made of two plies, 70 mm long middle section made of three plies and 100 mm long bottom section made of four plies as shown Figure **3.10**. The increasing area and thickness from the top to the bottom of the attenuator acted as triggers to initiate progressive crushing from the top. It was made

of the same material used to fabricate the flat plates and the material characterization specimens. The numerical model of the attenuator closely followed the process used for modelling the composite flat plates as the objective was to validate the numerical methodology and showcase its predictive capability by comparing the numerical and experimental results of drop test on a composite component. Hence, a macroscale and mesoscale model was developed for the attenuator as well and is described below.

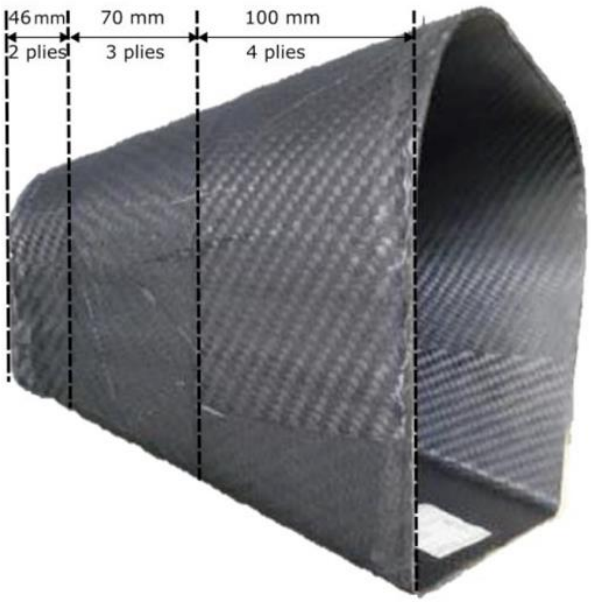

Figure 3.10: *CFRP impact attenuator (98)*

3.2.2.1. Macroscale model

The macroscale model was comprised of three components: the composite attenuator, the falling steel plate (impactor) and the steel base on top of which the attenuator sat. Material and property law 1 were used to model the metallic components, whilst material law 25 and property law 11were used to model the composite attenuator. Three different properties were created to accommodate the varying ply layups. Although, the thickness of the plies for the composite flat plate was 0.64 mm, using the same ply thickness resulted in an attenuator mass of 461 grams, which was significantly below the actual mass of the attenuator (539 grams). Wall thicknesses of the physical impact attenuator were then measured, revealing that the ply thickness was 0.75 mm for the top and middle sections and 0.77 mm for the bottom section. The updated thicknesses resulted in a good match between the physical and numerical masses. Rigid body elements were applied to the impactor and the bottom plate. Boundary conditions applied to the bottom plate ensure no translation or rotational DoFs, whilst those applied to the impactor ensured only translation in the x-direction. Both the impactor and the bottom plate were made sufficiently large so as not to allow any parts of the attenuator to "spill" out upon impact as it exhibited fronding and fragmentation failure modes. The interfaces between the impactor and attenuator, base and attenuator and amongst the elements of the attenuator were modelled using type 7 contacts. The mesh size was kept consistent from the flat plate model at 4 mm. However, due to the geometry, triangular elements had to be added in order to obtain an acceptable mesh without any failed or excessively skewed elements. Only half the attenuator was meshed, and the mesh was then mirrored along the plane of symmetry

to ensure that the mesh was symmetric as shown in Figure **3.11**b. This ensured that no torsional forces were introduced due to an asymmetric mesh. The top and bottom plates were meshed with a 5 mm element size, similar to that used in the flat plate model. The entire model was made of approximately 14,000 elements and 64,500 DoFs, of which the attenuator was composed of 62 triangular and approximately 10,200 quadrilateral elements. As no DoFs were restricted for the attenuator, its nodes made up most of the DoFs available for the entire model (62,700 DoFs). The final model is shown in Figure **3.11**a.

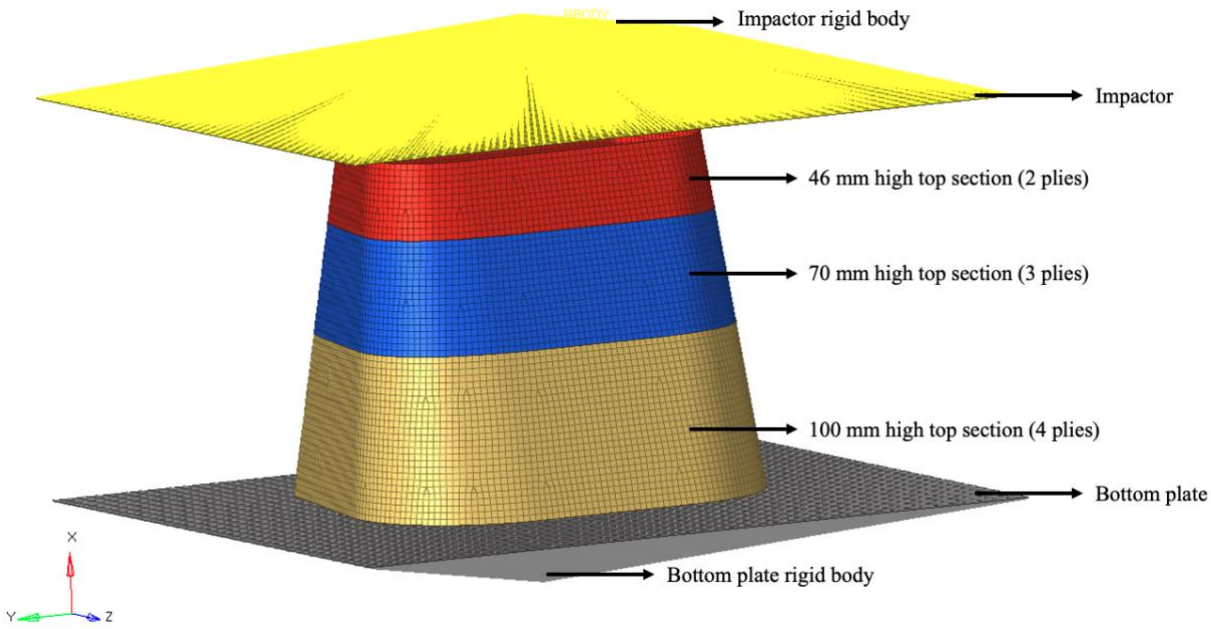

(a)

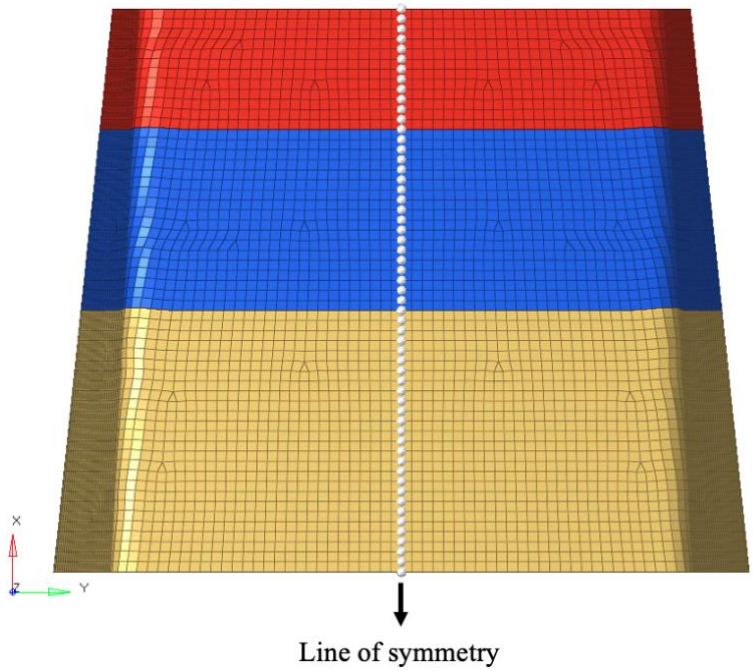

(b)

Figure 3.11: *Macroscale model of the impact attenuator (a); Symmetry plane for the impact attenuator (b)*

3.2.2.2. Mesoscale model

As was the case with the flat plate model, 3D cohesive elements were added to the impact attenuator model to simulate delaminations between the plies. Instead of a single layer of shell elements, plies in each section were modelled using separate layers of shell elements spaced 0.75 mm apart. Cohesive layers of solid elements, 0.75 mm thick, were added between the plies: a single layer for the top section, two layers for the middle section and three layers for the bottom section as shown in Figure **3.12**. Although the thickness of the plies in the bottom section was 0.77 mm, the cohesive elements were 0.75 mm thick to avoid a mismatch between the nodes at the interface between the middle and bottom section that led to non-physical failure of the plies when the solid elements in the bottom section were modelled as 0.77 mm thick. In order to avoid penetrations between the layers since the thickness was 0.77 mm and the gap between them was 0.75 mm, a flag was activated in the contact card that numerically shifted the nodes that the software identified to be penetrated. This is further explained in section 3.5.3. Unlike the flat plate model in which all cohesive elements were hexahedrons, triangular prisms were used for the impact attenuator mesoscale model due to the presence of triangular elements in the shell layers. Cohesive elements were modelled with material laws 59 (Connect) and Fail_Connect and property type 43 (Connect), similar to what was done for the flat plate model. All nodes of the cohesive elements were merged with those of the shell elements; hence no additional interface was needed. The interface between the elements of the plies was changed to type 24 contacts to accurately capture the interactions between the plies as type 7 contact resulted in numerical penetrations. The model was made of 62,000 elements and 213,000 DoFs, of which the impact attenuator was made of 58,000 elements and 211,000 DoFs.

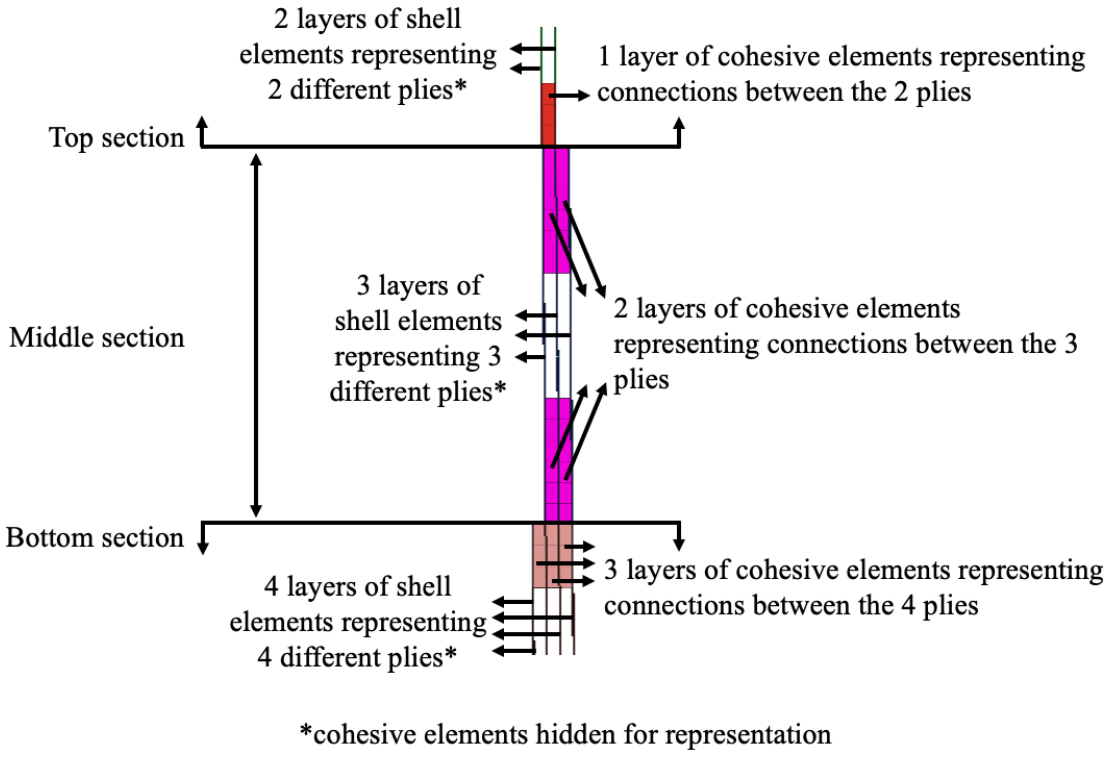

Figure 3.12: *Cross-section of the impact attenuator (98)*

3.3. Material cards

The preceding section in this chapter provided an overview of the methodology followed for macroscale and mesoscale modelling of the flat plate and impact attenuator models. This section provides details about the three material cards used across the models, their underlying material laws, the inputted parameters, and determination/identification and validation of these parameters. Two different material cards were used to model the behavior of C40 Steel used for metallic components. First law 2 (Johnson-Cook Elastoplastic) was used to determine the thickness of the top plate of the fixture that did not lead to plastic deformation at the highest impact energy level generated by the Instron 9400 drop tower series (1800 J). Once it was established that no plastic deformation would occur, the simplified law 1 (Elastic) was used. CRASURV formulation of the law 25 (Composite Shell) was used to model the behavior of the GG630T-37 Carbon Fiber Epoxy 2 x 2 twill material (99). The composite material was a prepreg laminate with a fiber volume fraction of 0.55 and plies that were 0.64, 0.75 and 0.77 mm thick. Law 59 was combined with Fail_Connect to model the cohesive material, as the material card did not have any inbuilt failure criteria. Specific parameters used for each of the material cards are summarized at the end of each material card description.

3.3.1. Law 2 – Johnson-cook elastoplastic

Law 2 is based on the Johnson-Cook material model that models stress as a function of strain, strain rate and temperature and has since been used to model metallic elastoplastic behavior in various published studies (100) (101). It models the behavior as linearly elastic until the equivalent stress is lower than the plastic yield stress, after which it is modelled as plastic and governed by the Equation 3.1 below (102).

$$\sigma = \left(a + b\varepsilon_p^n\right)\left(1 + c\ ln\frac{\dot{\varepsilon}}{\dot{\varepsilon}_0}\right)(1 - (T^*)^m) \qquad 3.1$$

Strain-rate and temperature effects were not considered for the study as the range of velocities tested was between 4 – 8 m/s, a range too narrow to observe any significant strain-rate effect, and all tests were conducted at room temperature (103). Strain-rate effects that may have occurred due to the geometry were ignored. Hence, no values were attributed to parameters for the same. Values for all other parameters were obtained from the Total Materia Database as shown in Table **3.1** (104). The law has built-in failure criteria based on maximum plastic strain or stress, upon reaching which the respective element is deleted.

Table 3.1: C40 Steel material parameters and properties for Johnson-Cook Elastoplastic material card (102)

Flag	Definition	Determination	Input Value
ρ_i	Density	Total Materia Database (104)	7.85 10x^{-6} g/mm^3
E	Young's modulus	Total Materia Database (104)	202 GPa
ν	Poisson's ratio	Total Materia Database (104)	0.3
$Iflag$	Flag to use classical parameters (a, b, n) or simplified parameters (Yield stress, ultimate engineering stress (UTS), strain at UTS)	0 for classical parameters 1 for simplified parameters	0
a	Yield stress	Total Materia Database (104)	230 MPa
b	Hardening parameter	Total Materia Database (104)	0.7
n	Hardening exponent	Total Materia Database (104)	0.4
ε_p^{max}	Failure plastic strain	Total Materia Database (104)	0.16
σ_{max0}	Maximum stress	Total Materia Database (104)	560 MPa

3.3.2. Law 1 – Hooke's elastic (simplified law 2)

Law 1 is based on the Hooke's law and models only the elastic behavior, as compared to Law 2, which modelled both the elastic and plastic behavior. As was the case for Law 2 the parameters required were obtained from the Total Materia database for C40 steel, shown below in

Table 3.2, whilst shear modulus is calculated using Equation 3.2. It was only applied once it was certain that the steel material underwent solely elastic deformations under the maximum loading of 1800 J.

$$G = \frac{E}{2(1+\nu)} \tag{3.2}$$

Table 3.2: *C40 Steel material parameters and properties for Elastic material card (102)*

Flag	Definition	Determination	Input Value
ρ_i	Density	Total Materia Database (104)	7.85 10x^{-6} g/mm^3
E	Young's modulus	Total Materia Database (104)	202 GPa
ν	Poisson's ratio	Total Materia Database (104)	0.3

3.3.3. Law 25 – Composite shell (CRASURV formulation)

Of the several material cards laws available within Radioss that can be used to model composite materials, only Law 15 and 25 were suitable to the application at hand: modelling dynamic non-linear impact behavior of components made from woven or UD quasi-isotropic/orthotropic composite material. Plasticity model in law 15 is based on the Tsai-Wu formulation and the Chang-Chang failure criterion is built into the material law. Plasticity model in law 25 is based on the CRASURV formulation which is a modified form of the Tsai-Wu formulation that allows for definition of yield limits for each orthotropic direction in tension, compression and shear and the failure criterion is based on tensile strain and maximum plastic work, which can also be defined for each orthotropic direction in tension, compression and shear. Due to the availability of a greater number of parameters to control the composite behavior and its robustness, law 25 with CRASURV formulation was chosen for the study.

The Tsai-Wu failure criterion is a specialization of the generalized quadratic failure criterion proposed by Gol'denblat and Kopnov, where failure occurs if the left-hand side of equation 3.3 exceeds 1 (105). Equation 3.3 is specialized for the lamina, in that the stresses considered are plane stresses. The F_{ij} factors are functions of the maximum stresses as shown in equations 3.4 – 3.9. For the CRASURV formulation, these maximum stresses are in-turn a function of the plastic work (energy absorbed) per unit volume (W_p) and strain rate ($\dot{\varepsilon}$), for all three loading scenarios: tension (equation 3.10), compression (equation 3.11)and shear (equation 3.12). Equations 3.10 – 3.12 are of the Johnson-Cook type, with the hardening parameter, b, a function of the energy absorbed, W_p, and with the temperature effects ignored. This is not the case for the classical Tsai-Wu criterion; hence the criterion transforms to the one shown in equation 3.13, resulting in a criterion with second order

closed 3D Tsai-Wu surface in σ_1, σ_2 and σ_{12} space, where 1 and 2 are the orthotropic directions of the lamina. This surface can be scaled, moved or rotated by varying the energy absorbed or the strain rate, ultimately allowing the user greater control over modelling the failure.

$$F_1\sigma_1 + F_2\sigma_2 + F_{11}\sigma_1^2 + F_{22}\sigma_2^2 + F_{44}\sigma_{12}^2 + 2F_{12}\sigma_1\sigma_2 < 1 \quad 3.3$$

$$F_1 = -\frac{1}{\sigma_{1u}^c} + \frac{1}{\sigma_{1u}^t} \quad 3.4$$

$$F_2 = -\frac{1}{\sigma_{2u}^c} + \frac{1}{\sigma_{2u}^t} \quad 3.5$$

$$F_{11} = \frac{1}{\sigma_{1u}^c \sigma_{1u}^t} \quad 3.6$$

$$F_{22} = \frac{1}{\sigma_{2u}^c \sigma_{2u}^t} \quad 3.7$$

$$F_{44} = \frac{1}{\sigma_{12u}^c \sigma_{12u}^t} \quad 3.8$$

$$F_{12} = -\frac{\alpha}{2}\sqrt{F_{11}F_{22}} \quad 3.9$$

$$\sigma_{iu}^t\left(W_p^*, \dot{\varepsilon}\right) \Rightarrow \sigma_{iu}^t\left(1 + b_i^t\left(W_p^*\right)^{n_i^t}\right)\left(1 + c_i^t ln\left(\frac{\dot{\varepsilon}}{\dot{\varepsilon}_0}\right)\right) \quad 3.10$$

$$\sigma_{iu}^c\left(W_p^*, \dot{\varepsilon}\right) \Rightarrow \sigma_{iu}^c\left(1 + b_i^c\left(W_p^*\right)^{n_i^c}\right)\left(1 + c_i^c ln\left(\frac{\dot{\varepsilon}}{\dot{\varepsilon}_0}\right)\right) \quad 3.11$$

$$\sigma_{12u}\left(W_p^*, \dot{\varepsilon}\right) \Rightarrow \sigma_{12u}\left(1 + b_{12}\left(W_p^*\right)^{n_{12}}\right)\left(1 + c_{12}\, ln\left(\frac{\dot{\varepsilon}}{\dot{\varepsilon}_0}\right)\right) \quad 3.12$$

$$F_1\left(W_{p,1}, \dot{\varepsilon_1}\right)\sigma_1 + F_2\left(W_{p,2}, \dot{\varepsilon_2}\right)\sigma_2 + F_{11}\left(W_{p,1}, \dot{\varepsilon_1}\right)\sigma_1^2 + F_{22}\left(W_{p,2}, \dot{\varepsilon_2}\right)\sigma_2^2 + F_{44}\left(W_{p,12}, \dot{\varepsilon_{12}}\right)\sigma_{12}^2 + 2F_{12}\left(W_p, \dot{\varepsilon}\right)\sigma_1\sigma_2 < 1 \quad 3.13$$

Energy absorbed is the area under the stress-strain graph during plastic deformation, which includes the energy absorbed during softening as shown in Figure **3.13**a. Fiber-reinforced composite materials, due to their brittle behavior, do not exhibit any material hardening and plasticity post-yield in tension and compression when these loadings are along the orthotropic directions, whilst the behavior is non-linear for all other cases such as shear loadings. Energy absorbed during loadings that result in non-linear stress-strain behavior constitute absorption as a result of plastic work, shown by areas 1 and 3, and elastic work, shown by area 2 in Figure **3.13**a. Area 1 is the energy absorbed during plasticity and area 3 is the energy absorbed during damage and

softening. On the other hand, energy absorbed during loadings that result only in linear stress-strain behavior constitute absorption as a result of only elastic work.

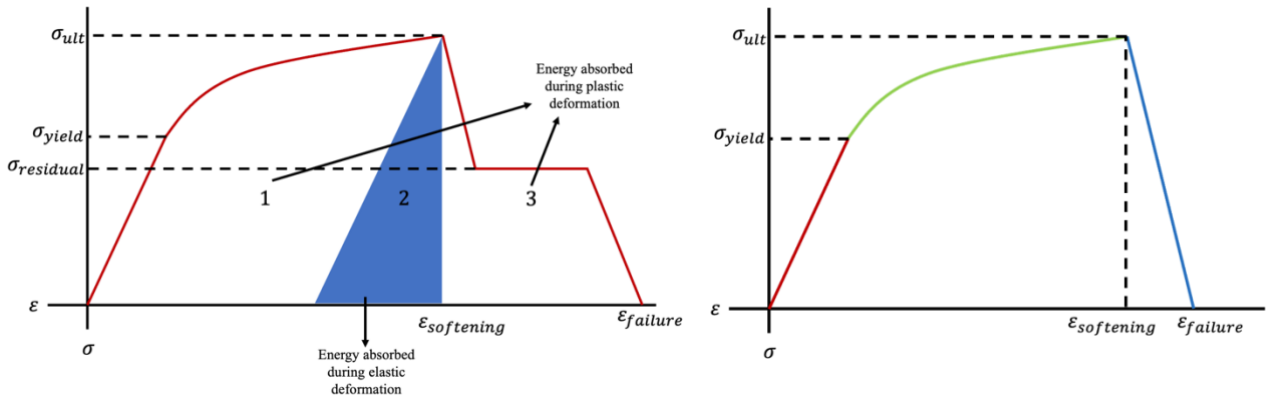

Figure 3.13: *Energy absorbed failure parameter and softening with residual stress (a); softening without residual stress (b)*

The formulation allows for softening after damage, which can either be a linear softening until failure strain as shown in Figure **3.13**b or until residual stress as shown in Figure **3.13**a. Residual stress is the residual stress bearing capacity of the element after ultimate stress or damage and it eventually drops to zero once all the energy has been absorbed or the failure strain has been reached, after which the element is deleted. Element deletion is governed by the I_{off} parameter whose value can be set between 0 and 6 as described below. Case 5 is the most accurate representation as it encompasses all possible scenarios and assigns a degree of preference to them, whilst case 6 is the most robust one since it avoids any numerical instability and artificial strengthening that may arise due to non-deletion of one of the layers in the stacked shell but still incorporated all possible scenarios.

- 0: shell is deleted if energy absorbed is greater than maximum energy absorbed for one element
- 1: shell is deleted if energy absorbed is greater than maximum energy absorbed for all element layers
- 2: shell is deleted if energy absorbed is greater than maximum energy absorbed, or tensile strain is greater than maximum tensile strain in 1 direction for each layer
- 3: shell is deleted if energy absorbed is greater than maximum energy absorbed, or tensile strain is greater than maximum tensile strain in 2 direction for each layer
- 4: shell is deleted if energy absorbed is greater than maximum energy absorbed, or tensile strain is greater than maximum tensile strain in 1 and 2 directions for each layer
- 5: shell is deleted if energy absorbed is greater than maximum energy absorbed, or tensile strain is greater than maximum tensile strain in 1 or 2 directions for all layers
- 6: shell is deleted if energy absorbed is greater than maximum energy absorbed, or tensile strain is greater than maximum tensile strain in 1 or 2 directions for each layer

The entire material card could be divided into seven broad components: setup, elastic, plastic, softening, damage, strain rate and delamination, based on the type of parameters that are inputted. The parameters and their definition, determination and input values are mentioned in Table **3.3** - Table **3.7**. The range of velocities

tested was between 4 – 8 m/s, a range too narrow to experience significant strain rate effects on the mechanical properties of composite materials (106). Jacob et al. and Savage concluded that any strain rate dependency of the material had insignificant effect on its crashworthiness for high loading scenarios such as the ones presented in this study (107) (108). These conclusions were supported by the experimental data obtained that showed no strain rate effects for the material and geometry used for impact energies up to 850 J, after which it was not possible to test the specimen as this energy level resulted in the specimen undergoing 50 mm of stroke displacement, which was the maximum allowable stroke displacement for the fixture (48) (95) (98). Experimental data also confirmed no effect of strain rate for the range of velocities mentioned above for the type of geometries used: flat plate and pyramid of rectangular cross-section with curved edges. Hence, strain rate effects were not modelled, and the related parameters were left blank. The material card also had a built-in delamination model, which was not used due to its over simplicity. Thereby, the related parameters were not incorporated.

Table 3.3: *GG630T-37 Carbon Fiber Epoxy setup parameters for the composite material card*

Flag	**Definition**	**Determination**	**Input Value**
ρ_i	Density	Rule of Mixtures verified with physical measurement using $\frac{Mass}{Volume}$	1.34 x 10^{-6} g/mm^3
I_{form}	Formulation type	0 for Tsai-Wu formulation 1 for CRASURV formulation	1

Properties in 1 and 2 directions were assumed equal due to the quasi-isotropic nature of the material. It is well known that the behavior of fiber-reinforced composite materials is brittle under tension and compressive loading in the orthotropic directions. As can be seen from Figure **3.14**a and Figure **3.14**b, the tensile and compressive material characterization curves exhibited slight curvature as the strain increased.

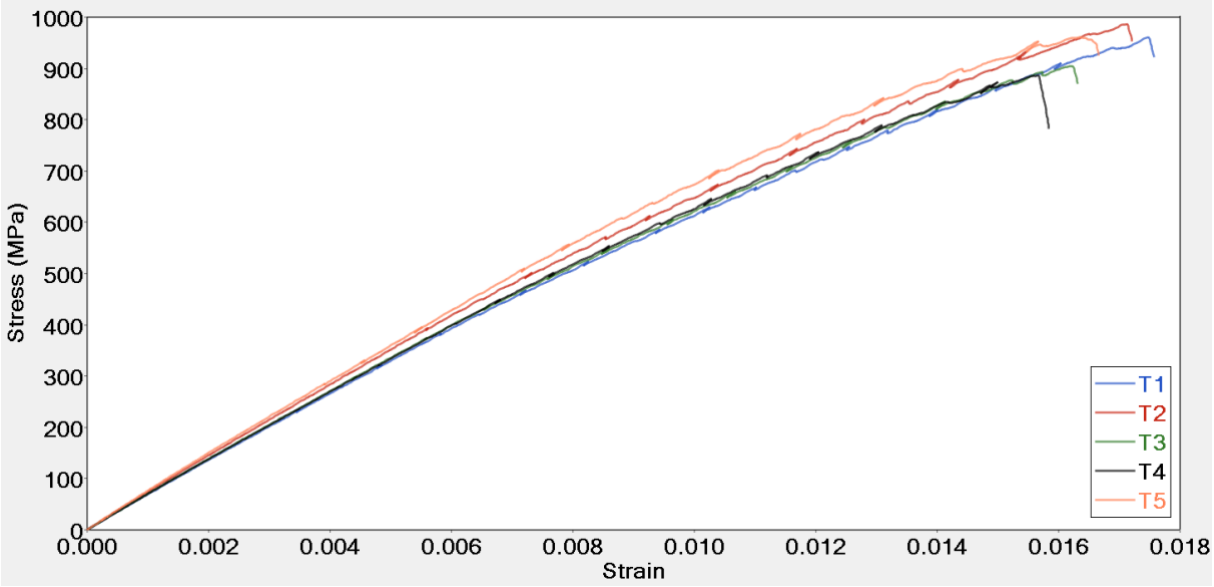

(a)

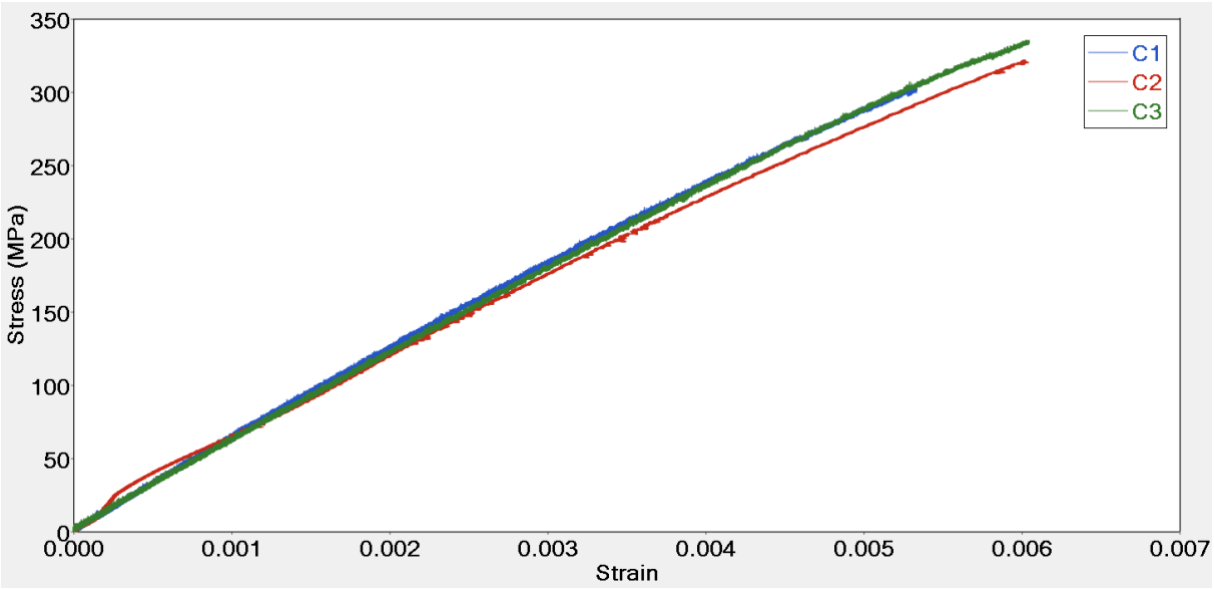

(b)

Figure 3.14: *Stress-strain results of material characterization tests under tension (a) and compression loading (b) (95)*

As tensile failure is fiber dominated and fibers are brittle in nature and do not exhibit any plasticity, a gradual decrease in the tensile Young's modulus with each stepwise increase in strain occurred due to the failure of individual fibers or fiber tows and the fiber-matrix interface. Compressive failure, on the other hand, is matrix dominated so the decrease in compressive Young's modulus was probably due to matrix and interface cracking or debonding of the fibers from the matrix. In order to accurately model the abovementioned behaviors, a multiscale approach would be ideal. However, using such an approach would be computationally expensive, especially at a component scale. Additionally, multiscale modelling in HyperWorks is still under development. Hence, two different approaches were modelled to represent tensile behavior. The first was to model part of the stress-strain graph as elastic and part of it as plastic (after the point that it starts to deviate from linearity)

using a hardening parameter and exponent in order to capture the microscale behavior. The second was to model it as purely elastic and disregard the microscale damage. This resulted in two different Young's moduli and the inclusion of hardening parameter and exponent as seen in

Table **3.4** and Table **3.5**. The effect of modelling tensile behavior using two different approaches was also assessed to obtain the one that modelled crushing behavior accurately and is shown in section 5.4. Such an approach was not necessary for compressive behavior as compression failure is matrix dominated, which behaves in an elastoplastic manner.

Parameters obtained through experimental characterization tests (ASTM D3039 – tension, ASTM D3410 – compression, and ASTM D3518 – shear) were obtained from stress-strain data provided by Babaei (95). A curve was chosen to represent the material behavior under tensile, compressive and shear loading to input data into the material card and to ensure correlation between the numerical and experimental characterization curves. Under tensile loading, as can be seen from Figure **3.14**a, the curves of specimens T1, T3 and T4 overlap, but the specimen failed at different levels of stress due to slight variations in the material. Specimens T2 and T5 not only failed at different levels of stress, but also exhibited higher Young's moduli, hence they were not considered as representative of the material behavior. Of the three curves mentioned earlier, specimen T3 failed at a stress level that was between that of specimens T1 and T4. Hence, specimen T3's results were chosen as the representative curve. Under compressive loading (Figure **3.14**b), specimen C2 exhibited a slight bump at the start, possibly due to issues with the strain gauge, whilst specimen C1 failed prematurely. Specimens C1 and C3 exhibited equal Young's moduli, whilst C2 and C3 exhibited equal failure stress. Hence, specimen C3's results were chosen as the compressive representative stress-strain data. Under shear loading, as shown in Figure **3.15**, specimen S3 failed prematurely and specimen S4 exhibited lower moduli and strength as compared to the other three specimens. The stress-strain curves of specimens S1 and S2 almost overlapped. Hence, specimen S2's results were chosen as the representative curve.

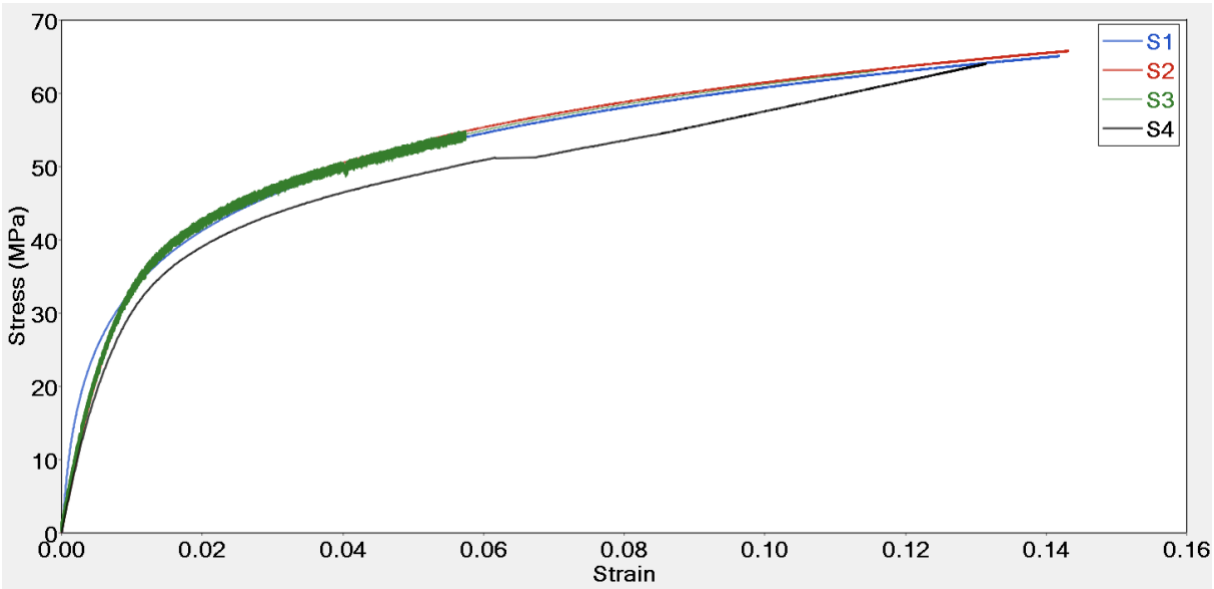

Figure 3.15: *Stress-strain curves of material characterization tests under shear loading*

Table 3.4: *GG630T-37 Carbon Fiber Epoxy elastic material properties and parameters for the composite material card*

Flag	Definition	Determination	Input Value
E_{11}, E_{22}	Young's modulus in 1 and 2 directions	From experimental stress-strain representative curve	60 GPa (Elastoplastic formulation) 70 GPa (Elastic formulation)
ν_{12}	Poisson's ratio	From experimental data	0.3
E_{33}	Young's modulus in 3 direction	Not available	--
G_{12}	Shear modulus in 12 direction	From experimental stress-strain representative curve	4 GPa
G_{23}	Shear modulus in 23 direction	Not available	--
G_{31}	Shear modulus in 31 direction	Not available	--

Table 3.5: *GG630T-37 Carbon Fiber Epoxy plastic material properties and parameters for the composite material card*

Flag	Definition	Determination	Input Value
σ_{1y}^{t}, σ_{2y}^{t}	Tensile yield stresses in 1 and 2 direction	From experimental stress-strain representative curve	120 MPa (Elastoplastic formulation) 911.5 MPa (Elastic formulation)
b_1^t, b_2^t	Tensile plastic hardening parameters in 1 and 2 directions	By calibrating (manual trial-and-error) numerical stress-strain curve to correlate with the experimental stress-strain representative curve	35 (Elastoplastic formulation)
n_1^t, n_2^t	Tensile plastic hardening exponents in 1 and 2 directions	By calibrating (manual trial-and-error) numerical stress-strain curve to correlate with the experimental stress-strain representative curve	0.275 (Elastoplastic formulation)
σ_{1max}^{t}, σ_{2max}^{t}	Tensile maximum stresses in 1 and 2 directions	From experimental stress-strain representative curve	911.5 MPa (Both formulations)
σ_{1y}^{c}, σ_{2y}^{c}	Compressive yield stresses in 1 and 2 directions	From experimental stress-strain representative curve	55 MPa

b_1^c, b_2^c	Compressive plastic hardening parameters in 1 and 2 directions	By calibrating (manual trial-and-error) numerical stress-strain curve to correlate with the experimental stress-strain representative curve	500
n_1^c, n_2^c	Compressive plastic hardening exponents in 1 and 2 directions	By calibrating (manual trial-and-error) numerical stress-strain curve to correlate with the experimental stress-strain representative curve	0.55
σ_{1max}^c, σ_{2max}^c	Compressive maximum stresses in 1 and 2 directions	From experimental stress-strain representative curve	334 MPa
σ_{12y}	Shear stress in 12 direction	From experimental stress-strain representative curve	10 MPa
b_{12}	Shear plastic hardening parameter in 12 direction	By calibrating (manual trial-and-error) numerical stress-strain curve to correlate with the experimental stress-strain representative curve	10
n_{12}	Shear plastic hardening exponents in 12 direction	By calibrating (manual trial-and-error) numerical stress-strain curve to correlate with the experimental stress-strain representative curve	0.145
σ_{12max}	Shear maximum stress in 12 direction	From experimental stress-strain representative curve	65 MPa

For softening, residual stresses were incorporated into the material card under compression and shear loading, but not for tensile loading as tensile behavior does not have a significant effect on the crushing behavior. Softening under tensile loading was linear until zero stress and maximum strain, after which the element was deleted at failure strain. The maximum strain value for elastic formulation was marginally lower than that for elastoplastic formulation because of a higher Young's modulus for the former that resulted in the maximum/ultimate stress being reached at a lower strain level. The values for the softening stresses were identified using an optimization procedure developed as a part of this research work and is explained in detail in section 5. Table **3.6** mentions the softening strains and stresses used in the material card.

Table 3.6: *GG630T-37 Carbon Fiber Epoxy softening material properties and parameters for the composite material card*

Flag	**Definition**	**Determination**	**Input Value**
ϵ_1^{t1}, ϵ_2^{t1},ε_{t1}, ε_{t2}	Tensile initial softening strain in 1 and 2 directions	From experimental stress-strain representative curve	0.01644 (Elastoplastic formulation) 0.0152 (Elastic formulation)
ϵ_1^{t2}, ϵ_2^{t2}, ε_{m1}, ε_{m2}	Tensile maximum softening strain in 1 and 2 directions	110% of the initial softening strain as advised by the reference manual to ensure smoothing without numerical instabilities	0.018084 (Both formulations)
σ_{rs}^{t1}, σ_{rs}^{t2}	Tensile residual stress in 1 and 2 directions	Not applied as the material was degraded linearly until zero stress level	--
ϵ_1^{c1}, ϵ_2^{c1}	Compressive initial softening strain in 1 and 2 directions	From experimental stress-strain representative curve	0.00604
ϵ_1^{c2}, ϵ_2^{c2}	Compressive maximum softening strain in 1 and 2 directions	Not applied as compressive damage dominated by maximum energy absorption	--
σ_{rs}^{c1}, σ_{rs}^{c2}	Compressive residual stresses in 1 and 2 directions	Using optimization procedure	Refer to section 5

ϵ_{12}^{1}	Shear initial softening strain in 12 direction	From experimental stress-strain representative curve	0.073
ϵ_{12}^{2}	Shear maximum softening strain in 12 direction	Not applied as compressive damage dominated by maximum energy absorption	--
σ_{12rs}	Shear residual stress in 12 direction	Using optimization procedure	Refer to section 5

Element deletion was governed by strain for tensile failure and energy absorption for failure other than tensile failure. Although individual energy absorption terms were available for compression and shear, they were not used as the global energy absorption parameter was encompassing of them. Table **3.7** mentions the element deletion parameters

Table 3.7: *GG630T-37 Carbon Fiber Epoxy failure material properties and parameters for the composite material card*

Flag	**Definition**	**Determination**	**Input Value**
ε_{f1}, ε_{f2}	Maximum tensile strain for element deletion in 1 and 2 directions	120% of the initial softening strain as advised by the reference manual to ensure smoothing without numerical instabilities	0.019728 (Both formulations)
W_p^{max}	Maximum global energy absorbed per unit volume	Using optimization procedure	Refer to section5
I_{off}	Flag for deletion	0 – 6 as described above	5 (Most accurate)

3.3.3.1. Calibration and validation of physical parameters

In order to calibrate the hardening parameters and ensure cohesion between the experimental and numerical characterization results, single element tests were conducted. Three quadrilaterals, 4 mm in size, were meshed to represent tension, compression and shear loading. Material law 25 and property type 11 were used to model the elements. The elements were constrained at the bottom nodes in the z-direction as shown in Figure **3.16**. No rotational DoFs were constrained in order to observe any bending or torsional behavior that may have been introduced due to errors in material card inputs. A constant displacement of 0.1 mm/ms was applied to the top nodes of each of the elements to simulate behavior similar to that observed in experiments as per ASTM standards as shown in Figure **3.17**. Displacement was in the positive z-direction (1 direction) for tension and shear loading and in the negative z-direction for compression loading, akin to experiments. As the CFRP

material used was quasi-isotropic in nature, no testing was conducted with the displacement in the weft direction (2 direction).

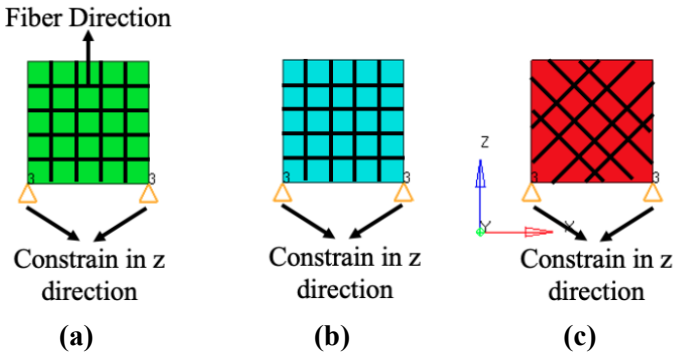

Figure 3.16: Constrains applied to single element test elements

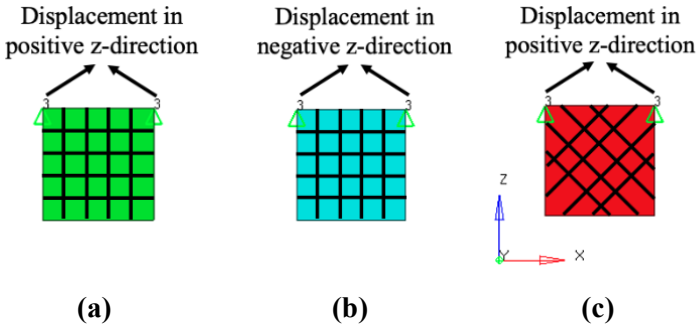

Figure 3.17: Displacements applied to single element test elements

The final tests did not exhibit any bending or torsional behavior, thereby confirming that the individual element sizes was not too coarse and did not induce any unwanted failure mechanisms. As mentioned earlier, numerical results were compared with the representative experimental stress-strain curve for tension, compression and shear loading and the results are shown in Figure **3.18** (tension), Figure **3.19** (compression) and Figure **3.20** (shear) and a good correlation was observed for all three loading scenarios, hence confirming that the numerical material behaved in a manner similar to that observed in the experimental characterization campaign. Residual stresses shown for compression and shear cases were set arbitrarily for demonstration purposes and were calibrated using the optimization procedure detailed in section 5.

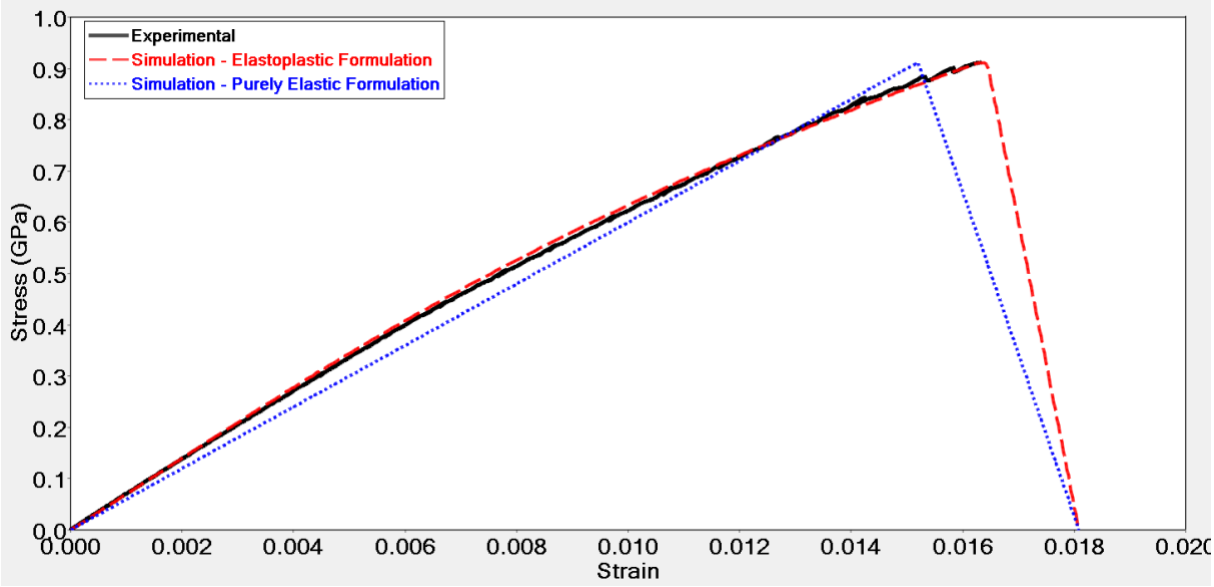

Figure 3.18: *Comparison of numerical and experimental characterization test results under a tensile load*

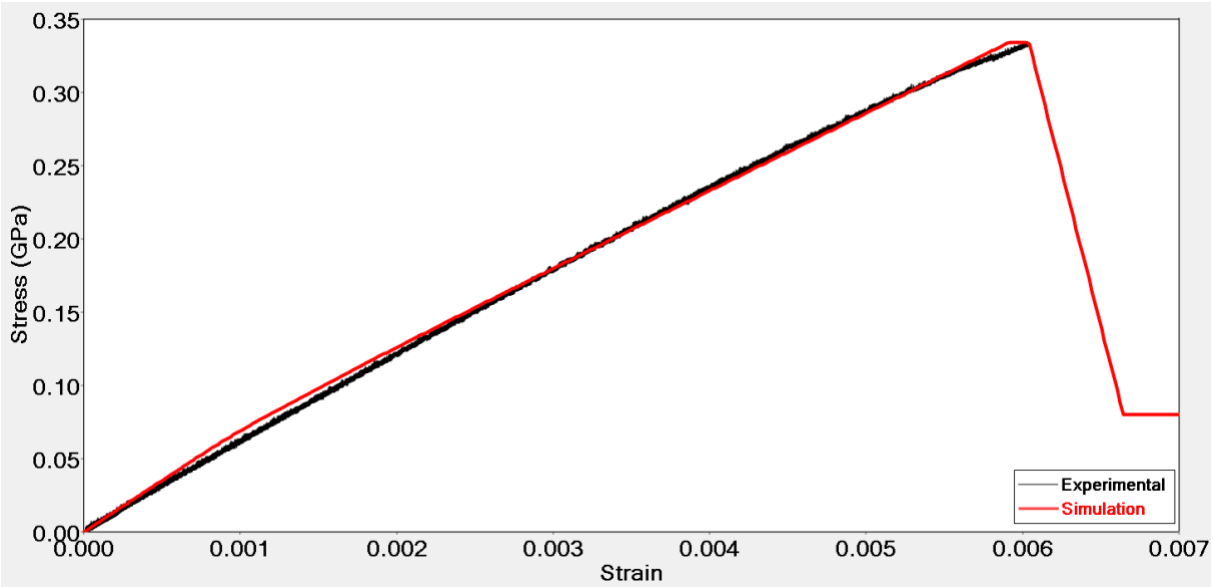

Figure 3.19: *Comparison of numerical and experimental characterization test results under a compressive load*

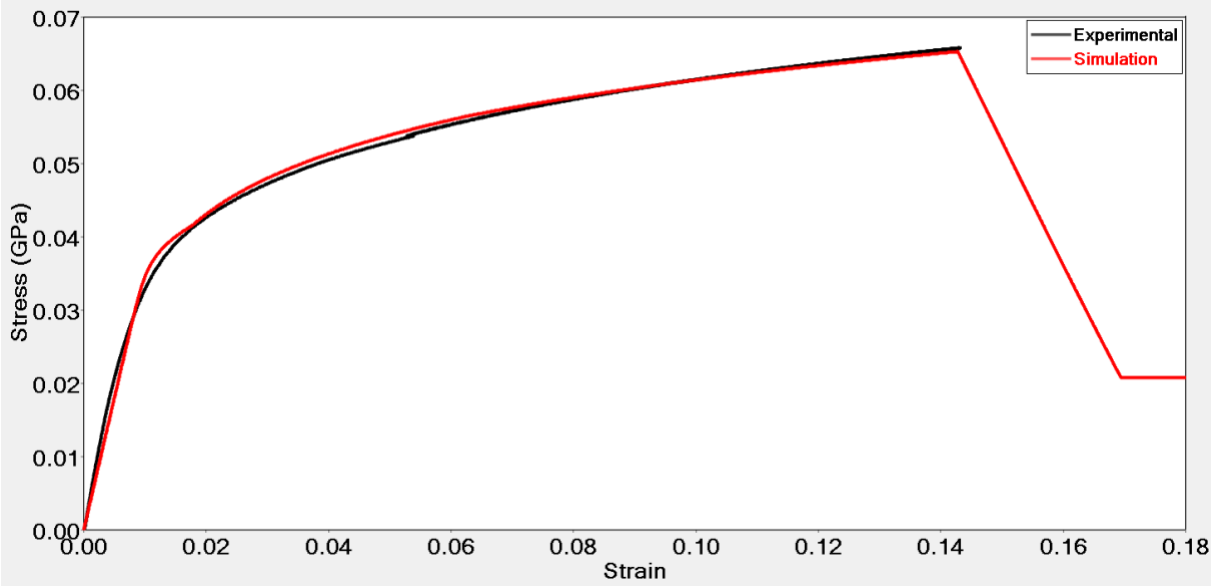

Figure 3.20: *Comparison of numerical and experimental characterization test results under a shear load*

3.3.4. Law 59 – Cohesive material

The cohesive layer was modelled using law 59, which allows for modelling elastic and elastoplastic behavior in normal and shear directions (102). Elastic behavior is modelled using the Hooke's law and elastoplastic behavior is incorporated by adding a stress-strain function post-yield. Stress was assumed constant post-yield until failure to avoid numerical instability introduced when stress is reduced after yield. Hence the stress-strain graph was a rising slope (elastic region) followed by a plateau (plastic region) that terminated at the maximum strain value, at which point the stress dropped to zero. As no experimental testing was done to characterize the epoxy used and no material data sheet was available for the same, values for Young's modulus (tension and compression) and shear moduli, yield stress and failure strain were obtained from literature (109) (110) (111). Due to this it was assumed that the properties of the adhesive layer were equal to the properties of epoxy. Since the material card did not have a built-in failure card, Fail_Connect card that could model failure as either strain- or energy-based was linked with the cohesive material card. To incorporate energy-based failure, DCB and ENF testing needed to be conducted in order to obtain the critical strain energy release rates under failure modes I and mode II, respectively, which are then used as benchmarks to calibrate the energy-based failure parameters (19) (87) (112). Since no such testing was conducted, a strain-based failure was used instead, values for which were obtained from the aforementioned literature. Table **3.8** lists the parameters used to model the cohesive behavior and its failure, and the values used.

Table 3.8: *Cohesive material and failure parameters and properties*

Flag	**Definition**	**Input Value**
E	Young's modulus	3.2 GPa
G	Shear modulus	2 GPa

E_{comp}	Compression modulus	8 GPa
σ_y	Yield stress	75 MPa
ε_f	Failure strain in normal direction	0.045
I_{fail}	0 – unidirectional failure 1 – multi-directional failure	1

3.4. Property cards

This section details the three property cards used across the models, the inputted parameters, and determination/identification of these parameters. Property type 1 (shell) was used to model the metallic components for both the macroscale and mesoscale models. Property type 11 (composite shell) was used to model the composite flat-plate and impact attenuator and define their respective layup configurations amongst other parameters. Property type 43 (connect – solid) was introduced for the mesoscale models to define the cohesive layer elements. No particular parameters were needed to be input for property type 43 except for activation of the small strain formulation flag. Specific parameters used for each of the material cards are summarized at the end of each material card description.

3.4.1. Property type 1 (shells) – for metallic components

All metallic components were made from shell elements only and their shell formulation, properties and thicknesses were described using property type 1. Since fully integrated Batoz elements were used, there was no need to define the hourglassing and damping coefficients. Table **3.9** details all the parameters used and their respective inputs.

Table 3.9: *Property type 1 (metals) parameters and inputs*

Flag	Definition	Determination	Input Value
I_{shell}	4 node shell element formulation flag	1 – Under-integrated Belytshko & Tsay formulation elements with 1 integration point on the surface 2 – 1st formulation without orthogonality 3 – 1st formulation with orthogonality and elasto-plastic hourglass stabilization 4 – 1st formulation with full hourglass stabilization (most efficient)	12 (fully integrated elements are desired)

		12 – Full-integrated Batoz formulation elements with 4 integration points on the surface, no artificial hourglassing stabilization (most accurate, least efficient due to high computation cost) 24 – Improved under-integrated Belytshko & Tsay formulation elements with 1 integration point on the surface and hourglass stabilization (best compromise between accuracy and efficiency)	
I_{smstr}	Shell small strain formulation flag	1 – small strain from t = 0 2 –full geometric nonlinearities with possibility of activating small strain formulation if needed 3 – old formulation 4 – full geometric nonlinearities without the possibility of activating small strain formulation	2
N	Number of integration points through-thickness	Minimum 3 is recommended	3 – anti-buckling supports and impactor 5 – top and bottom plates (more integration points because optimization conducted)
I_{strain}	Compute strains for post-processing flag	1 – Yes 2 – No	1
$Thick$	Thickness	Based on the model	Top plate – 30 mm (10 – 30 mm in increments of 5 mm for determination of optimum thickness) Bottom plate – 20 mm Anti-buckling supports – 2 mm Hemispherical and flat impactor – 5 mm

I_{thick}	Resultant stress formulation flag	1 – Thickness change is taken into account 2 – Thickness change is not taken into account	1
I_{plas}	Plane stress plasticity flag	1 – Iterative projection with 3 Newton iterations (for metallic materials) 2 – Radial return (for composite materials)	1

3.4.2. Property type 11 (shell sandwich) – for composite components

Property type 11 was used to model the flat-plate and impact attenuator. As was the case with property type 1, fully integrated Batoz elements were used, hence there was no need to enter values for hourglass and damping coefficients. Number of layers and their respective thickness were entered as per the model. Separate duplicates with different thicknesses were created for the mesoscale model of the impact attenuator. Table **3.10** presents the parameters entered and their respective values.

Table 3.10: *Property type 11 (composites) parameters and inputs*

Flag	**Definition**	**Determination**	**Input Value**
I_{shell}	4 node shell element formulation flag	Refer to Table **3.9**	12
I_{smstr}	Shell small strain formulation flag	Refer to Table **3.9**	2
I_{sh3n}	3 node shell element formulation flag	1 – standard triangle 2 – standard triangle (large rotations possible)	2 (flag activated due to presence of triangular elements in the impact attenuator)
N	Number of layers (1 integration point through-thickness)	Number of layers	Flat plate (Macroscale): 4 plies each 0.64 mm thick [0 90 90 0] Impact attenuator (Macroscale): 2 plies each 0.75 mm thick [0 90], 3 plies each 0.75 mm thick [0 90 0], 4 plies each 0.77 mm thick [0 90 90 0] (Top, middle, bottom section)

			Both mesoscale models: 1 ply 0.64, 0.75 and 0.77 mm thick depending on the model [0]
I_{strain}	Compute strains for post-processing flag	Refer to Table **3.9**	1
$Thick$	Thickness	Based on the model	Flat plate: 2.56 mm Impact attenuator: 0.75 mm (top and middle sections), 0.77 (bottom section
I_{thick}	Resultant stress formulation flag	Refer to Table **3.9**	1
I_{plas}	Plane stress plasticity flag	Refer to Table **3.9**	2
I_{orth}	Orthotropic system formulation flag	0 – orthotropic system is with respect to local ply coordinate system 1 – orthotropic system is with respect to global coordinate system	0 (to ensure orthotropic directions are always maintained)

3.5. Contact modelling

This section goes over the three contact models used for this study: type 7 (node-to-element), type 19 (node-to-element and edge-to-edge) and type 24 (surface-to-surface). Table **3.11** lists the respective contact types used to define the interface amongst various components within the models. Type 19 and Type 24 contacts were introduced as type 7 contact models led to numerical penetrations in the trigger region when cohesive elements were added to the models. These prevented the edges of the plies in the trigger region to "see" and "repel" each other and the anti-buckling columns in a manner that is physical. Hence, a Type 19 contact was used at it combines a type 7 contact with an edge-to-edge contact (type 11). A type 24 contact is a surface-to-surface (element-to-element) contact that is also used to model sliding surfaces, such as the one between the anti-buckling columns and the composite specimen. The following sections explain each of these contacts in detail, the specific parameters that were activated and deactivated and their respective values. They also present the underlying kinematics behind the stiffness calculations. A study was conducted using the flat-plate model to obtain the best combination of stiffness formulations that accurately represent the progressive crush behavior and is discussed in section 5.5.

Table 3.11: Contact types used for the models

		Master Surface	Slave Surface	Contact Type
Macroscale	**Flat-Plate Model**	Impactor	Top Plate	Type 7
		Top Plate	Composite Specimen	Type 7
		Bottom Plate	Composite Specimen	Type 7
		Anti-Buckling Columns	Composite Specimen	Type 24
		Composite Specimen	Composite Specimen	Type 7
	Impact Attenuator Model	Top Plate	Impact Attenuator	Type 7
		Bottom Plate	Impact Attenuator	Type 7
		Impact Attenuator	Impact Attenuator	Type 7
Mesoscale	**Flat-Plate Model**	Top Plate	Composite Specimen	Type 7
		Bottom Plate	Composite Specimen	Type 7
		Anti-Buckling Columns	Composite Specimen	Type 19
		Composite Specimen	Composite Specimen	Type 19
	Impact Attenuator Model	Top Plate	Impact Attenuator	Type 7
		Bottom Plate	Impact Attenuator	Type 7
		Impact Attenuator	Impact Attenuator	Type 24

3.5.1. Type 7 (node-to-element)

Type 7 contact is a multiuse contact model available in Radioss that can be used to model interactions between nodes and elements/surfaces, wherein the master segment is composed of the elements of the master component and the slave segment is composed of nodes of the slave component as shown in Figure **3.21**a. Slave nodes behave according to the forces or the behavior of the master elements. This contact was also used to model the self-contact for the composite flat plate and the impact attenuator. A self-contact, shown in Figure **3.21**b, ensures that the elements and nodes within a component "see" each other and interact with one another, which is essential during a highly dynamic case such as the one under investigation in this work. In a self-contact, the nodes and elements on the same component are used as slave and master segments, respectively.

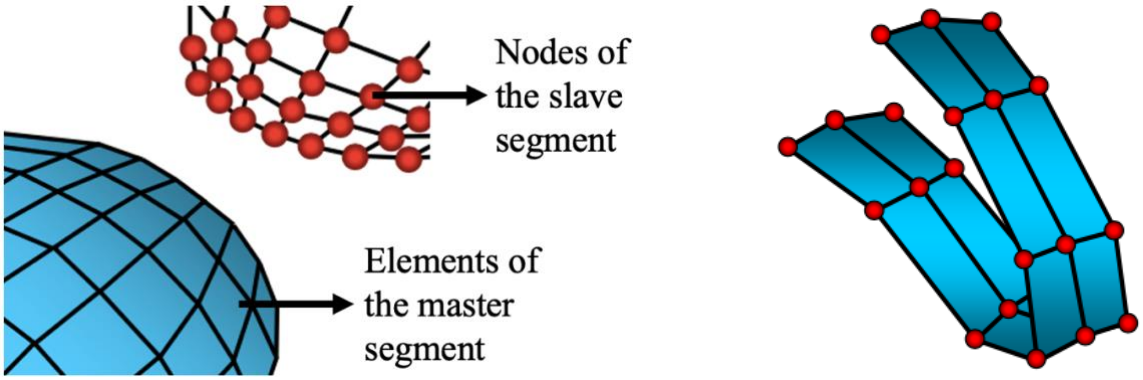

Figure 3.21: *Illustration of slave nodes and master elements in a type 7 contact (a); Self-contact with slave nodes and masterelements on the same component (b) (113)*

Stiffness between the slave nodes and master elements is calculated using equation 3.14, where minimum (St_{min}) and maximum (St_{max}) stiffness values are entered directly into the contact card and K_0 is calculated depending on the input for the I_{stf} flag as shown in equations 3.15 – 3.20. K_m is the stiffness dependent on the master component, K_s is the stiffness dependent on the slave component, E is the respective Young's modulus, t_m is the thickness of the master component and t_s is the thickness of the slave component. No maximum stiffness value was set, but a minimum stiffness of 1 kN/mm was set in order to avoid a "too soft" contact that could have occurred during the simulation run. Based on the recommendation of the reference manual, I_{stf} was set equal to 4 (113) (102). However, an investigation was conducted by trying different combinations of I_{stf} for interfaces that were set equal to either 1 or 4, to determine a combination that resulted in progressive crushing similar to that observed in physical experimental tests conducted on the flat composite plate. The same is described in detail in section 5.5. $Inacti$ parameter needed to be activated because the bottommost cohesive elements for the impact attenuator were modelled as 0.75 mm thick even though the thickness of the plies in reality was 0.77 mm, in order to maintain continuity between the plies in the middle and bottom section with coinciding nodes at the interface. Expectedly, modelling the cohesive elements as 0.75 mm thick led to initial penetrations that needed to be accounted for in the model and were done so by artificially shifting the bottommost plied by 0.02 mm thereby ensuring that the flat activation brought the model back to its original state of 0.77 mm thick cohesive elements in the lowermost section, albeit numerically. Section 6.1 further discusses this numerical modification. Friction coefficients were obtained from published literature studies (114) (115) (116). Although the friction coefficient varies during the crush process as the texture of the composite surface becomes coarser due to fiber and matrix damage, the contact models did not allow for this increase to be modelled (88) (114) (117). Additionally, it varies with a change in the number of cycles, velocity and load (115) (118) (119). Hence, nominal values were used for the friction coefficients of the standard Coulomb friction model, which was preferred over other friction models due to the availability of published data regarding the friction coefficients and it's used in other published studies that involved crushing of composite components (27) (120). Additionally, the friction coefficient between the anti-buckling columns and the composite plate would be affected by the force exerted during clamping, which would in-turn depend

on the user and their expertise in handling the fixture and ensuring that columns merely "kiss" the plate only to support it and not exert any force on it. Any force exerted would increase the friction coefficient and affect the specific energy absorption properties (41). For the numerical analysis, an idealized case was assumed, wherein the columns do not exert force onto the plate prior to impact and post-impact the force is exerted as a result of vibrations caused due to the impact and the interaction of the resulting fronds with the columns. Table **3.12** lists the input parameters for all the type 7 contacts.

$$K = \max\left[St_{min}, min(St_{max}, K_0)\right] \quad 3.14$$

$$K_0 = Stfac \text{ if } I_{stf} = 1 \quad 3.15$$

$$K_0 = \frac{K_m + K_s}{2} \text{ if } I_{stf} = 2 \quad 3.16$$

$$K_0 = max(K_m, K_s) \text{ if } I_{stf} = 3 \quad 3.17$$

$$K_0 = min(K_m, K_s) \text{ if } I_{stf} = 4 \quad 3.18$$

$$K_0 = \frac{K_m * K_s}{K_m + K_s} \text{ if } I_{stf} = 5 \quad 3.19$$

$$K_0 = K_m \text{if } I_{stf} = 1000 \quad 3.20$$

$$K_m = Stfac * 0.5 * E * t_m \quad 3.21$$

$$K_s = 0.5 * E * t_s \quad 3.22$$

Table 3.12: *Input parameters, their determination and input values for type 7 contacts*

Flag	Definition	Determination	Input Value
I_{stf}	Interface stiffness definition flag	Explained above	1 or 4
I_{gap}	Gap option flag	1 – variable gap according to the characteristics of the master and slave surfaces 2 – option 1 + gap scale correction of the computed gap 3 – option 2 + mesh size taken into account	3 (most robust option to accurately determine gap between master and slave segments during a dynamic crush event)
St_{min}	Minimum stiffness	Reference manual (102) (113)	1 kN/mm

$Stfac$	Stiffness scale factor		0 or 1 depending on the case in section 5.5
$Fric$	Coulomb friction	Obtained from literature (114) (115) (116) (121) and in the same range of values used in other literature studies involving crushing of composite components (27) (120)	0.3 between steel and CFRP 0.2 between CFRP (self-contact)
Gap_{min}	Minimum gap for stiffness activation	Required to avoid penetrations	0.5 mm (Half the thickness of the anti-buckling columns – thinnest component)
$Inacti$	Deactivation flag of stiffness in case of initial penetrations	1 – deactivation of stiffness on nodes 2 – deactivation of stiffness on elements 3 – change node coordinates to avoid initial penetrations 5, 6 – gap is variable with time and initial gap is adjusted to avoid initial penetration	6 (adjustment for initial penetrations is more real as compared to that for 5 and does not lead to deactivation of stiffnesses or variation of node coordinates (change in geometry))
I_{fric}	Friction formulation flag	0 – static Coulomb friction law 1 – generalized viscous friction law 2 – Darmstad friction law 3 – Renard friction law	0 (most widely used friction law so data available in literature and does not require too many parameters to be defined like the other laws)
I_{form}	Friction penalty formulation type	1 – viscous formulation 2 – stiffness formulation	2 (stiffness formulation appropriate for the type of problem)

3.5.2. Type 19 (node-to-element and edge-to-edge)

For some cases that involve edges crossing each other, such as the ones shown in Figure **3.22**, type 7 and 24 contacts do not capture edge-to-edge interactions accurately. Hence, an edge-to-edge (type 11) contact should be added. A type 19 contact combines a type 7 contact with a type 11 contact without any modifications to the type 7 contact parameters needed. It was activated for the mesoscale models of the flat composite plate as the edges of the separate plies in the trigger region did not interact as intended with each other and with the edges

of the anti-buckling columns with a type 7 contact. Figure **3.22** shows illustratively the effect of adding an edge-to-edge contact to the model.

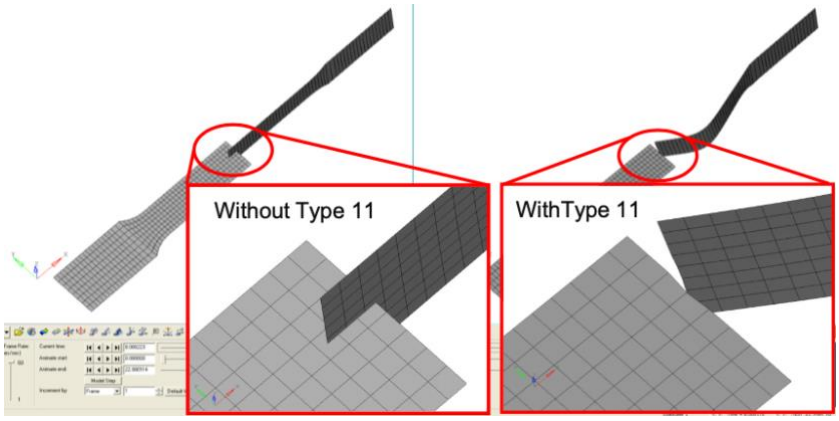

Figure 3.22: *Illustration of adding an edge-to-edge contact*

3.5.3. Type 24 (surface-to-surface)

In the case of sliding interface, a type 24 contact more accurately captures the sliding behavior as compared to a type 7 contact as a type 24 contact inculcates both the nodes and the elements for both the master and slave components as illustrated in Figure **3.23**. Hence, the interface between the anti-buckling columns and the flat composite specimen was modelled as a type 24 contact.

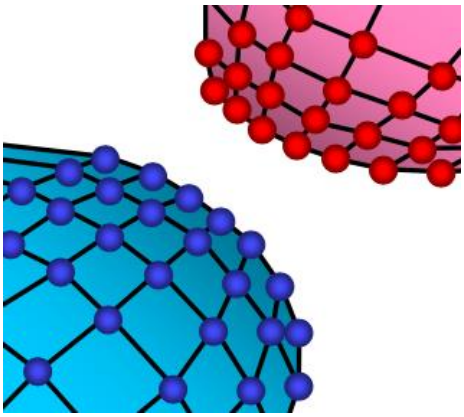

Figure 3.23: *Illustration of slave and master nodes and elements in a type 24 contact (113)*

In the case of the self-contact for the impact attenuator's mesoscale model, numerical penetrations were observed at the interface between the sections when type 7 contacts were used. Hence, these were changed to type 24 contacts, as the inclusion of elements for the slave segment and nodes for the master segment allows a greater part of the component to be in contact at the interface, especially given the complex geometry. Inputs to the parameters used for type 24 contacts were the same as those for type 7 contacts.

4. Fixture Design

The following chapter presents the simulation studies undertaken to support the design process of fixture. Evaluations were conducted to determine the thickness of the top plate with the objective of obtaining purely elastic deformations upon an 1850 J impact. A safety margin of 50 J was added to the 1800 J of maximum energy generation possible in the Instron CEAST 9400 Series Droptower Impact Systems, thereby resulting in an 1850 J impact for the simulations. After obtaining the desired top plate thickness, evaluation tests were undertaken to determine the optimum distance between the anti-buckling columns and their diameters with the objective that the specimen collapse resulted in progressive crush that initiated from the bottom of the specimen

without any damage on its top edge and any significant buckling. A 150 x 100 x 2.56 mm CFRP flat-plate composite specimen was used for all the simulations, due to the robustness of the material data available for the same as shown in section 3.3.3 and 3.3.4 (Table **3.3** – Table **3.8**). Additionally, CFRP is widely used to manufacture primary components in the automotive and aerospace industry as explained in sections 1 and 2 and was the material of choice for FCA. Published literature studies have reported the dependence of crushing behavior on the unsupported height of the anti-buckling columns and an investigation was conducted to determine the optimum height that allowed unimpeded frond formation (21) (41) (96). Finally, in order to assess the robustness of the fixture, the thickness of the CFRP flat plate specimen was increased hypothetically by adding 20 more plies and a test was conducted at the highest energy level of 1850 J to evaluate if the fixture is able to generate a progressive response for materials with mechanical properties other than ones that were used to aid its development. Discussed in the following sections are all of the above-mentioned investigations and a summary of the design parameters used to arrive at the final design shown in Figure **3.1**.

4.1. Identification of the thickness of the top plate

The initial design iteration specified the thickness of the top plate as 10 mm. Using the model shown in Figure **3.4**, material Law 2 and modelling the top plate as 10 mm thick, an 1850 J impact using a 145 kg impact mass and 5 m/s impact velocity resulted in plastic deformations around the point of impact and around the cavity machined in to allow the anti-buckling columns to pass through as shown in Figure **4.1**. Additionally, two elements were deleted as a result of the impact, which could either signify a significant dent at the point of impact or an amplification of the same due to the selected mesh size. In either case, plasticity in the top plate compromised the robustness of the fixture, hence the thickness was increased in increments of 5 mm to obtain a thickness that did not result in any plastic deformations. Slight plasticity was still observed at the point of impact with a 20 mm thick top plate, although none was observed around the cavities as shown in Figure **4.1**. A 25 mm thick top plate did not exhibit any plastic deformations. However, a margin of safety of 5 mm was added and an iteration was run with a 30 mm thick top plate to account for any plausible difference between the material properties of the physical plate and the numerical model, since the properties for the numerical model was obtained from the Total Materia database. As shown in Figure **4.1**, a 30 mm thick top plate did not exhibit any plastic deformation. The bottom plate was 15 mm thick and did not exhibit any plastic deformations as the composite specimen absorbed most of the energy.

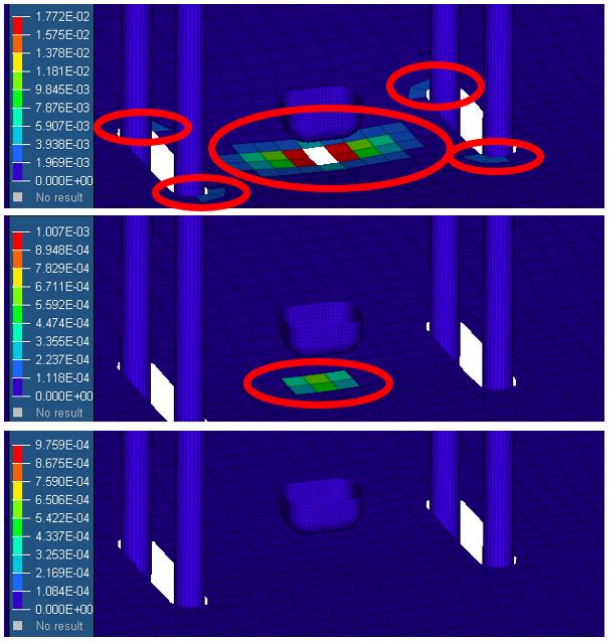

Figure 4.1: *Comparison of the deformation response of top plates with different thickness (10, 20 and 30 mm) to an 1850 J impact (48)*

4.2. Identification of the parameters relating to the anti-buckling columns

Following the determination of the top plate thickness, design studies were conducted at 550 J with an impact mass of 22 kg and an impact velocity of 7 m/s to determine the anti-buckling column spacing, diameter and unsupported height and assess their impact on the crushing behavior. An impact energy of 1850 J was not used as 850 J resulted in a >40 mm crushing displacement of the composite plate. Given that the maximum crush distance was 50 mm, 550 J was considered optimal in order to avoid damaging the fixture in initial trials. Subsequent studies, further explained in section 5.2, were conducted at 850 J after the operator gained confidence in the fixture. Mean crush force between 850 J and 550 J did not change significantly, with the extra energy bring displaced over a larger displacement. The impactor as seen in Figure **3.4** was removed and the velocity was directly applied to the rigid body element governing the top plate. The mass of the top plate was changed by artificially increasing the density of the steel material used in order to obtain the desired impact energy. The top plate thickness was unchanged as it was a factor in determining the contact stiffnesses as shown in equations 3.21 and 3.22.

4.2.1. Column spacing

Although specimen with width greater than 100 mm could be tested in the fixture, it was designed around with a 100 mm wide specimen in order to obtain coherence with the compression after impact standard (ASTM D7137) and with a goal to establish a standard to calibrate and determine numerical crashworthiness parameters that cannot be obtained from material characterization tests. Keeping a 100 mm wide specimen in mind, three values for the distance between each set of anti-buckling columns were tested: 50, 65 and 80 mm, and Figure **4.2** shows the front view of a time-lapse of the crushing behavior at 0, 2, 4, 6, 8 and 10 ms for all three configurations. The distance was measured from the axis of the columns and their diameter was set at 10

mm. As can be seen from the view at 2 ms, progressive crushing behavior was observable for all three configurations. Although it was not possible to accurately capture qualitatively the fronding behavior with the use of shell elements only (macroscale approach), some fronding is observable when the columns were spaced 65 mm apart as evidenced by each lower half of the trigger fronding to its respective side throughout the crushing process, whereas with the other two configurations the composite specimen only get crushed and undergo fragmentation. As the crushing behavior progressed, slight deformation of the tested composite plate was observed at the top for all three configurations (seen by a change in shade of the elements as they change angle with respect to the xy-plane), deformation that translated into permanent damage 8 – 10 mm deep from the top for the specimen supported by the columns spaced 80 mm apart. This permanent damage on the top of the plate for the configuration with supports 80 mm apart was probably because the specimen was not sufficiently supported from the middle (i.e., the free distance among the columns was too large) that resulted in buckling initially, later transforming into damage of the specimen as the top ended up as the weaker region due to stress concentration as compared to the bottom section. Alternatively, this damage may have been because the impact front did not travel to the bottom of the composite plate as quickly as it did for the other two configurations as evidenced by the onset of deformation on the top at the same time the composite plate got damaged from the bottom. Top edge deformations for the other two configurations occurred much later when most of the energy was already absorbed, resulting in only elastic deformations for the same. Early onset of deformation may have turned permanent as the impact period was spread over a longer duration. On the other hand, the specimen constrained by columns 50 mm apart exhibited multiple bucklings at the bottom of the specimen as seen from Figure **4.3**, which were probably caused due to overconstraining of the specimen in the middle that prevented it from crushing progressively. Hence, the intermediate spacing value, 65 mm, was selected as the final distance between the anti-buckling columns. In order to ensure that specimens made of materials with a lower Young's modulus than CFRP do not buckle from the middle, a provision was left in the fixture to add another set of shorter anti-buckling columns should the need be.

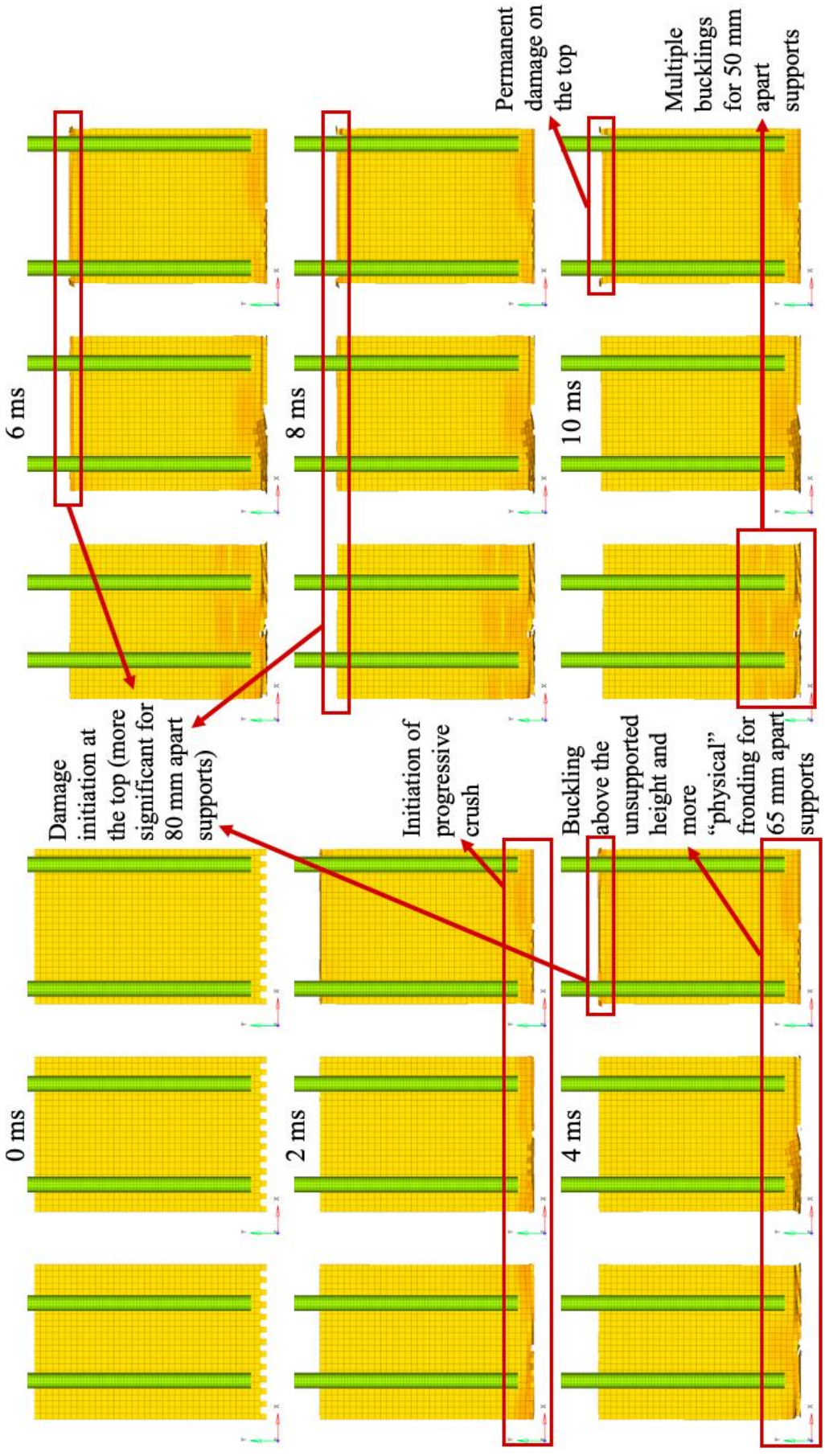

Figure 4.2: *Front view of a time lapse (0, 2, 4, 6, 8 and 10 ms) comparing the response of a 4-ply thick (2.56 mm) CFRP flat plate supported by anti-buckling columns spaced at three different distances (50 (left), 65 (center) and 80 (right) mm) to a 550 J impact*

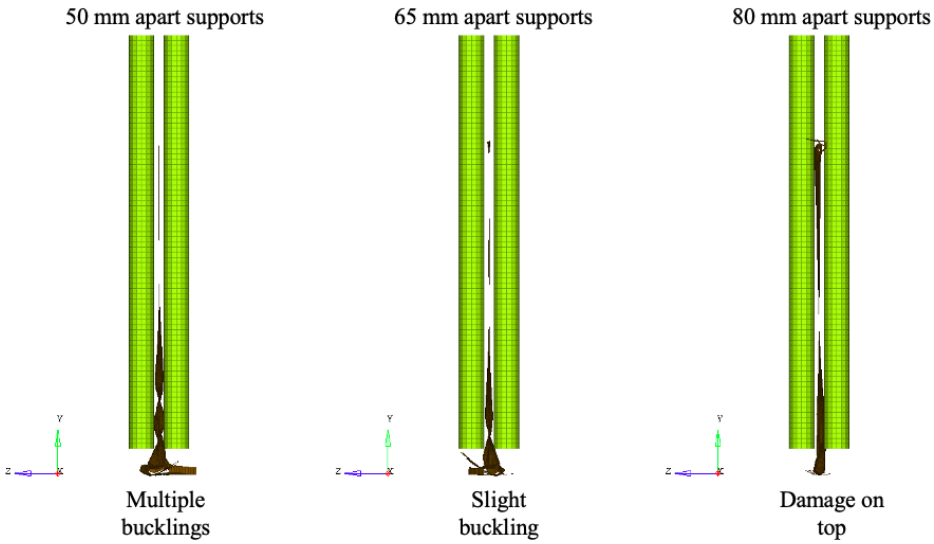

Figure 4.3: *Side view of a time lapse (0, 2, 4, 6, 8 and 10 ms) comparing the response of a 4-ply thick (2.56 mm) CFRP flat plate supported by anti-buckling columns spaced at three different distances (50 (left), 65 (center) and 80 (right) mm) to a 550 J impact*

4.2.2. Column diameter

Three diameters for the anti-buckling columns were evaluated with the columns placed 65 mm apart: 5, 10 and 20 mm. Similar to the case with the column spacing, progressive crushing behavior was initiated from the bottom of the plate, signifying proper functioning of the trigger mechanism, and was soon followed by slight deformation at the top of the specimen for all three configurations as shown in Figure **4.4**. However, the deformation was permanent only for the columns with the maximum diameter. The thicker columns could have impeded specimen fronding from the bottom, which caused permanent damage on the top. Fronding appeared to be more physical (i.e., similar to the experimental behavior) for the 10 mm column diameter configuration as compared to that observed under the 5 mm column diameter configurations, which also exhibited greater buckling as compared to the former possibly because of low lateral reinforcement provided by the latter. Hence, the column diameter was set at 10 mm for the final design. Additionally, columns with 10 mm diameters allow space for threaded screws to be inserted into them to attach them to the lateral support plates, which was not possible for the 5 mm diameter columns as they were too thin to add space for inserts and doing so would have resulted in a significant reduction of their strength and ability to counteract the vibrations introduced during a dynamic crushing test.

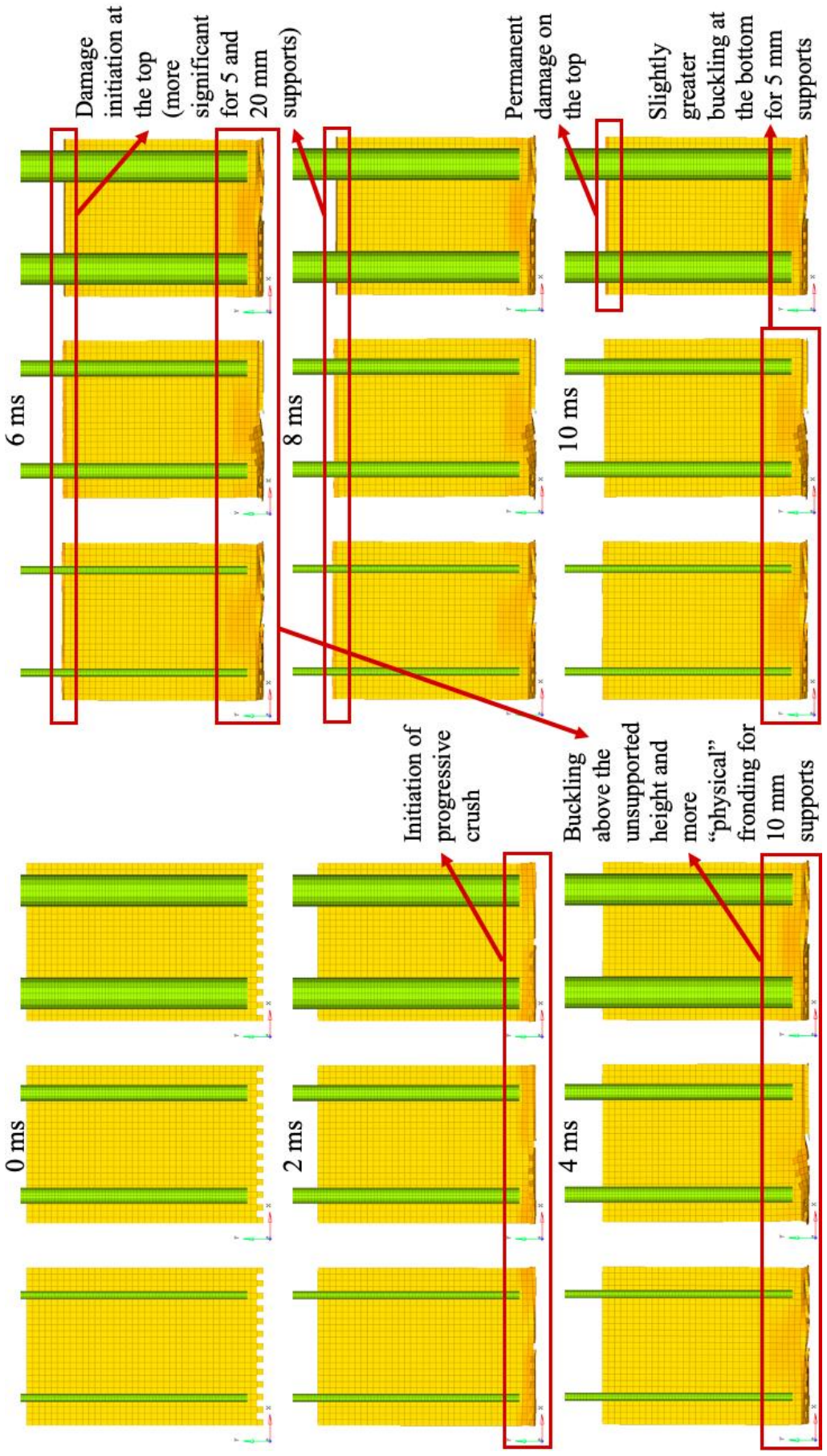

Figure 4.4: *Time lapse (0, 2, 4, 6, 8 and 10 ms) comparing the response of a 4-ply thick (2.56 mm) CFRP flat plate supported by anti-buckling columns of three different diameters (5 (left), 10 (center) and 20 (right) mm) to a 550 J impact*

4.2.3. Unsupported height

A provision was made in the fixture to change the height of the anti-buckling columns to modify the unsupported heights of the composite specimens being tested to evaluate the effect of the height on the crushing behavior. An investigation was undertaken to determine an unsupported height that would permit unimpeded frond formation yet provide enough lateral support to the composite specimen to not buckle and break upon impact. Four different heights were tested: 5, 10, 20 and 30 mm. The effect of the heights could be clearly seen from the force-displacement curves generated as shown in Figure **4.5**. A height of 5 mm resulted in a sudden increase in the force as a result of the interaction between the fronds and the anti-buckling columns that resulted in accumulation of debris in the crushing region. A height of 10 mm led to a stable crushing force. Heights of 20 and 30 mm caused the specimen to buckle leading to a drop in the force and a sustained low force as a result of breakage of the specimen. Hence, an unsupported height of 10 mm was suggested for the experimental investigation. An experimental investigation conducted on GFRP specimens after the fixture was manufactured and assembled revealed that a 10 mm height provided an appropriate gap to allow fronds to grow without impediment, whilst a lower height impeded frond formation and a greater height caused the specimen to buckle and break above the trigger region rendering the test invalid (95). Hence, the conclusions of this numerical investigation were validated through experiments, in that a 10 mm unsupported height offered sufficient gap for frond progression and lateral support for the composite specimens. Table **4.1** lists the final parameters for the fixture design.

Table 4.1: *List of final parameters for the fixture design*

Parameter	**Value**
Top plate thickness	30 mm
Column spacing	65 mm
Column diameter	10 mm
Unsupported height	10 mm

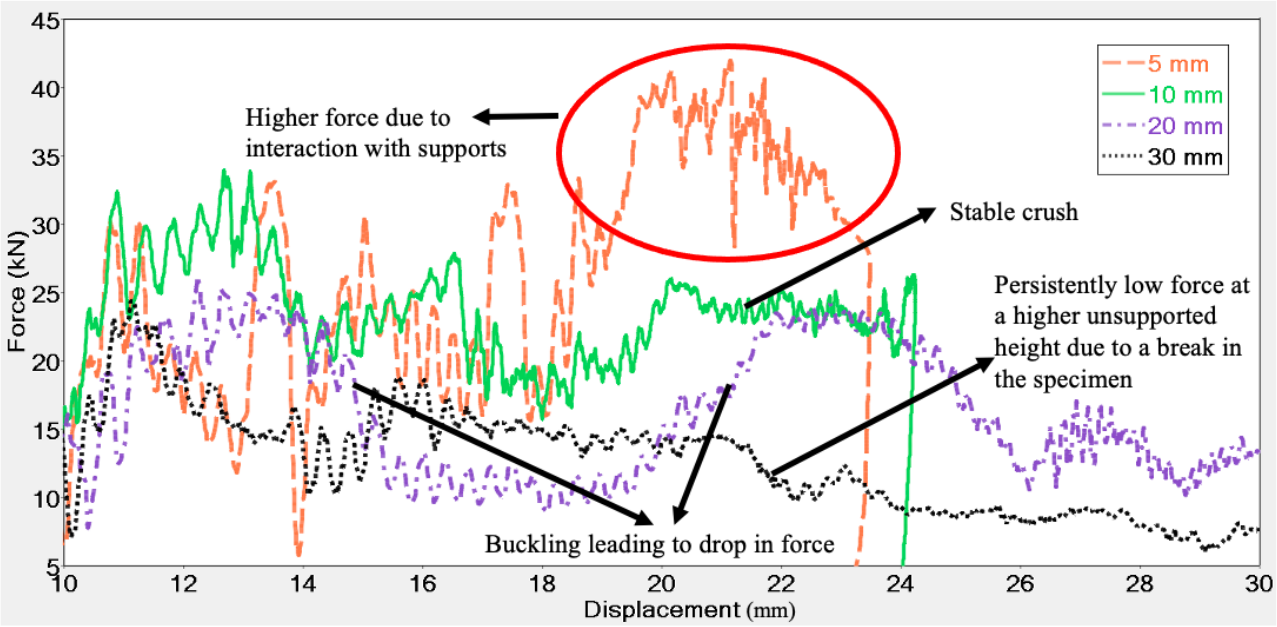

Figure 4.5: *Force-displacement curve comparison of a 4-ply thick (2.56 mm) CFRP flat plate impacted at 550 J supported by anti-buckling columns placed at different unsupported heights (5, 10, 20 and 30 mm) (48)*

4.3. Assessment of the robustness of the fixture

In order to assess the robustness and versatility of the design of the fixture with the parameters listed in Table **4.1** in generating a progressive crush behavior for materials with mechanical properties other than the ones used to aid its design and specimens with greater thicknesses, a hypothetical study was conducted by adding 20 more plies to the CFRP composite used resulting in a 150 x 100 mm composite specimen with 24 plies (15.36 mm thickness). It was impacted with 1850 J of energy with a 145 kg impact mass and 5 m/s impact velocity. As can be seen from Figure **4.6**, failure initiated from the bottom with fronding and fragmentation behaviors. The 24-ply thick specimen absorbed all 1850 J of energy within 15 mm of displacement, significantly less than the 50 mm it took to absorb the 550 J impact with 4 plies as expected. Since an approximately 16 mm thick CFRP specimen underwent only 15 mm displacement upon an 1850 J impact, laminates as thick as 16 mm, the maximum allowable thickness for the fixture, with energy absorption capabilities less than CFRP (such as GFRP) could be tested to obtain a mean crush force over a prolonged displacement. Specimens with such a material would undergo displacement greater than 15 mm, sufficient to obtain a stable crush region, and possibly less than 50 mm, the maximum allowable displacement, thereby preventing any damage to the fixture. Additionally, progressive damage behavior could be observed for specimens with these types of materials for longer than 5 ms, allowing the user sufficient data to assess the crashworthiness of the material. The assessment justified that the proposed design could enable dynamic testing of composite materials across a variety of material properties and thickness and was used to manufacture the fixture shown in Figure **3.1**.

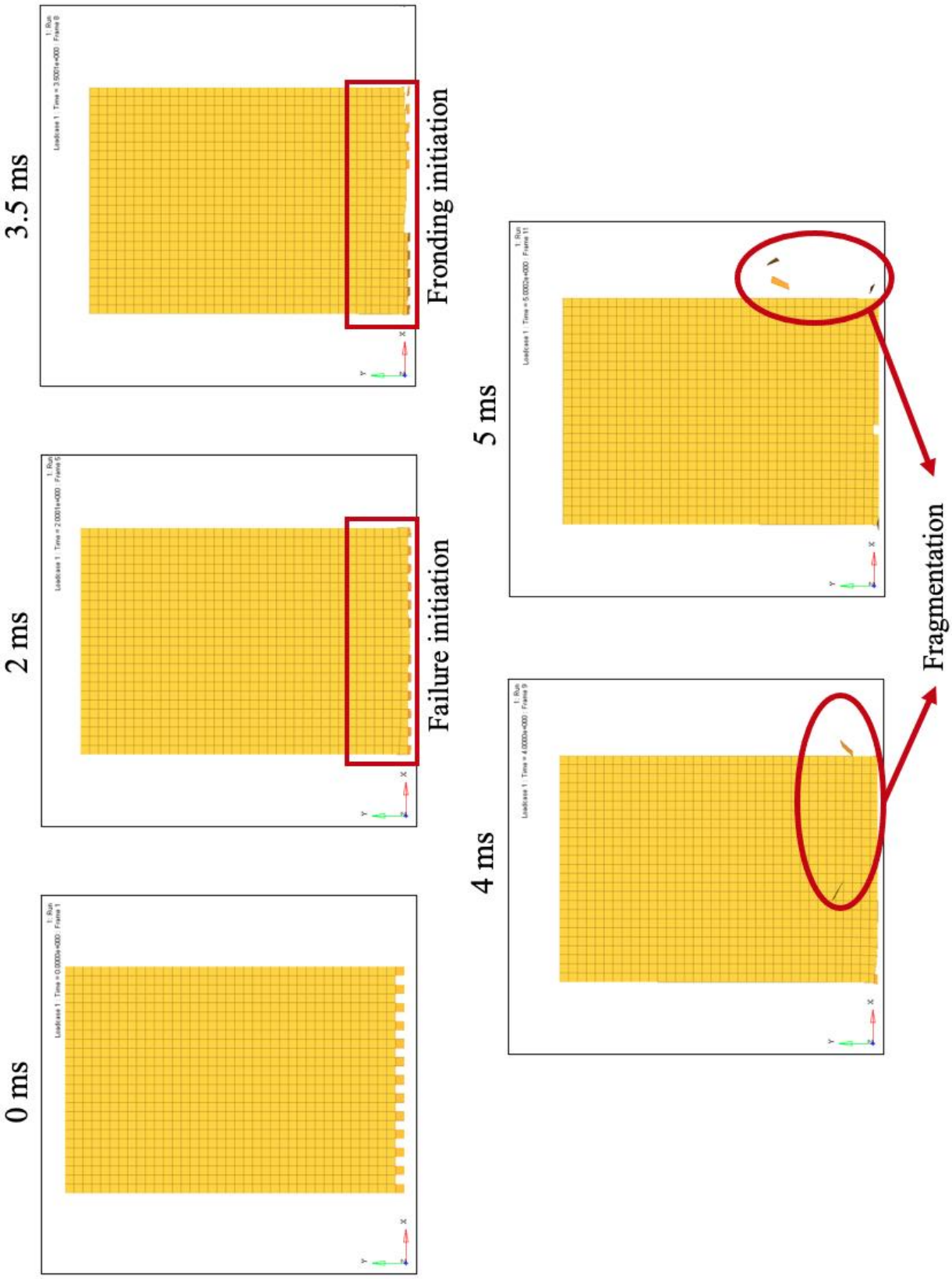

Figure 4.6: *Time lapse (0, 2, 3.5, 4 and 5 ms) comparing the response of a 24-ply thick (15.36 mm) CFRP flat plate to an 1850 J impact from the front (left) and side (right) views*

5. Material Card Calibration

This chapter presents the part of the methodology that relates to calibration of certain numerical parameters that are a part of the mathematical model that characterizes the numerical material structural behavior. These parameters could not be derived directly from experimental tests and improve the description of the crashworthiness of the material. It also details the studies conducted to arrive at the response function and optimization algorithm used for the penultimate calibration. Post determination of the function and the algorithm, studies were conducted to arrive at the tensile formulation and best combination of contact stiffness formulations that eliminate numerical (artificial) buckling and enable the composite components to undergo progressive deformations similar to those observed in experiments. Calibrations were conducted using optimization algorithms in HyperStudy. In the past, tuning of these parameters was typically undertaken using a trial-and-error approach, which is often time-consuming and does not guarantee that the values obtained are the optima. Calibrations performed using the adopted automated methodology are significantly more efficient and correlate the entire experimental and numerical force-displacement curves allowing for all the crashworthiness parameters to be taken into account when obtaining values for these numerical terms. Use of optimization algorithms and methodology also enabled sensitivity studies to determine the correlations between different parameters. Although detailed sensitivity studies were not conducted in this thesis, the methodology could be used for such studies as was done in those conducted by Wade, Feraboli and Boria (21) (23) (24). The ability to test composite plates that were significantly bigger than characterization coupons and exhibited failure modes similar to those observed for composite components and in full-scale testing presented an opportunity to extract crashworthiness force-displacement data that was unaffected by geometry and represented only the material's behavior. Calibrating numerical parameters using the entirety of these curves makes the model more robust and increases its predictive ability.

In the CRASURV formulation in material law 25 there are eleven numerical parameters that primarily govern the softening and element deletion behavior that should be calibrated to obtain good correlation between numerical and experimental results. These are:

- maximum global energy absorbed per unit volume (W_p^{max})
- energy absorbed during tension in 1 direction per unit volume ($W_p^{max^{t1}}$)
- energy absorbed during tension in 2 direction per unit volume ($W_p^{max^{t2}}$)
- energy absorbed during compression in 1 direction per unit volume ($W_p^{max^{c1}}$)
- energy absorbed during compression in 2 direction per unit volume ($W_p^{max^{c2}}$)
- energy absorbed during shear in 12 direction per unit volume (W_{12p}^{max})
- residual tensile stress in 1 direction (σ_{rs}^{t1})
- residual tensile stress in 2 direction (σ_{rs}^{t2})
- residual compressive stress in 1 direction (σ_{rs}^{c1})
- residual compressive stress in 2 direction (σ_{rs}^{c2})

- residual shear stress in 12 direction (σ_{12rs})

Due to the quasi-isotropic nature of the CFRP material used, properties in 1 and 2 directions were assumed equal. Since tension behavior does not have a huge bearing on the impact behavior, tension softening was modelled as linearly downward sloping until the maximum tensile strain. Hence, residual tensile stress values were not included into the parameter calibration activity. Tensile failure was strain based; hence tensile energy absorption parameter was not required to be defined. Additionally, the global energy absorption parameter is encompassing of all the other energy absorption parameters, hence only W_p^{max} was defined. These assumptions and modelling decisions finally resulted in only four parameters that needed to be calibrated using the optimization techniques (W_p^{max}, σ_{rs}^{c1}, σ_{rs}^{c2} and σ_{12rs}) of which the compressive residual stresses in 1 and 2 directions were, reasonably, considered equal. The following sections discuss the calibration setup and the optimization algorithms and response objectives used before presenting the correlation obtained between the numerical and experimental results.

5.1. Overview of the calibration setup

Following were the steps undertaken as a part of the setup process:

- Input variables and their bounds: The four above-mentioned parameters were entered as the input variables. Upper bounds for the residual stresses were fixed as the respective ultimate stresses as residual stresses cannot exceed the ultimate stress. Lower bounds for the residual stresses were fixed as 10% of the upper bound to allow a greater range of values. Lower bound for the maximum global energy absorption parameter was fixed as 0.008 J/mm^3 as that was the area under the shear stress-strain curve. The upper bound for the same was fixed at 0.12 J/mm^3 for the macroscale model based on values obtained from literature (120). For the mesoscale model, the optimization arrived at the previously set upper bound for W_p^{max} as the value that achieved lowest response value, hence the upper bound was increased sequentially to 0.6 J/mm^3 in order to avoid this behavior. Nominal values were set arbitrarily within the bounds for all the variables in order to initiate the next step. It was ensured that the function that determined the value for the input variables for the iterations, was continuous and not discrete to allow for more precision in the value for the variables. The precision was set to six decimal places.
- System check: After defining the input variables and their bounds a system check was conducted to ensure that the simulations run on both the upper and lower bound. A system bounds check was preferred over the nominal check as it allows for the simulation to be run on both the bounds and also on the nominal values, whereas a nominal check runs simulation only on the nominal values.
- Response objective definition: A preliminary study was conducted between two response functions to arrive at the one that resulted in a closer correlation with the experimental force-displacement curve. The representative experimental curve used was of a 550 J impact at 7 m/s. The response objectives were set to minimize the response values, i.e., the differences between the two force history curves. The two considered response functions were: summation of the absolute difference between the experimental and

simulation crush force as shown in equation 5.1 and summation of the squared difference between the experimental and simulation crush force as shown in equation 5.2. The sampling frequency of the experimental data was 1 MHz that resulted in 10,000 data points over 10 ms, which was the typical run time for a 550 J impact. The sampling frequency for the numerical simulations was set equal to that of the experiments. The results of the investigation are shown in section 5.2. The response object was run at the nominal value to obtain a nominal objective function value (NOFV) that was used as an input to determine the convergence criteria for the optimizations. Average deviation from the experimental mean force (ADMF) value could be gauged by equations 5.3 and 5.4, and was used to measure to compare the accuracy of different approaches and techniques.

$$ResponseObjective_{abs} = minimize\left[\sum_{t=0}^{\infty}\left(\left|F_{exp} - F_{sim}\right|\right)\right] \quad 5.1$$

$$ResponseObjective_{sq} = minimize\left[\sum_{t=0}^{\infty}\left(F_{exp} - F_{sim}\right)^2\right] \quad 5.2$$

$$ADMF_{abs} = \frac{ResponseObjective_{abs}}{Experimental\ mean\ force\ \times Run\ time\ \times\ Sampling\ frequency} \quad 5.3$$

$$ADMF_{sq} = \frac{\sqrt{\frac{ResponseObjective_{sq}}{Run\ time \times Sampling\ frequency}}}{Experimental\ mean\ force} \quad 5.4$$

- Optimization algorithm selection: Given the nature of the problem: deterministic with a single objective, multiple variables and constrains, only the following optimization algorithms could be used from those available in HyperStudy:
  - Adaptive response surface methodology (ARSM): The response surface methodology (RSM) was first introduced by Box and Wilson in 1951 to obtain an optimal response of a response variable to various exploratory variables using a design of experiments approach and a second-degree polynomial model (122). Relations between these variables are modelled using a mathematical model that can be seen effectively as a (multidimensional) response surface. Models that involve building these response surfaces based on simulations are called *surrogates*. Once a (surrogate) RSM has been identified, one can arrive at the objective optimum with relative ease with inexpensive simulations; however, to get a suitable RSM a number of expensive simulations have to be run. It is therefore convenient to minimize the number of simulations to reduce the computation cost of the optimization, whilst ensuring that the actual system improves throughout each step of the search. ARSM involves surrogates that boast of a better management of the approximation model in the optimization process to ensure a design optimum for the actual problem, hence making them more efficient as compared to generic RSM techniques (123). Various ARSM techniques have been developed over the years and have been validated using

a full-scale automotive crashworthiness and aircraft stiffened panel example (123) (124) (125). The ARSM technique available in HyperMesh builds the first response surface using a linear regression polynomial and then validates the optimum of this forecasted surface with the simulation that was run with the assigned variable values. If the output response value from the surface is not within the convergence criteria defined for the exact simulation, the surface is updated with the new evaluation and the process is repeated until the convergence criteria is met (126). The convergence criteria are based on either of the five criteria: absolute convergence (if reached for two consecutive designs (equation 5.5), relative convergence (equation 5.6), design variable convergence (equation 5.7), maximum number of iterations and failed analysis. If any of these criteria are reached, the optimization process is terminated. The convergence criteria, shown in

- Table **5.1**, was unchanged from its default values for all optimizations conducted with the ARSM technique.

$$|objective\ function_t - objective\ function_{t-1}| < convergence\ limit_{abs} * NOFV \quad 5.5$$

$$\frac{objective\ function_t - objective\ function_{t-1}}{objective\ function_{t-1}} \times 100 < convergence\ limit_{rel} \quad 5.6$$

$$\Delta\ input\ variable < \begin{cases} convergence\ limit_{design\ \ variable} \times range\ of\ the\ variable \\ convergence\ limit_{design\ variable} \times |nominal\ value| \end{cases} \quad 5.7$$

Table 5.1: *Convergence limits for ARSM technique*

Convergence Criteria	Value
$Convergence\ limit_{abs}$	0.001
$Convergence\ limit_{rel}$	1 %
$Convergence\ limit_{design\ \ variable}$	0.001

- Global response surface methodology (GRSM): This methodology was developed by Altair Engineering Inc. and since it is their proprietary method, not much published literature is available for the same. It is an improved form of the ARSM, in that it has global optimization capabilities as compared to local optimization capability of ARSM that ensure that it does not get stuck on a local optimum. It does this by simultaneously generating global and local response surfaces to ensure a good balance between the two search capabilities. These response surfaces are updated as the optimization progresses to obtain a better fit. This capability makes it less efficient as compared to ARSM, but significantly more robust and accurate (126).

- Sequential quadratic programming (SQP): This methodology is a gradient-based iterative optimization method, which is of the same level of accuracy and efficiency of GRSM. A major drawback of this technique, as implemented in HyperStudy, is that it operates with unconstrained input variables, which might result in optima with unrealistic input values (126). For the purposes of this study, this could mean residual stress values higher than the ultimate stress, which would physically not be possible. Negative values for residual stresses and energy absorbed would also be tested with initially by the optimization model, but simulations with these values would terminate prematurely, thereby ensuring that the optimization model "learns" that negative values are not possible and stays in the positive quadrant. This drawback of this technique made it unsuitable for the purposes of this study.
- Method of feasible directions (MFD): This methodology involves moving from one feasible design to an improved feasible design, reducing the objective response function as a result (126). Like SQP, the unconstrained nature of the input variables made this technique unsuitable for the purposes of this study.
- Genetic Algorithm (GA): This methodology is a metaheuristic inspired by Charles Darwin's theory of natural evolution (127). It starts by creating a population of designs that are ranked according to their fitness, which is a measured as a function of the constraint violation and objective function values. The "fittest" designs are reproduced using crossovers and mutations and the resulting designs become part of the next generation of designs, which undergo the same ranking and mutation processes until convergence is reached (126). Like SQP, the unconstrained nature of the input variables made this technique unsuitable for the purposes of this study.

Table **5.2** summarizes the advantages and disadvantages of each of the above-mentioned optimization techniques and ranks them based on their accuracy and efficiency. SQP, MFD, and GA were not considered for this study due to unconstrained nature of the input variables that characterizes their implementation within HyperStudy. Section 5.3 details the results of the study conducted to compare the applicability of ARSM and GRSM. Figure **5.1** presents a flowchart of the optimization procedure described above using the GRSM technique.

Table 5.2: *Comparison of available algorithms according to their advantages, disadvantages, accuracy and efficiency (126)*

	Advantages	Disadvantages	Accuracy	Efficiency
ARSM	Highly efficient	Only single objective local optimization	*	***
GRSM	Highly accurate and robust as allows for single or multiple objective global optimizations	Not as efficient as ARSM	***	**
SQP	--	Not possible to enter constraints for input variables Only single objective local optimization	***	**
MFD	--	Not possible to enter constraints for input variables Only single objective local optimization	**	**
GA	--	Significantly expensive and to be used only if the simulations are affordable Only single objective local optimization	**	*

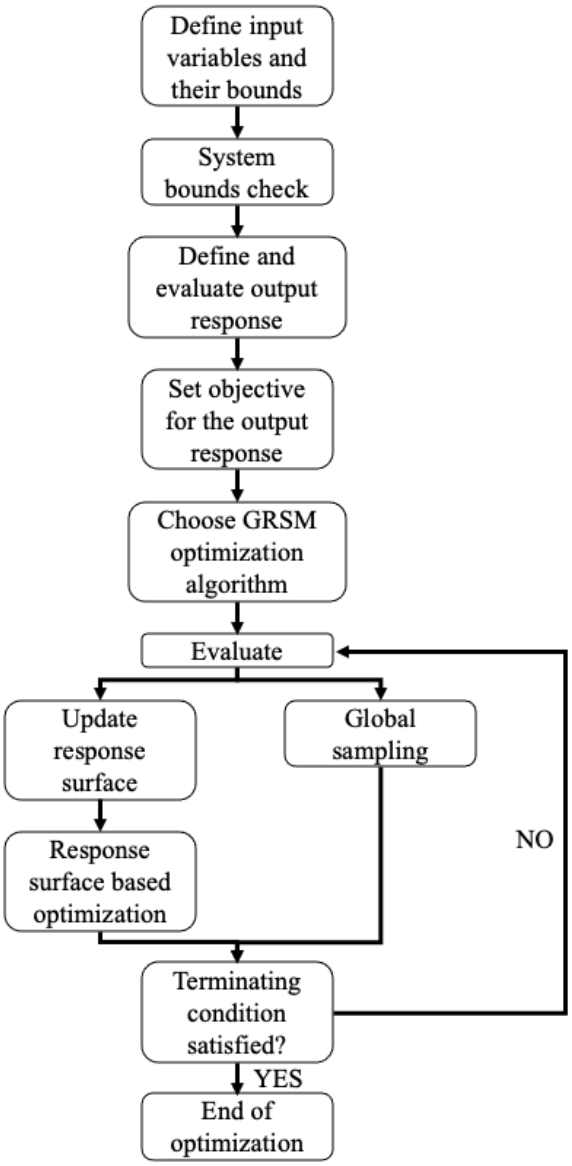

Figure 5.1: *Overview of the calibration approach with GRSM optimization algorithm*

5.2. Comparison of response objectives

Two response objectives stated in equations 5.1 and 5.2 were compared and Figure **5.2** presents the force-displacement comparison of the calibrated models for each response objective with the experimental results. The models were calibrated using the ARSM optimization algorithm. The tests were conducted at 850 J with an impact mass and velocity of 50 kg and 5.84 m/s respectively on 150 x 100 x 2.54 mm CFRP flat plates. Both the response objectives were able to initiate a progressive crush behavior as evidenced by a sustained mean crush force and the correlation for both the objectives improved after the trigger region as the trigger region was modelled with a geometry different to that in the physical composite plate as explained in section 3.2.1.2. Although results of both the objectives overlapped until 20 mm displacement, they diverged after that with the absolute difference approach showing a closer comparison with the experimental results as compared to the squared difference approach. This resulted in an error of 4.5% and 11% for the absolute and squared difference approaches respectively for the stroke displacement. As can be seen from

Table **5.3**, the ADMF value for the absolute difference approach was 22% lower than that for the squared difference approach, signifying that the former was able to model the crushing behavior more accurately. Response value was higher for the squared difference approach to the inherent mathematical formulation, hence could not be used as barometer to gauge the accuracy of the function in calibrating the material card, hence the ADMF value was used. The scatter for the residual stresses was minimal, hence suggesting that the energy absorption value was better calibrated using the absolute difference approach, which in turn lead to the improved correlation. Since the absolute difference approach showed better correlation with the mean crush force and lower error for stroke displacement, it was preferred over the squared difference approach for the subsequent calibrations.

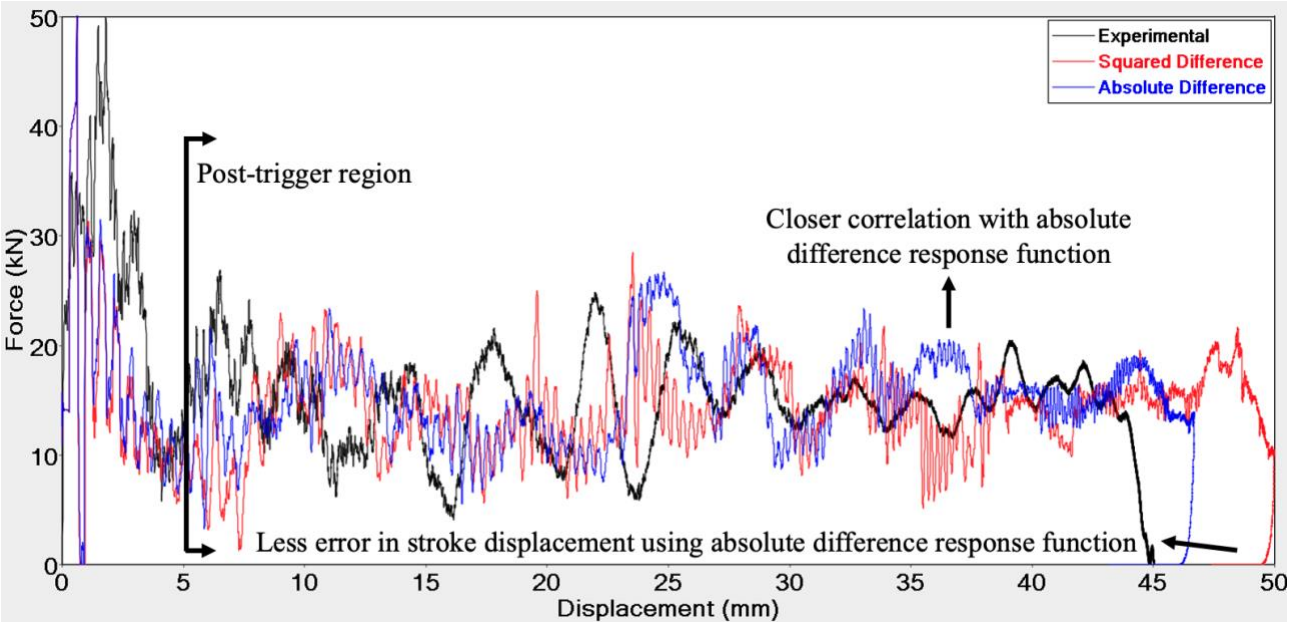

Figure 5.2: *Comparison of the experimental force-displacement curve with those obtained from optimized runs with the squared and absolute difference response objectives*

Table 5.3: *Comparison of post-optimization variable and response values*

Response objective	$W_p^{max}\ (J/mm^3)$	$\sigma_{rs}^{c1}, \sigma_{rs}^{c2}\ (MPa)$	$\sigma_{12rs}\ (MPa)$	Response objective value (kJ)	ADMF
Absolute difference	0.069440	94.900	20.57	60,989.55	0.407
Squared difference	0.053263	86.051	20.56	559,195.80	0.499

Figure **5.3** shows the comparison between the ADMF value progression for the absolute and squared difference response functions. Response values for these functions could not be compared because they were at least an order of magnitude higher for the squared difference function as compared to the absolute difference function

due to the inherent mathematics. Due to the use of the ARSM approach, the response values do not exhibit a clear convergence, especially for the squared difference approach, with the minimum values occurring at 10th and 13th iteration for the absolute and squared difference approaches, respectively. This was due to the inherent lack of progression and convergence of the response values of the ARSM approach that renders it as a randomized optimization algorithm as compared to the GRSM approach, which shows a clear progression and convergence as the optimization progresses, as is explained in the following section. Hence, any deductions from this graph remain inconclusive. Since the absolute difference approach showed better correlation with the mean crush force and lower error for stroke displacement, it was preferred over the squared difference approach for the subsequent calibrations.

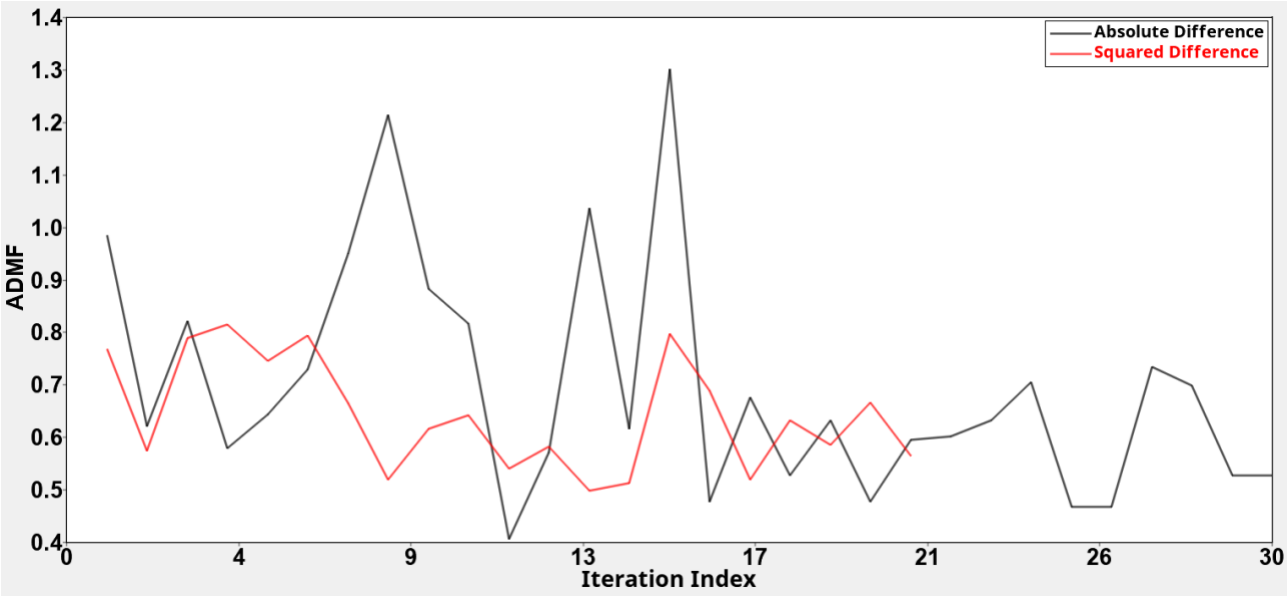

Figure 5.3: *Comparison of the ADMF values for all iterations of the optimization approach for the absolute and squared difference response functions*

5.3. Comparison of optimization algorithms

The ARSM and GRSM techniques were tested with the absolute difference response functions to compare their ability to simulate progressive crush behavior similar to that observed in experimental tests. Tests were conducted at 850 J using an impact mass and velocity of 50 kg and 5.84 m/s respectively on flat composite plates. As can be seen from Figure **5.4**, calibrated models obtained using both the techniques were able to simulate a progressive crush behavior similar to the experimental results and there was a difference of less than 1% in their error for stroke displacement. The ADMF values were 0.422 and 0.406 for the calibrated models obtained using the GRSM and ARSM approaches, respectively, suggesting that the ARSM algorithm was 4% more accurate primarily on account of the lower spread of the simulated force versus the experimental force after 42 mm of displacement. However, upon analyzing the response value progression with the optimization, the GRSM technique appeared more progressive as the response value decreased gradually, whilst the ARSM technique did not show any particularly progressive behavior as shown in Figure **5.5**. Additionally, the GRSM technique first reached the optimum value after 30 iterations, after which it ran several

iterations to obtain other optima due to the absence of any convergence criteria, but instead arrived at the same value repeatedly, albeit periodically, before terminating at 62 iterations, which was the maximum number of iterations inputted. ARSM technique on the other hand, converged after 29 iterations, significantly prior to the 62 iterations that were allowed to run. Therefore, both the techniques were equally efficient for the particular type of simulations used in this study, but GRSM would need user intervention to stop the analysis if the response value arrives at the optima repeatedly. Although both techniques showcased an equal magnitude of accuracy and efficiency for the analysis under consideration for the work in this study, the progressive nature of the GRSM approach led to the conclusion that it should be used for academic purposes, whilst ARSM could be used in the industry as it terminated immediately after arriving at the optima due to the presence of convergence criteria. Hence, GRSM was used for the remainder of the analysis. It was discovered that 40 – 50 iterations would be sufficient to reach the optima, hence the maximum number of iterations was fixed at 45 for the subsequent runs.

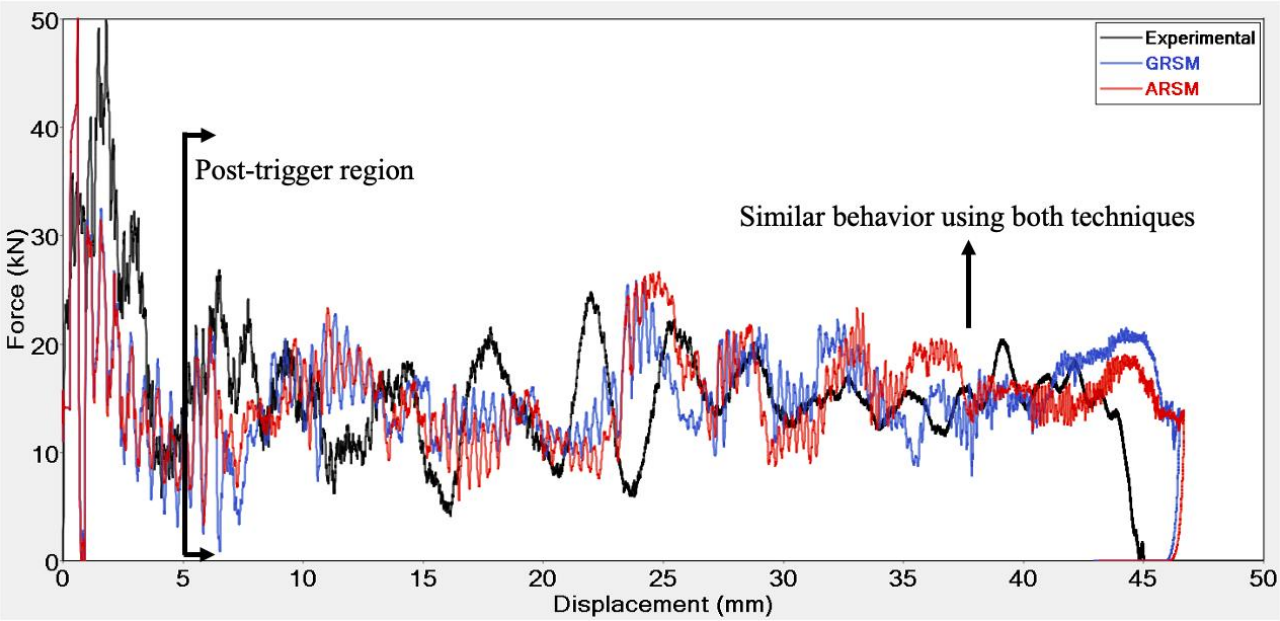

Figure 5.4: *Comparison of the experimental force-displacement curve with those obtained from optimized runs with the GRSM and ARSM algorithms*

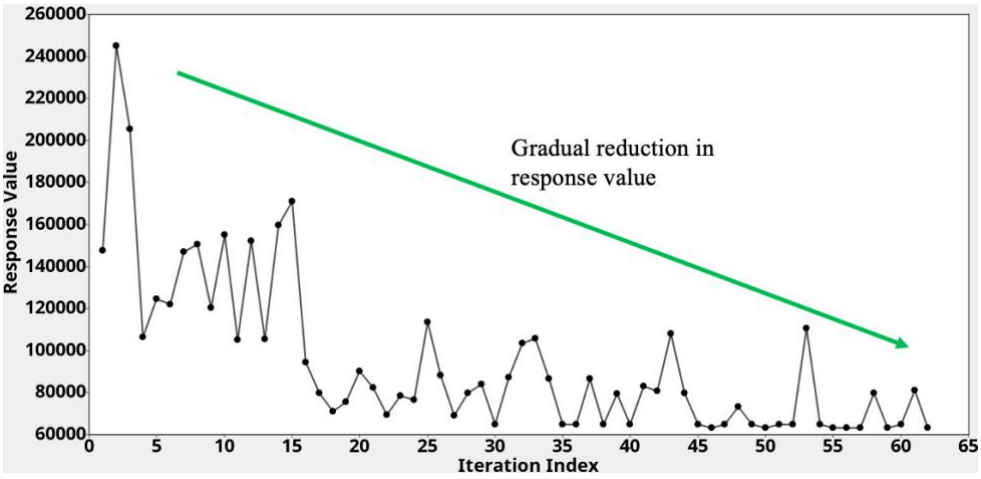

(a)

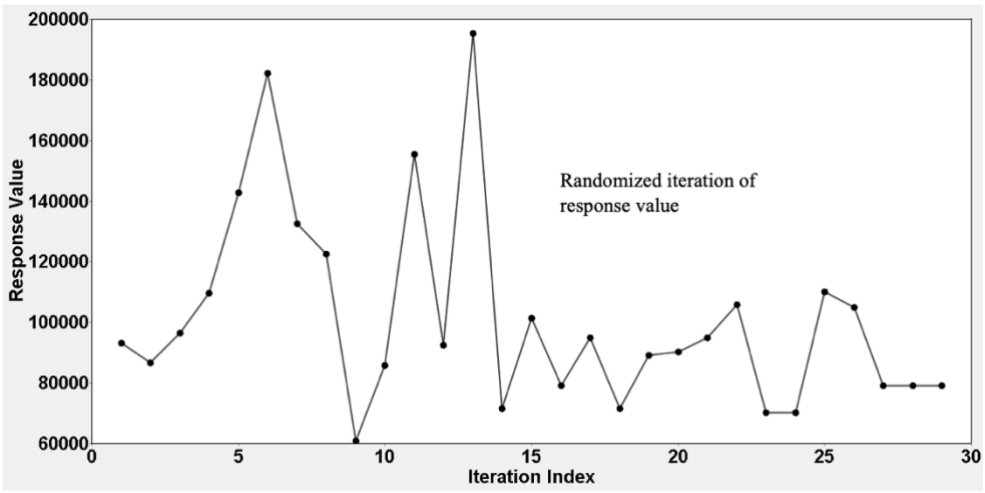

(b)

Figure 5.5: *Response values for different runs using GRSM (a) and ARSM (b) algorithms*

5.4. Determination of the tensile formulation for the composite material

A comparison of the two tensile formulations, elastoplastic and purely elastic, for characterizing the tensile behavior of the composite material as explained in section 3.3.3 was conducted using an impact energy of 550 J (7 m/s impact velocity and 22 kg impact mass) to determine its effect on the crashworthy behavior of the composite plate. The analysis was conducted using the GRSM and absolute difference approaches. As can be seen from Figure **5.6**, the model with the elastic formulation results in lower buckling above the unsupported height as compared to that observed using the elastoplastic formulation.

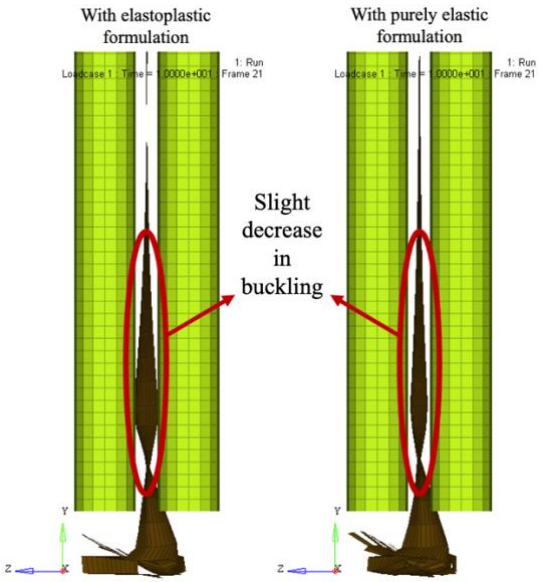

Figure 5.6: *Side-view comparison of final damage using the elastoplastic and purely elastic tensile formulation*

Experimental data used hereon forth was different from that used in sections 5.2 and 5.3, as a more stable crush (more akin to ideal crushing with initial peak at the level of mean crush force) was obtained in subsequent runs due to a slight modification in the experimental procedure that involved impacting the specimen using a hemispherical impactor. There was no change in the material used. Updating of the experimental set is not though to affect the findings of the previous sections, as they are dependent on the underlying mathematics behind the response functions and algorithms, which generally are unaffected by a slight change in the dataset as long as the dataset is of the same general type. Although this updated dataset would have changed the values for the optimized parameters, it would have done so "proportionally" for either of the parameters under consideration (the two response functions or the two optimization algorithms), thereby most likely not changing the findings of the studies conducted previously. Lower buckling could also be seen in the force-displacement graph in Figure **5.7**, as the sudden increase in the force due to buckling at 20 mm was lower for the elastic formulation as compared to the elastoplastic formulation. Additionally, this resulted in an error of 8% for the elastic formulation as compared to a 12% error for the elastoplastic formulation for the correlation between the experimental and numerical stroke displacements. Lower buckling for the elastic formulation was due to the absence of plastic deformations induced during vibrations of the plate, which in the case of an elastoplastic formulation become permanent damage and aggravate into buckling. ADMF values when composite tensile behavior was modelled as elastoplastic and purely elastic were 0.115 and 0.111, respectively, suggesting that the latter lead to better the correlation with the experimental results. Improved correlation with the experimental results and lower buckling, ceteris paribus, led to the conclusion that tensile behavior be modelled as purely elastic, thereby ignoring any reduction in the Young's modulus caused due to microscopic damage of individual fibers or tows or of the fiber-matrix interface. The residual buckling was attributable to contact modelling, which is further discussed in the next section.

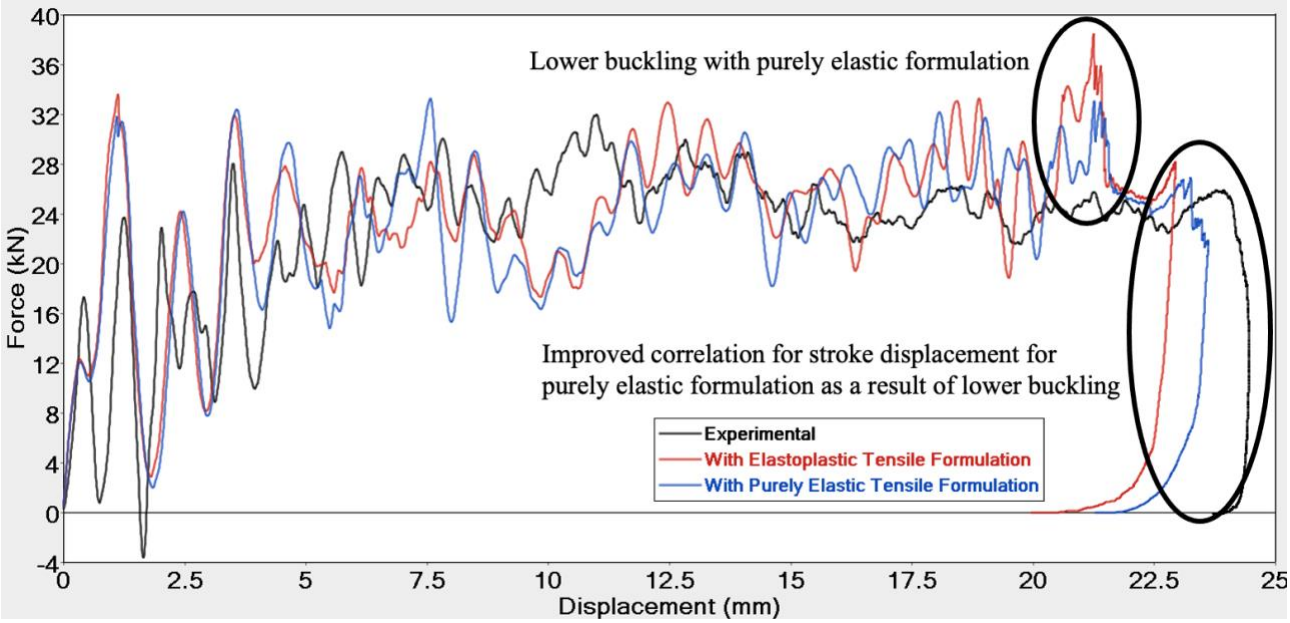

Figure 5.7: *Force-displacement comparison of the two tensile formulation*

5.5. Determination of the contact stiffness combination

Different combinations of stiffnesses activation flags and factors were tested to arrive at one that resulted in elimination of the residual buckling seen in Figure **5.6** and ensure that the qualitative and quantitative numerical results correlated with those obtained from experiments. Initially, stiffness between all the components was set equal to a minimum stiffness value 1 kN/mm that avoids a "too soft" contact. The value was obtained from the reference guides (128). This model was set as the benchmark. To do so, I_{stf} was set equal to 1, which ensured $K_0 = Stfac$. $Stfac$ was set to 0 to force the K value in equation 3.14 to equal the minimum stiffness value. A model with all stiffnesses between the components set to 1 kN/mm resulted in fronding at bottom of the specimen, damage on the top of the specimen and slight buckling that extended above the unsupported height. Seven different combinations, except from the benchmark, of stiffness were run as shown in Table **5.4**. Calculation of the stiffness between components was conducted by setting I_{stf} equal to 4, which was the recommended stiffness model, and $Stfac$ equal to 1. This ensured that the stiffness between the components for which the stiffness was to be calculated was computed using equation 3.18, 3.21 and 3.22. If the computed value was greater than 1 kN/mm, the same would be used and if it was lower than 1 kN/mm, the minimum stiffness value would be used. Activation of stiffness calculation between the composite plate and the anti-buckling supports did not have any effect on the results as evidenced by the no change in the deformation type between cases A and B, D and F and E and H as the contact was purely sliding and supportive in nature. However, activation of stiffness calculation between other components did have an effect on the final damage as shown in Table **5.4**.

Table 5.4: *Comparison of the different contact stiffness formulation combinations based on their respective damage behavior and an overview of the cases selcted to be optimized*

Case	Stiffness Formulation	Deformation Type	Optimization
A	Minimum stiffness for all contacts	Fronding at the bottom with buckling extending above the unsupported height and delamination on top	
B	Calculated stiffness between supports and specimen	Fronding at the bottom with buckling extending above the unsupported height and delamination on top	
C	Calculated stiffness between impactor, base and specimen	Fronding with significant buckling at the bottom extending above the unsupported height	
D	Calculated stiffness between elements of the specimen (self-contact)	Fronding at the bottom	
E	Calculated stiffness for all contacts	Fronding at the bottom	✔
F	Calculated stiffness between supports and specimen and elements of the specimen	Fronding at the bottom	✔
G	Calculated stiffness between impactor, base and specimen and supports and specimen	Fronding with significant buckling at the bottom extending above the unsupported height	✔
H	Calculated stiffness between impactor, base and specimen and elements of the specimen	Fronding at the bottom	

Cases D, E, F, and H eliminated any buckling and ensured the specimen was damaged progressively with fronding at the bottom and no damage on the top of the specimen, similar to what was observed in experimental tests. Since the results of cases D and H were the same as that of case F and E, respectively, and the latter cases were encompassing of their respective former ones, cases D and H were not considered for further investigation. Further investigation involved conducting optimization studies to ensure that the damage reported in Table **5.4** was applicable and observable also at the respective calibrated values. Although, case G exhibited slight buckling at the bottom above the unsupported height, it was possible that this was introduced due to the use of uncalibrated values. Hence, the combination listed under case G was also considered for parametric optimization.

The calibrated model for case E displayed multiple buckling along the entire length of the composite plate, as shown in Figure **5.8**, possibly because the contact became too stiff. However, cases F and G developed fronds only at the bottom. Frond formation for case F extended 30 mm above the unsupported height, whilst for case G it was restricted entirely below the unsupported height as shown in Figure **5.8**. Additionally, the ADMF values were 0.149 and 0.132 for cases F and G, respectively, suggesting that case G more accurately modelled the crushing behavior. Therefore, the contact stiffness calculation based on the Young's modulus and thickness of the respective components was activated between the metallic top plate and the composite specimen, the metallic bottom plate and the composite specimen and the metallic anti-buckling supports and the specimen, whilst minimum stiffness value of 1 kN/mm was used for the self-contact.

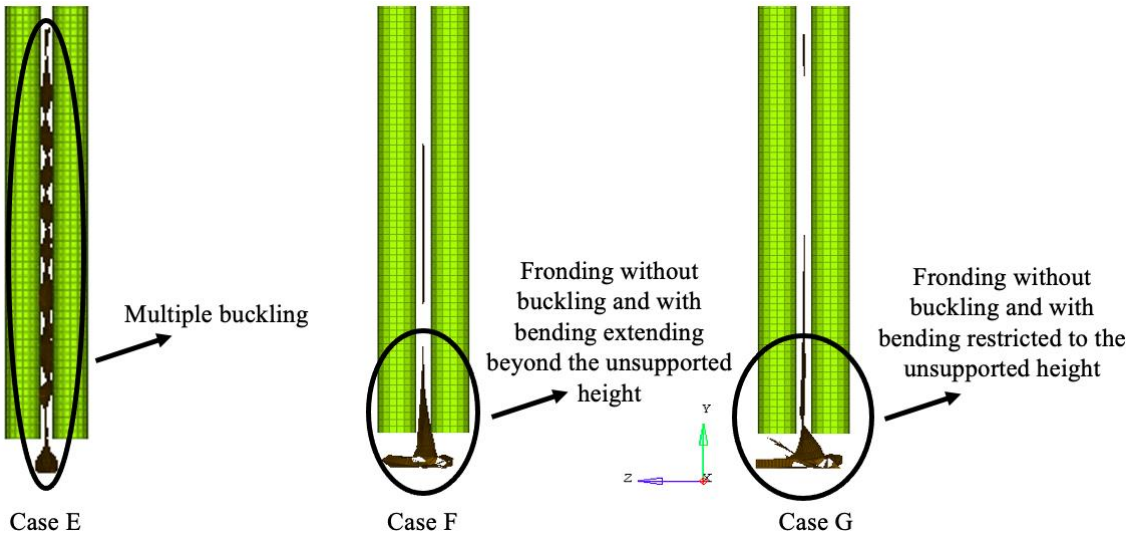

Figure 5.8: *Post-calibration comparison of the E, F and G cases (side-view)*

5.6. Final optimization run

Case G reported in the previous section was the final run case to obtain the calibrated material card for the macroscale model. It was run using the GRSM algorithm with absolute difference approach as the response function. The material card was populated with parameters for the purely elastic tensile formulation. The unsupported height was 10 mm and the anti-buckling column diameter and spacing were 10 mm and 65 mm respectively. The impact energy was 550 J with an impact velocity and mass of 7 m/s and 22 kg respectively. The specimen was made of a CFRP material with quasi-isotropic properties and measured 150 x 100 x 2.54 mm (4 plies). A mesoscale model that consisted of four plies separated by three layers of cohesive elements was also run using the above-mentioned parameters, functions and techniques and a comparison of both models with experimental results is shown in Figure **5.9**. In the trigger region, both models overestimated the force until 3 mm of displacement before closely following the experimental curve. The difference in the forces in the trigger region was because the trigger in the simulations had a different geometry as compared to the physical trigger. This observation follows conclusions in published literature that initial peaks are a function of the trigger modelling (41) (92) (129). Another reason for the overestimation of the force in the trigger region was the modelling of the base plate as a rigid body. This prevented any elastic deformation of the base plate

upon impact, which in turn made the contacts between the specimen and the base plate stiffer than the experimental setup, resulting in an overestimation of the force due to excessive stiffening. In the post-trigger region, calibrated models using both the approaches were able to capture the force-displacement behavior with a good degree of accuracy. The ADMF value for the macroscale model was 0.132, whilst that for the mesoscale model was 0.121 suggesting that the mesoscale model resulted in a better correlation with the experimental results owing to its robustness in capturing delamination behavior. Stroke displacement was modelled within 3% of the experimental value using both the modelling approaches. In the experiments the base plate flexed about 1 mm, which when accounted for would further reduce the error in the stroke displacement as the base plate was modelled as a rigid body in the numerical analysis. Run times for each macroscale and mesoscale simulation was 5 and 65 minutes respectively. Since each optimization was conducted for 50 simulations to arrive at the calibrated values, total run times for the optimization procedure were 4 and 54 hours, respectively, for the macroscale and mesoscale approaches. This is considerably less than typical time taken to calibrate using a trial-and-error approach, even though the time taken is a function of the skill of the user, which also influences the quality of the calibration. Hence, the optimization procedure, quantitatively, presents an accurate, efficient and objective approach to calibrating material cards for the purposes of composite crashworthiness.

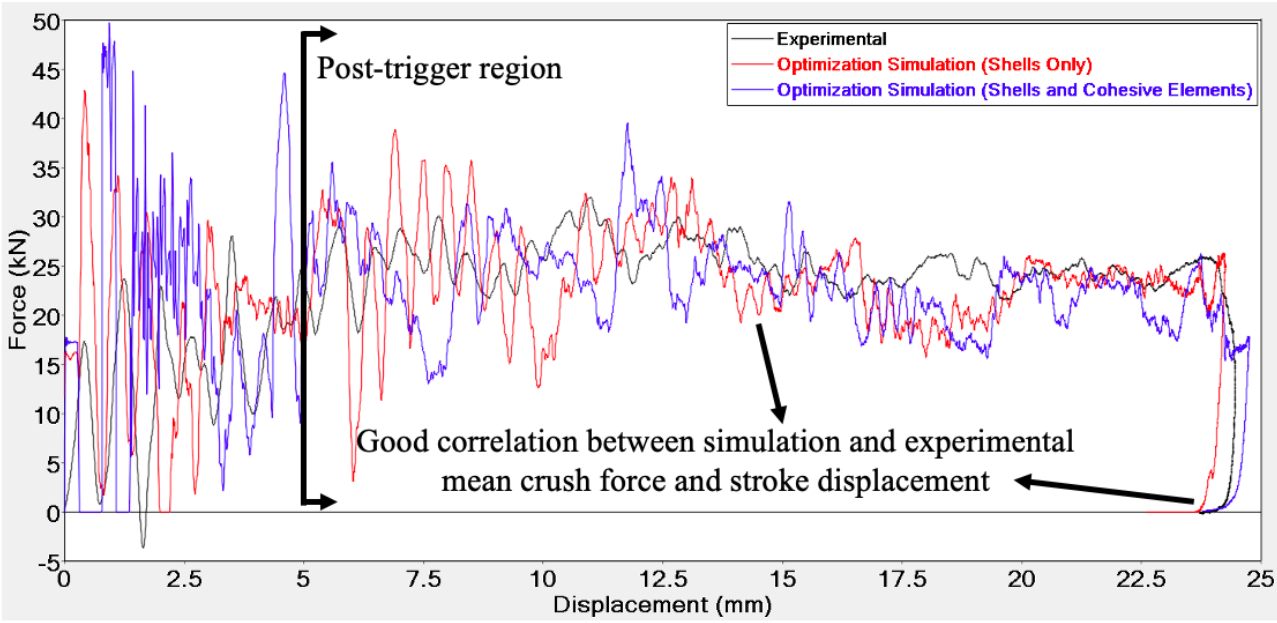

Figure 5.9: *Comparison of the experimental force-displacement curve with the final optimization runs for the macroscale and mesoscale approach (98)*

Optimal values for all the parameters are reported in Table **5.5**. The macroscale model modelled the composite plate as a stacked shell wherein a single shell element was made up of four separate plies. It, therefore, assumed perfect bonding between the plies. However, for the mesoscale model delamination behavior was modelled using cohesive elements. Since a strain-based failure model was used to model the failure of cohesive elements due to the absence of DCB and ENF testing data, which allows for an energy-based failure model to be used, energy absorption optima was higher using the mesoscale model as compared to the macroscale model. The

residual stresses were higher for the mesoscale models to allow for the increased energy absorption. Residual stress values as a percentage of the ultimate stresses are within the range of values reported in literature using LS-Dyna and Radioss solvers: 35 – 40% and 40 – 65 % for shear and compressive residual stresses respectively (21) (19) (27). Figure **5.10** shows the progression of the variables for all the optimization iterations for the two approaches. As can be observed, all variables converge to their values showing the robustness of the optimization approach. Since the values appear asymptotic, any further iterations run will only improve the results marginally.

Table 5.5: *Optimal values of all four parameters for both the approaches*

Parameter	**Macroscale Optima**	**Mesoscale Optima**
$W_p^{max}\ (J/mm^3)$	0.0846	0.4070
$\sigma_{rs}^{c1}, \sigma_{rs}^{c2}\ (MPa)$	132	187
$\sigma_{12rs}\ (MPa)$	34	39
$\sigma_{rs}^{c1}, \sigma_{rs}^{c2}\ (\%\ of\ ult.stress)$	40	56
$\sigma_{12rs}\ (\%\ of\ ult.stress)$	52	60

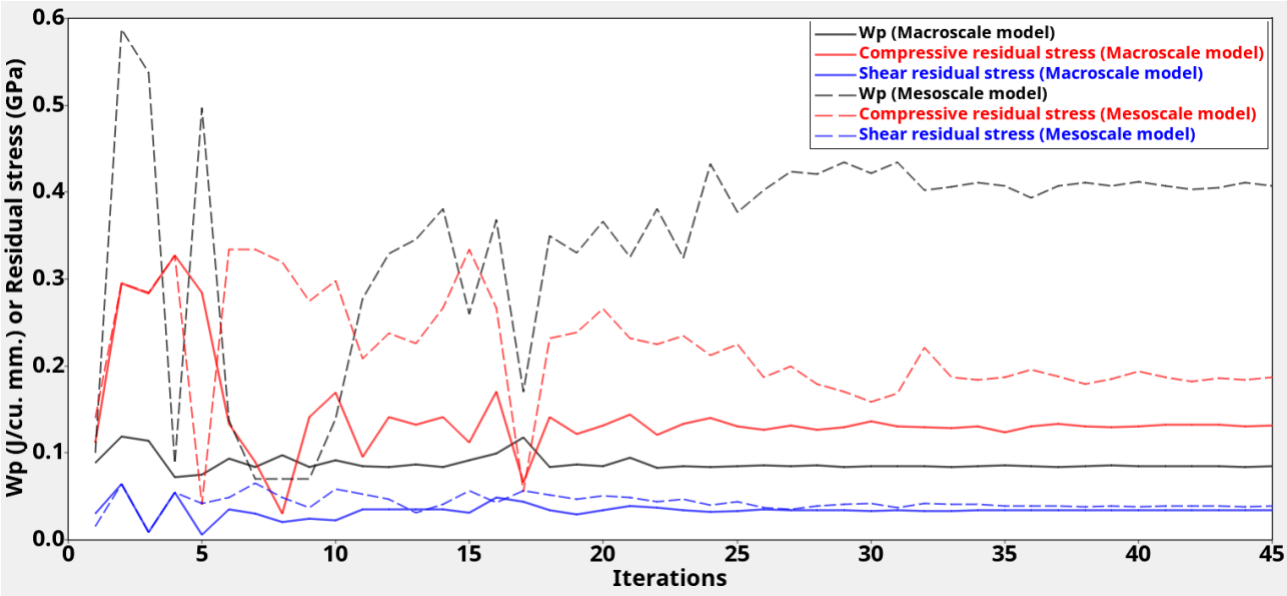

Figure 5.10: *Progression of the variables for the macroscale and mesoscale approaches*

Table **5.6** lists the correlations between the optimized parameters and the response function as obtained from HyperStudy. Correlation measures the strength between the associated variables, with a value closer to 1 indicating a stronger correlation and a value closer to 0 indicating a weaker correlation. As the loading was mostly compressive in nature with shear loading being introduced due to vibrations, the compressive residual stress had a larger bearing on the response values as compared to the shear residual stress, hence a larger value

for the correlation between the compressive residual stress and the response values as compared to that between the shear residual stress and the response values. Correlations with the residual stresses were consistent across the models for the residual stresses. Energy absorption had a significantly larger effect on the response value for the mesoscale model as compared to the macroscale model, as seen from increased correlation value for the same, probably because it allowed for occurrence of failure mechanisms such as delaminations and did not model contacts between the plies as perfectly bonded. Another contributing factor to the larger effect of energy absorption could be that friction forces accounted for only 15% of the energy absorption for the mesoscale model, while it accounted for 38% of the energy absorption for the macroscale model. Higher friction energy for the macroscale model was because the frond formation and debris from fragmentation accumulated at the bottom of the model resulting in more energy loss due to friction. However, for the mesoscale model fronds and fragmented elements translated sideways. Since less energy was attributable to friction energy, the energy absorbed by the plies could have had a greater effect on the response values.

Table 5.6: *Correlations between the optimized parameters and the response values*

Correlations with the Response Function	**Macroscale approach**	**Mesoscale approach**
W_p^{max}	0.31	0.61
Compressive Residual Stress	0.37	0.36
Shear Residual Stress	0.20	0.23

Figure **5.11** showcases the comparison between the damage progression as viewed from the side for both the mesoscale and macroscale models. As was expected, the macroscale model showcased very slight fronding due to the presence of a single layer of shell elements, whereas the mesoscale model exhibited delaminations and fronding behavior similar to that observed in experiments. Slight buckling was observed in the macroscale model, which was not the case for the mesoscale model. However, as can be seen from Figure **5.12** this buckling did not cause any plastic damage as no plastic strains were observed above the crushing area. Analysis of the damaged composite plate showed that one of the middle plies was crushed and it underwent significantly more fragmentation than the other three plies. Of the three remaining plies, two plies were crushed to one side and another to the other side. A similar behavior was observed in the numerical mesoscale model as shown in Figure **5.13**. To conclude, the optimization methodology developed was able to accurately, efficiently and objectively calibrate the material card and obtain good correlation with the experimental results, both qualitatively and quantitatively.

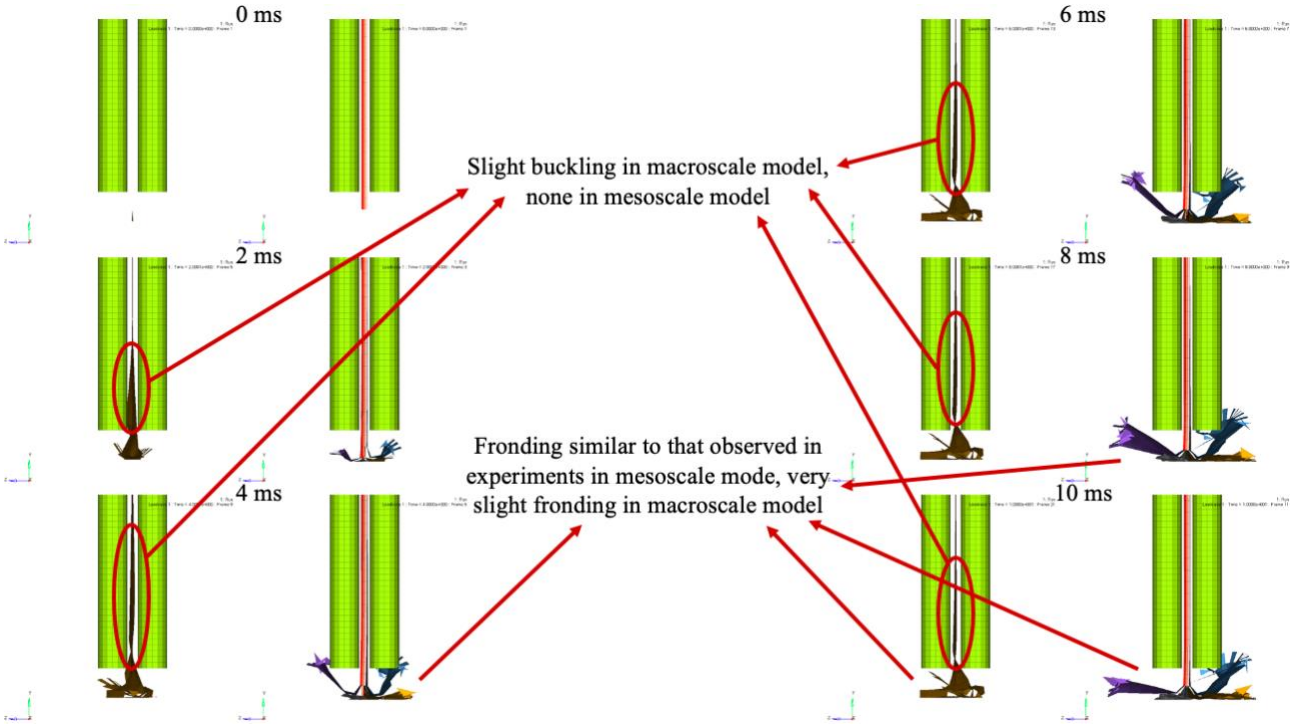

Figure 5.11: *Time-lapse comparison of the macroscale and mesoscale models (side view)*

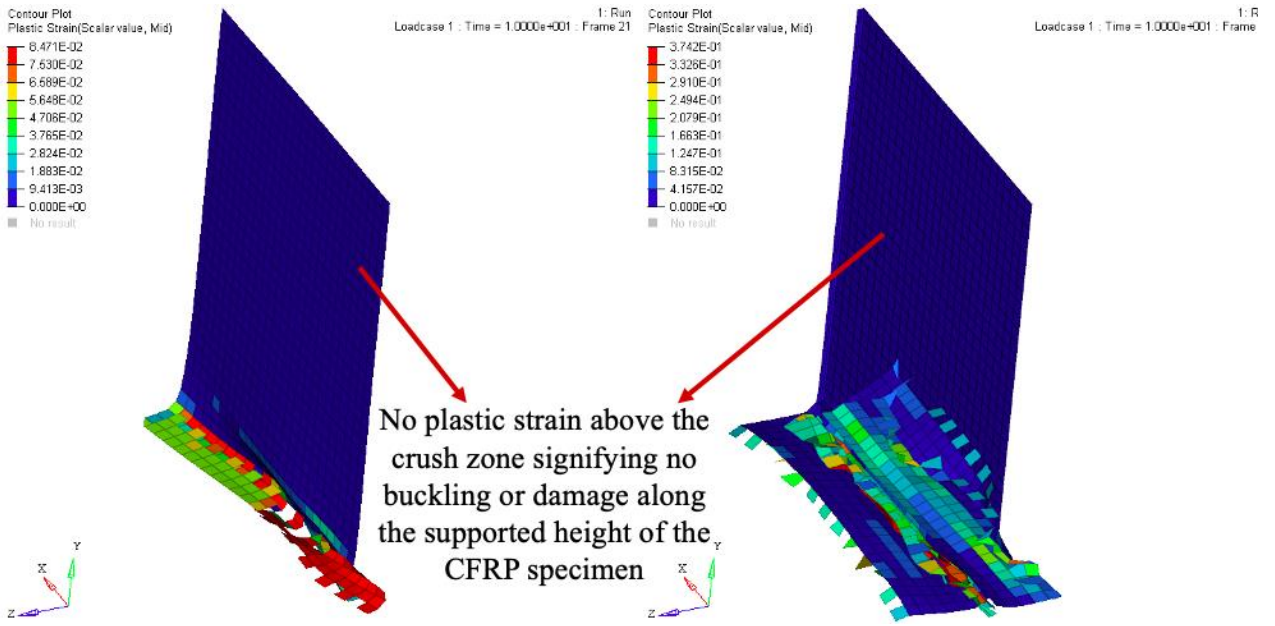

Figure 5.12: *View from the bottom of the final plastic strains observed in the macroscale and mesoscale models*

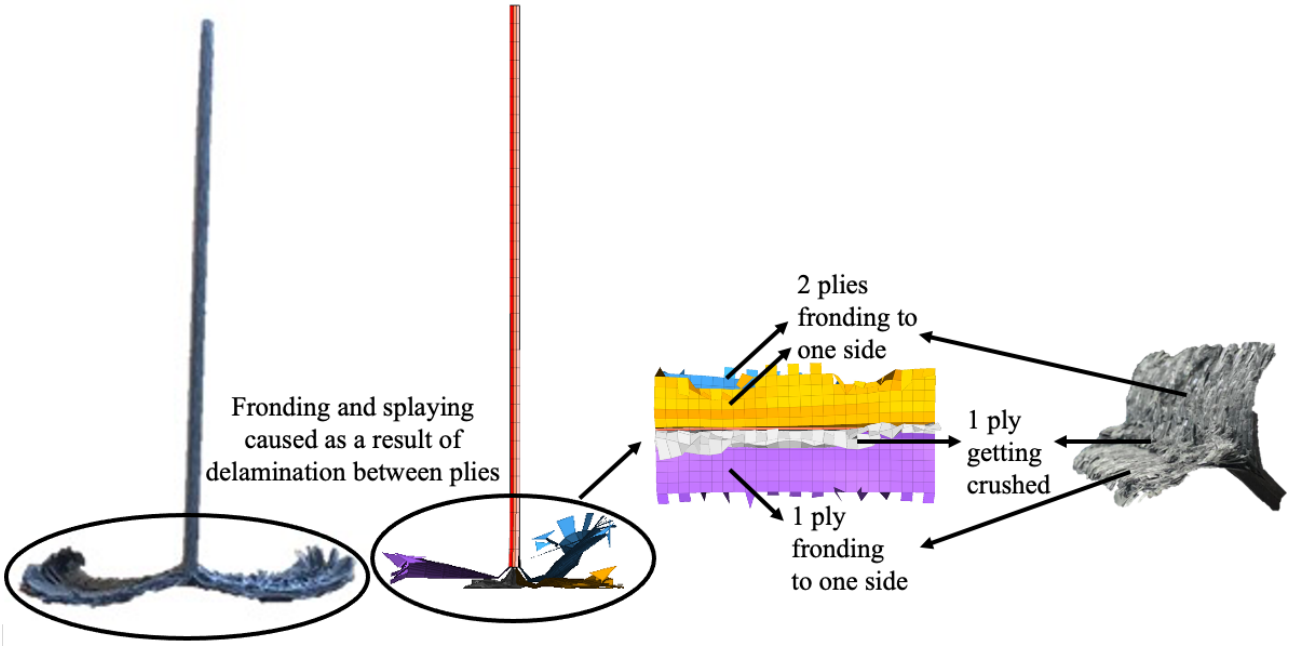

Figure 5.13: *Comparison of the fronding observed in the mesoscale model with that observed in the experiments (98)*

Appendix 9.1 shows the comparison between the calibrated and uncalibrated macroscale flat-plate models and the experimental force-displacement results. The uncalibrated model was run using default values for the calibrated parameters. As expected, the calibrated model showed a marked improvement as compared to the uncalibrated one.

6. Validation of Modelling Methodology

This chapter presents the numerical analysis conducted on the composite impact attenuator shown in Figure **3.11** in order to validate the methodology presented thus far. Results of the numerical models were compared with experimental results presented in another doctoral thesis, wherein the attenuator was impacted at four different impact velocities under a drop tower with an impact mass of 300 kgs at Picchio Spa (95). Table **6.1** lists the impact velocities and energies tested.

Table 6.1: *Impact velocity and energy levels*

Impact velocity (m/s)	Impact energy (J)
7.097	7555
7.101	7563
7.77	9056
8.04	9696

As can be seen from Figure **6.1**, all four impact velocities resulted in similar damage to the attenuator with the back and the front walls breaking off in the middle section and then caving in and the side walls getting crushed. The only difference was that a higher velocity resulted in damage extending further into the bottom section due to a higher impact energy. Although not shown in the images, high speed camera also captured buckling of the bottommost section upon impact (95) (98). Images of the attenuator impacted at 8.04 m/s were not available, but it exhibited behavior similar to that observed in the other three components (95).

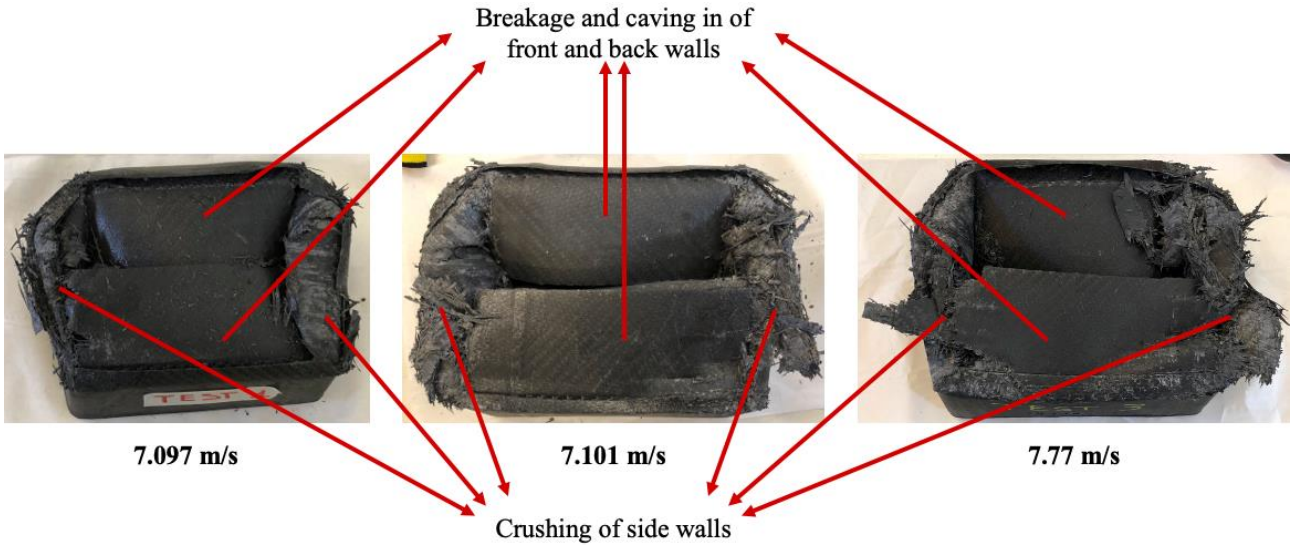

Figure 6.1: *Final damage of the impact attenuators at all four impact velocities*

The following sections presents the effects of a numerical modification made to the mesoscale model to account for the real geometry of the impact attenuator by activation of the Inacti flag and activation of the

advanced mass scaling (AMS) flag undertaken to decrease computation time, on the final results. Finally, a comparison is drawn between the numerical predictions and the experimental results.

6.1. Activation of *Inacti* flag

Initial numerical runs of the impact attenuator showed caving in of the innermost plies in the lowermost section that started at the interface between the middle and bottom sections. This aggravated the natural buckling of the front wall of the attenuator causing it to become unstable, thereby reducing the load bearing capacity of the crash box. This was caused due to geometry of the attenuator. Since the bottom section of the impact attenuator was made of plies 0.77 mm thick and the top and the middle sections were made of plies 0.75 mm thick, modelling the plies and cohesive elements with exact dimensions resulted in non-coincidence of nodes at the interface between the middle and bottom sections. This configuration, therefore, resulted in unnecessary buckling upon impact as shown in Figure **6.2** as the plies caused excessive shear deformation of the cohesive elements, resulting in their deletion. This behavior was not observed in physical testing due to the bridging of fibers across the interface during the curing process. Multiscale modelling could, perhaps, model this bridging and avoid the numerical behavior observed.

Since the cause of the problem was purely based on the meshing procedure and not the methodology, the modifications were made to the mesh. The thickness of the cohesive elements in the lowermost section was set equal to that of the other two sections (0.75 mm), without changing the ply thickness. This ensured that the nodes at the interface were coincident but resulted in penetrations (that lead to numerical instability and loss of data between nodes) between the plies in the lowermost section as they were spaced 0.75 mm apart but were 0.77 mm thick. Hence, the *Inacti* flag was activated in the contact model and set equal to six to numerically translate the nodes outward by 0.02 mm, thereby ensuring that there were no penetrations. This configurations with coincident nodes and no penetrations ensured behavior akin to that observed in physical testing by ensuring greater stability of the front wall and no caving in of the inner plies as shown in Figure **6.2**.

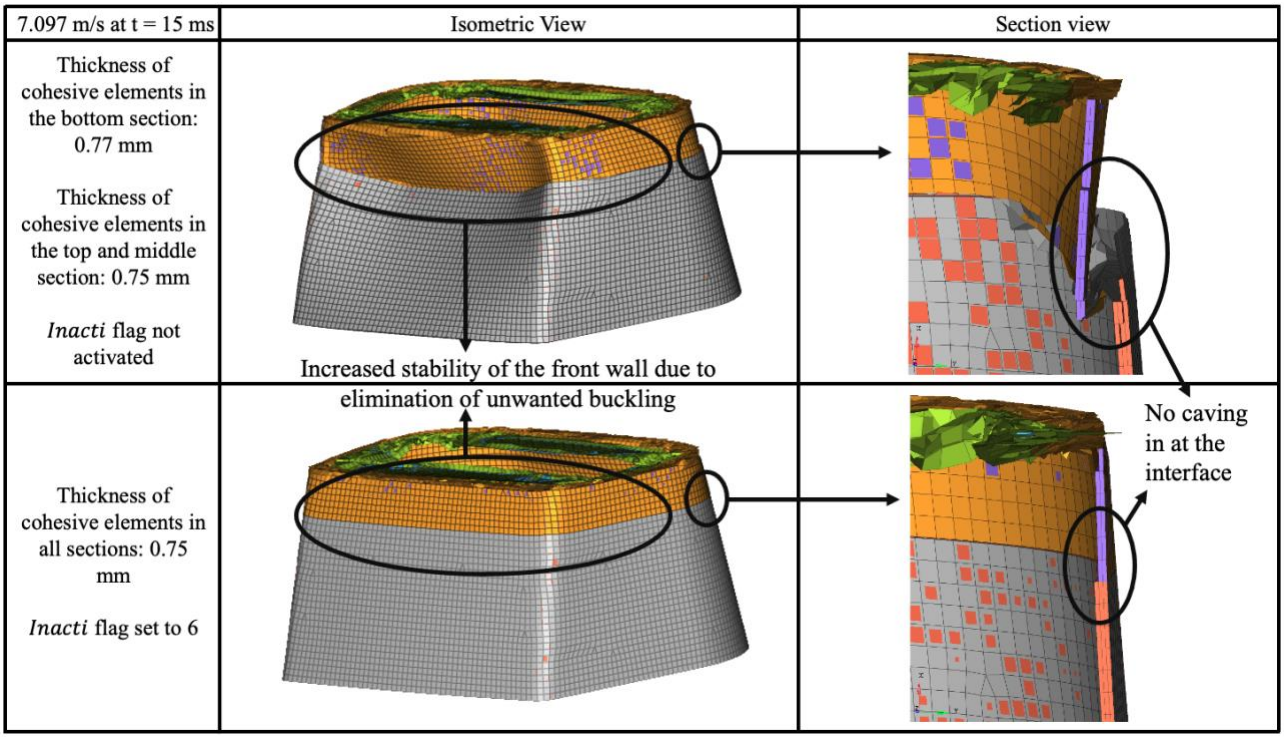

Figure 6.2: *Effect of the activation of the Inacti flag*

6.2. Activation of the AMS flag

Computation time for the macroscale model averaged about two hours for each run with six cores of Intel i7 CPU @ 2.70 GHz. This acceptable time period was because the time step for the macroscale models did not drop an order of magnitude for a prolonged time period and remained within 65% of the maximum (initial) time step for the majority of the run except when the impact velocity was 7.097 m/s, wherein it dropped to 15% of the maximum (initial) time step as shown in Figure **6.3**. However, this was not the case for the mesoscale approach, wherein the time step at times dropped two orders of magnitude and stayed at least an order of magnitude lower than the maximum (initial) time step as can be seen from Figure **6.3**. Mesoscale models were run with Altair's HPC cluster (16 nodes of Intel Xeon CPU E5-2667 v3 @ 3.20GHz), which limited the run time to 120 hours; hence, some simulations terminated after 5 – 15 mm displacement into the lowermost section of the impact attenuator.

To be able to run simulations on standard FCA hardware and obtain results within an acceptable time period, the AMS flag was activated, and the simulations run with the standard six cores of Intel i7 CPU @ 2.70 GHz. AMS flag activation is known to not affect the results significantly if the material is not hyper-elastic and the minimum time step is sufficiently lower than the initial time step (130). Through the activation of the flag, the minimum time step was fixed at 66% of the maximum (initial) time step. Since time step is a function of the element size, which varies during the simulation, and the speed of sound in the medium, which, in this case, was constant throughout the simulation as the composite stiffness and density were constant, this value for the minimum time step was considered reasonable. As the load case was mostly compressive and shearing in nature, it meant that only extremely deformed (hourglassed or skewed) cohesive elements could result in the

time step falling below 66% of the initial time step. Shell elements (plies) should have been damaged and deleted by the calibrated material law. If, however, any shell elements were not deleted and were guiding the time step, they would have been damaged and/or fragmented and would, therefore, not be carrying any significant load. Hence, activation of the AMS flag was not thought to affect the results significantly, while it had the potential to reduce the computation time significantly (as can be seen in Figure **6.3** from the constant value for the time step with AMS activation (solid black line) as compared with the drop in the time step without AMS activation (multicolored dashed lines)) and allow the simulation to run on standardized hardware available at FCA.

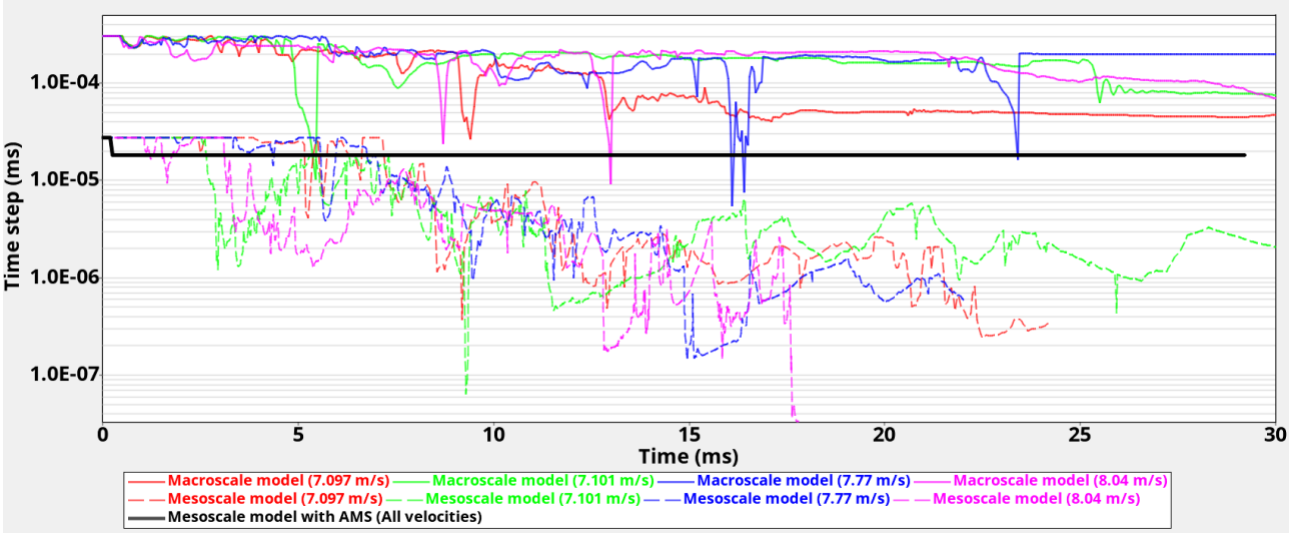

Figure 6.3: *Time step for the macroscale and mesoscale (with and without AMS flag activation) models*

Qualitative comparison between the damaged specimens revealed no significant difference between the models run with and without activation of the AMS flag as can be seen from Figure **6.4**. At an impact velocities of 7.101 and 7.77 m/s, the model without AMS activation exhibited slightly greater buckling of the front wall as compared to the model with AMS activation. Other than that, models at other velocities did not exhibit any significant difference between the two approaches for the damage progression as viewed from the simulations. Quantitative comparison between the two approaches is detailed in the following section and in Table **6.2**

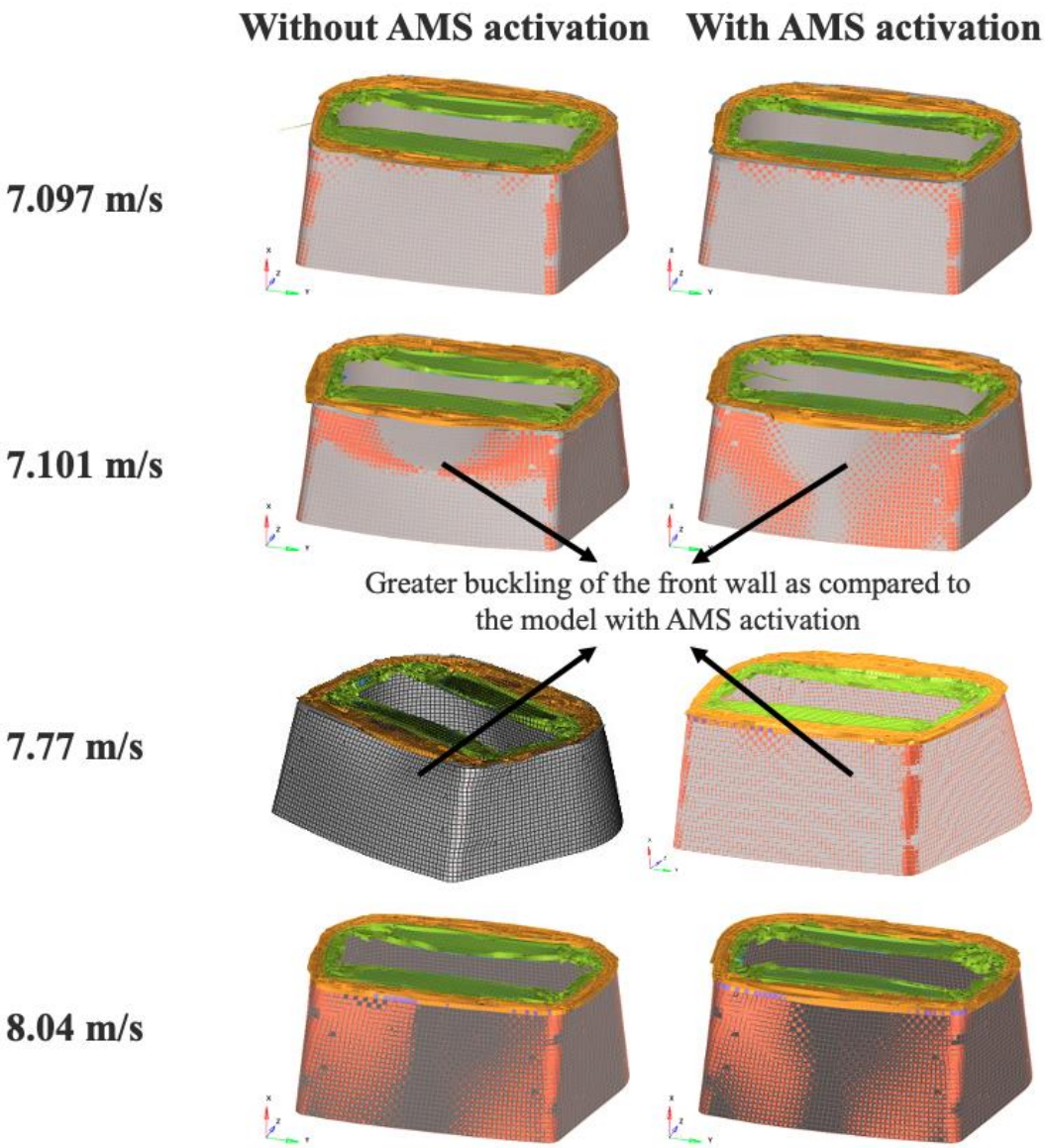

Figure 6.4: *Qualitative comparison of the impact attenuator final damage with and without activation of the AMS flag*

6.3. Numerical prediction comparison with experimental results

Twelve different numerical simulations were run on the composite impact attenuator: four each for every impact velocity using the macroscale, mesoscale (with AMS activation) and mesoscale (without AMS activation) approaches. Runs with the macroscale and mesoscale (with AMS activation) were run almost until the force dropped to zero, whilst that for the mesoscale (without AMS activation) were run for 120 hours (maximum run time on the Altair HPC cluster). Although the latter runs were time constrained, 120 hours were sufficient for the impact to reach the lowermost section and allow for the calculation of the mean crush forces for impact velocities except for 7.097 and 8.04 m/s, for which the simulation stopped 10 mm into the bottom section during which the interface peak had not sufficiently reduced to the mean crush force.

Table **6.2** shows the comparison between the experimental and the twelve simulation data sets for final displacement and mean crush force for each section and the entire attenuator that were derived from the force-displacement graphs for all four energy. Figure **6.5** shows the force-displacement comparison between

numerical and experimental results at an impact velocity of 7.097 m/s, whilst the same for the other three impact velocities are shown in appendix 9.2. Initial peak seen in the numerical force-displacement data was attributable to contact stiffening due to the rigidity of the base, as was the case for the flat-plate model, and the absence of a numerical trigger to initiate crushing. Similar peaks were also a characteristic of other published works on numerical analysis of composite components under a crushing load (82) (131). The experimental force-displacement graph exhibited a stepwise increase in the average crush force due to the presence of an extra ply in each subsequent section, a behavior that was predicted by all the simulations. However, the transition between the forces at the interfaces was more gradual in the experimental results, whilst it was more abrupt in the numerical analysis suggesting that the thickness increased gradually in the physical impact attenuators, whereas the thickness change in the numerical models was more abrupt. This abrupt change in thickness led to the peaks observed at the interfaces (46 and 116 mm). Use of a finer mesh and gradual increase in thickness at the interface, akin to the physical component, could have, possibly, reduced these peaks.

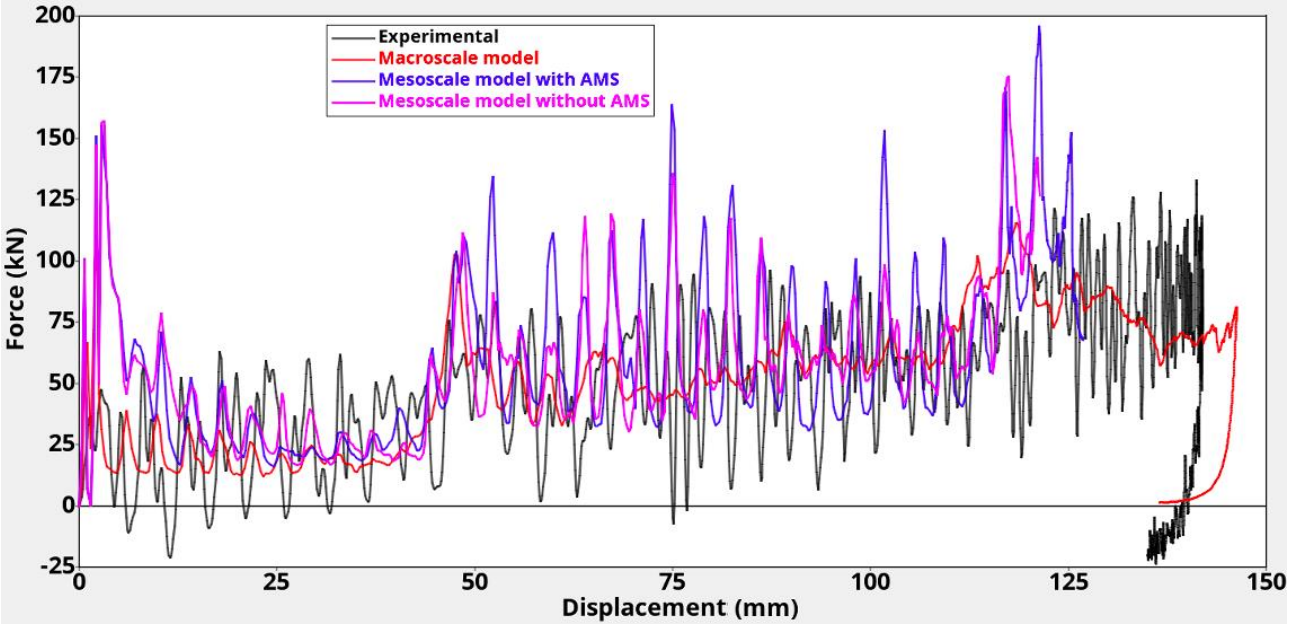

Figure 6.5: *Force-displacement result comparison at 7.097 m/s impact velocity*

Quantitative analysis presented in Table **6.2** revealed that the mesoscale approach resulted in improved prediction of the final displacement and mean crush force in each section and the impact attenuator (global) as compared to the macroscale approach because the percent error, as computed using equation 6.1, was lesser for the former as compared to the latter. This was expected because of the robustness of the mesoscale approaches in modelling the failure modes. Of the two mesoscale approaches, one without the activation of the AMS flag predicted the impact behavior more accurately as compared to the one with the activation of the AMS flag. Even though there was a difference in the prediction between the two, it was not significant, especially considering that AMS activation resulted in a substantially more efficient computation model both in terms of computation time and power. Notwithstanding this, the mesoscale model with AMS activation still predicted a majority of the parameters within a 10% error band. As mentioned previously, numerical analysis of mesoscale models without AMS activation was terminated prior to its completion for impact velocities

7.097, 7.77 and 8.04 m/s due to limited availability of computational resources on the HPC cluster. Hence, displacement values for these impact velocities were extrapolated. Mean crush force in the bottom section for 7.097 and 8.04 m/s cases could not be computed due to the unavailability of sufficient data for a prolonged displacement. Mean crush forces and their standard deviation for the experimental model were calculated between 0 – 46 mm, 46 – 116 mm and > 116 mm for the top, middle and bottom sections respectively.

$$Percent\ error = \frac{|Numerical\ Value - Experimental\ Value|}{Experimental\ Value} \times 100 \qquad 6.1$$

Error in the final displacement was less than 10% for all the mesoscale models and two of the macroscale models, suggesting good prediction of the same. Errors for the mean crush forces were between 5 – 38% using the macroscale approach, with higher values reported for the bottom section because local buckling gave way to crack formation from the bottom, which significantly decreased the load carrying capacity of the component. Although errors for the mesoscale approaches were also within the same range, they were mostly in the green band (0 – 10% error) than in the yellow (10 – 20% error) and red bands (> 20% error) as compared to the macroscale approaches, suggesting that the mesoscale approaches predicted the mean crush forces more accurately. Simplicity of the model and non-flexing nature of the base plate that made the model stiffer could be the reasons for this crack formation that originated from the bottom. Experimental standard deviation generally increased with displacement, because of the decreasing momentum of the impactor that resulted in increased vibrations in the entire system. This trend was observed also in the numerical analysis. Standard deviation of the mean crush force in the middle and bottom sections were almost equal for the experimental and mesoscale approaches, whilst it was lower for the macroscale approach because of its simplicity in modelling the failure modes. However, standard deviation of the mean crush force in the top section was significantly lower for all numerical models as compared to experimental results. A plausible explanation for this could be the higher stiffness and rigidity of the numerical model initially due to the presence of rigid bodies and absence of lateral supports (that also act as dampers) in the numerical model that ensured that the impact attenuator stayed in its position in the experimental tests. Standard deviation for global mean crush force, both experimental and numerical, was higher than that for the mean crush force for the sections. This was expected due to the increasing nature of the force-displacement curve caused because of the increasing cross-sectional area of the impact attenuator. 15 – 20% of the energy was absorbed due to friction, with the mesoscale models absorbing a larger amount of energy due to the increased exposed surface area. An increase in the impact energy marginally increased the frictional energy absorption because of the higher displacement, which is expected.

Table 6.2: *Displacement and mean crush force prediction comparison of numerical values with experimental results for the impact attenuator*

7.097 m/s	**Experimental**	**Macroscale model**	**Mesoscale model with AMS**	**Mesoscale model without AMS**
Final displacement (mm)	141.93	146.99 (3.57%)	129.08 (9.05%)	134.21* (5.44%)
Top section mean crush force (kN)	24.58 (19.66)	21.87 (13.82) (11.03%)	26.25 (7.7) (6.79%)	25.5 (7.37) (3.74%)
Middle section mean crush force (kN)	53.61 (21.10)	58.72 (13.61) (9.53%)	63.68 (25.45) (18.78%)	62.66 (19.21) (16.88%)
Bottom section mean crush force (kN)	82.71 (22.56)	76.84 (14.45) (7.10%)	104.45 (31.83) (26.28%)	--
Global mean crush force (kN)	54.13 (28.66)	49.58 (30.49) (8.41%)	69.67 (32.87) (25.01%)	58.82 (32.09) (7.97%)
7.101 m/s				
Final displacement (mm)	137.75	146.80 (6.57%)	129.12 (6.26%)	128.15 (6.97%)
Top section mean crush force (kN)	27.30 (23.66)	23.80 (15.39) (12.82%)	26.89 (6.33) (1.50%)	27.87 (9.31) (2.09%)
Middle section mean crush force (kN)	61.57 (24.68)	50.64 (15.62) (17.75%)	63.51 (21.81) (3.15%)	63.18 (24.13) (2.61%)
Bottom section mean crush force (kN)	99.05 (21.17)	86.90 (10.61) (12.27%)	92.13 (23.67) (6.99%)	95.47 (26.91) (3.61%)
Global mean crush force (kN)	61.38 (33.16)	59.68 (28.37) (2.77%)	64.68 (30.85) (5.38%)	67.32 (33.15) (9.68%)
7.77 m/s				
Final displacement (mm)	143.73	175.04 (21.78%)	145.04 (0.91%)	142.31* (0.99%)

Top section mean crush force (kN)	28.91 (20.69)	20.35 (14.35) (29.61%)	29.57 (8.32) (2.28%)	28.84 (9.76) (0.24%)
Middle section mean crush force (kN)	61.06 (29.10)	49.91 (17.37) (18.26%)	65.00 (23.14) (6.45%)	63.78 (15.01) (4.45%)
Bottom section mean crush force (kN)	132.50 (36.02)	81.05 (7.87) (38.83%)	109.46 (13.81) (17.38%)	113.05 (23.99) (14.68%)
Global mean crush force (kN)	75.74 (51.54)	58.21 (30.25) (23.14%)	62.91 (32.75) (16.94%)	64.39 (32.75) (14.98%)
8.04 m/s				
Final displacement (mm)	157.02	180.25 (14.8%)	152.08 (3.15%)	153.64* (2.15%)
Top section mean crush force (kN)	25.59 (22.45)	21.66 (14.90) (15.36%)	28.71 (11.90) (12.19%)	27.78 (8.47) (8.56%)
Middle section mean crush force (kN)	56.25 (24.97)	55.35 (13.68) (1.60%)	65.86 (27.04) (17.08%)	61.76 (19.46) (9.80%)
Bottom section mean crush force (kN)	108.76 (28.59)	72.11 (8.56) (33.69%)	96.06 (27.96) (11.68%)	--
Global mean crush force (kN)	52.33 (28.45)	58.91 (22.47) (12.56%)	71.19 (32.11) (36.06%)	54.63 (27.80) (4.39%)
				-- Data not available
				* Extrapolated data
				Value (Standard deviation) (Percent error)
Percent error = 0 – 10 %		Percent error = 10 – 20 %		Percent error > 20 %

Figure **6.6** shows the final damage comparison between the macroscale and mesoscale (with AMS activated) approaches at all four energy levels. In the macroscale models, crack formation occurred at the bottom and the crack propagated along half the length of the bottom section of the front wall for all impact velocities except 7.77 m/s, which buckled and crushed. This cracking behavior gave rise to slight cracking and bucking in the right wall of the attenuator. These behaviors were not observed in both the mesoscale models and the experimental tests (see Figure **6.1**). Crack formation and buckling in the bottom section led to a marked decrease in the load carrying capacity of the macroscale impact attenuator, thereby causing it to damage over

a longer displacement leading to a higher error in the final displacement as compared to mesoscale impact attenuator (see Table **6.2**). This damage behavior was caused due to higher stiffness of the component when modelled using a macroscale approach as compared to when it was modelled with the mesoscale approach. Perfect bonding between the plies due to the stacked shell approach used in macroscale modelling caused this higher stiffness, whereas the bonding between the plies was elastoplastic in nature and could damage in the mesoscale model allowing it to deform and absorb energy during crushing. Higher stiffness of the mesoscale models could also be because of increased contacts (which behave as springs) between elements, as each ply was modelled separately. Macroscale models, however, were able to replicate the breakage and caving in of the front and back walls in a similar manner to what was observed in experimental tests. Mesoscale models were not able to simulate this behavior due to the higher value of the deletion criterion (see Table **5.5**), which resulted in non-deletion of the elements after rupture along the creases of the broken walls, thereby causing the damaged walls to stay along the plane of the impactor (perpendicular to impact direction) even after cracking. This resulted in slightly higher peaks for the mesoscale model as compared to the experimental data during sustained crushing for all three sections due to a larger number of elements staying in contact with the steel impactor. Both the approaches were able to model the side wall crushing, with the mesoscale approach modelling it more accurately due to its robustness as compared to the macroscale models.

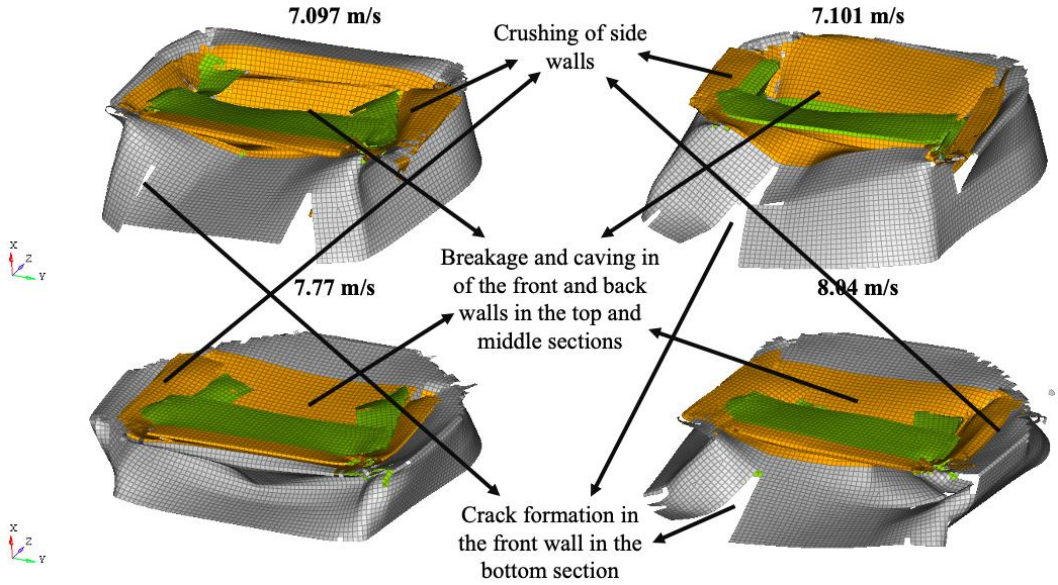

(a)

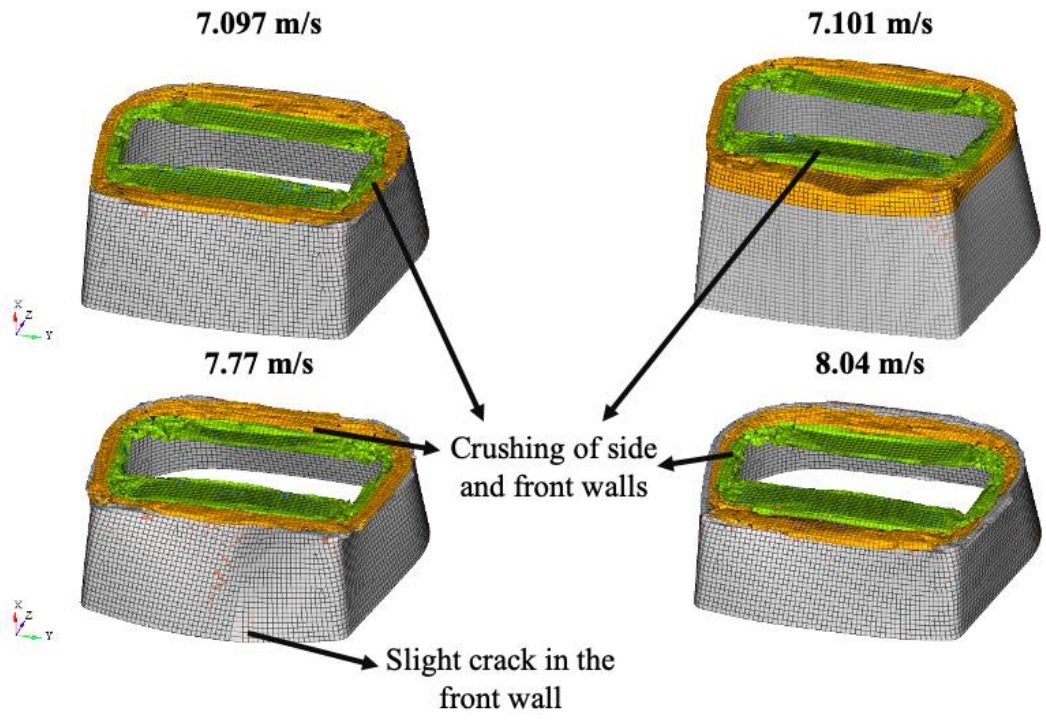

(b)

Figure 6.6: *Comparison of final damage using the macroscale (a) and mesoscale (with AMS) (b) approaches at all four energy levels*

Figure **6.7** shows a time lapse of the damage progression comparing the macroscale and mesoscale models and also shows only the cohesive elements of the mesoscale model as the crushing progressed. Behaviors previously mentioned can be seen as they progress through the crushing phase in the time lapse. Damage initiates from the top for both the models similar to the experiments. Cohesive elements were deleted along the direction of the impact as the damage progressed, ensuring the attenuator damaged progressively. Some cohesive elements were not deleted for the top and middle sections for the front and back walls suggesting that the plies cracked and folded towards the middle, similar to experimental tests. As mentioned before, since the elements were not deleted the plies did not cave towards the cavity as was observed in the macroscale models and experiments. The mesoscale approach predicted the qualitative and quantitative crushing behavior with greater accuracy as compared to the macroscale approach. However, macroscale approach was able to predict the general behavior and overall trends with a greater efficiency. Hence, the macroscale approach could be used in the pre-design stage, whilst the mesoscale approach can be used for the detailed design process.

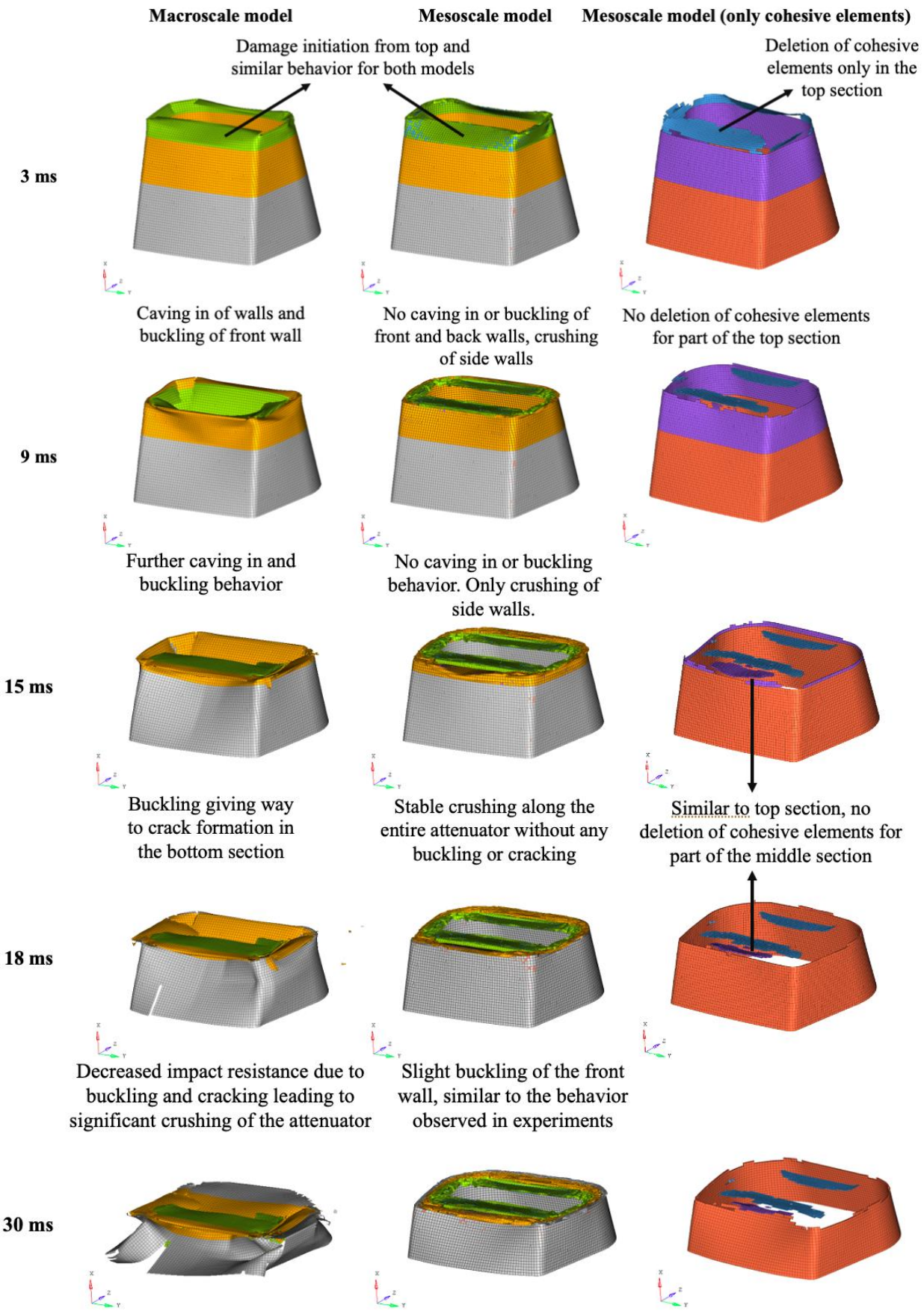

Figure 6.7: *Time lapse of damage progression for the numerical macroscale and mesoscale (complete model and cohesive elements only both with AMS) models at an impact velocity of 8.04 m/s*

7. Conclusions and Outlook

This dissertation focused on developing a methodology to predict the impact behavior of composite components. In order to arrive at this methodology, two steps need to be accomplished: first the material modelling data was needed and then a computational procedure to effectively simulate the specific collapse and crash of composite parts was needed.

An analysis of the existing material data and models put in evidence a lack of information and the need of an experimental procedure to complete the material characterization. With this aim a fixture was designed in collaboration with Instron that could test flat composite plates up to 150 x 100 x 16 mm and an impact energy of 1850 J. During the design activity it became clear that constructive details had to be decided and an intensive FEA analysis was conducted to obtain the parameters for the same. FEA analysis was used to determine the distances between the thickness of the anti-buckling columns that ensured progressive crush behavior originated from the trigger (bottom) of the plates and propagated upwards along the length of the plate. Thickness of the top plate was also optimized to ensure that an impact of 1850 J resulted solely in elastic deformation along the entire surface of the plate. A numerical study confirmed that the fixture could initiate progressive crush behavior for flat plates of various thicknesses and stiffnesses up to 1850 J. During physical testing, the fixture did not artificially add any failure modes, ensured unimpeded propagation of the crush fronds and allowed for easy egress of the damaged composite plates, which was a marked improvement over its counterparts, thereby fulfilling its objectives.

Upon the specific request of the industrial partner CRF, the simulation was developed in the RADIOSS environment to allow synergies with the existing architecture. Four models were created: two each that represented the flat composite plate testing in the fixture and impact attenuator testing under a drop tower. Flat composite plate testing was conducted to calibrate the specific material card available in the selected simulation code, whilst the impact attenuator testing was conducted to validate the methodology. Both the flat plate and the impact attenuator models were modelled using macroscale and mesoscale approaches. The former modelled the composite specimen using single stacked shell elements, whilst the latter introduced cohesive elements between the plies in order to capture the delamination behavior. All models were created using HyperMesh.

Entire force-displacement graphs obtained from experimental testing were used to calibrate the specific numerical model of the composite material. Calibration was conducted using optimization algorithms in HyperStudy in order to reduce the calibration time through automation and to obtain optimum values, both of which are not possible using the trial-and-error approach. Studies were conducted to arrive at the most accurate response functions and optimization algorithms, ones that provided the best correlation between the experimental and numerical force-displacement graphs. They revealed that the absolute difference between the experimental and numerical force more accurately (22%) captured the force-displacement behavior as compared to the squared difference between the forces. The ARSM algorithm was marginally (4%) more

accurate than the GRSM algorithm. Both techniques were equally efficient, but the GRSM algorithm required the user's intervention for termination as it repeatedly arrived at the optimum due to the absence of a convergence criteria. However, the GRSM algorithm showed a progressive decrease and a convergence in the response function, whereas the ARSM algorithm showed no such behavior. Due to this progressive behavior and convergence, GRSM was used for the final calibration. ARSM could be used in the industry owing to its ability to terminate automatically after satisfying the convergence criteria. Four parameters, specific to the material model available in the RADIOSS environment, were calibrated: energy absorption per unit volume, compressive residual stress in 1 and 2 directions and shear residual stress in the 12 direction. The fixture allowed the calibration of these parameters as they could not be obtained directly from standard material characterization tests.

The mesoscale model was able to capture the force behavior more accurately (9%) as compared to the macroscale model, which was expected as it captured failure modes more accurately. Both models captured the stroke displacement within 3% of the experimental values. However, each iteration of the macroscale model concluded in 5 minutes, whilst it concluded in 65 minutes for the mesoscale model suggesting that the former was more efficient than the latter. Macroscale models could be used for preliminary studies as its accuracy was within 10% of the mesoscale models. Owing to the presence of cohesive elements, the mesoscale model was able to capture the physical damage behavior more accurately than the macroscale model and exhibited fronding and fragmentation behavior similar to that observed in experimental tests. Correlation with the experimental force improved significantly after the trigger region because the trigger was not modelled similar to its physical counterpart. Modelling the trigger region with a finer mesh and exactly as machined physically would improve the correlation in the trigger region. The effect of the compressive residual stress on the response values was comparatively larger as compared to the shear residual stress because of the nature of the loading.

For the final validation of the numerical methodology and to justify the use of the fixture in developing this methodology, an analysis of the crash behavior of an impact attenuator was conducted through experimental tests and numerical simulations. Numerical analysis of the impact attenuator at four different energy levels revealed that the methodology was able to predict the mean crush force and final displacement without any change in the numerical formulations. Mesoscale models predicted the quantitative and qualitative impact behavior more accurately as compared to the macroscale model due to the presence of cohesive elements that allowed for more realistic capture of energy dissipation mechanisms. Final displacement values for the mesoscale models were within 10% of the experimental results, while those for the macroscale models were within 10% for two load cases and were off by 14% and 22% for the other two cases. A majority of the mean crush force parameters were within 10% of the experimental results using the mesoscale models, while the error for the macroscale models was greater. Higher errors for the macroscale models were because composite laminates were modelled as stacked shell elements that assumed perfect bonding between the plies, thereby making the model stiffer. This resulted in crack formation in the lowermost section, which significantly

reduced the load bearing capacity of the impact attenuator. Although errors for the mesoscale model were within an acceptable range, they could have been reduced had an energy-based failure criterion been used to model cohesive failure, values for which could have been obtained from DCB and ENF testing. This would also have resulted in a lower calibrated value of the energy absorption per unit volume parameter, which would also have allowed cracking of the front and back walls of the attenuator, ultimately improving the physical damage (qualitative) prediction. Furthermore, use of a finer mesh at section interfaces and numerical trigger at the top would have reduced the numerical peaks observed. A flag activation done for the mesoscale models resulted in a significant decrease in the computation time and power required whilst ensuring that the error stayed within an acceptable margin.

The validated methodology has the capability to predict impact damage for large composite components and can be used to design primary crash structures used in the automotive industry and increased use of virtual testing, thereby leading to savings in resources spent on research and development. Ultimately, this could increase the use of composite materials in vehicles making them lighter, resulting in fewer emissions.

8. References

1. Britannica. Nicolas-Joseph Cugnot. [Online] July 20, 1998. [Cited: October 19, 2020.] https://www.britannica.com/biography/Nicolas-Joseph-Cugnot.

2. —. Karl Benz. [Online] July 20, 1998. [Cited: October 19, 2020.] https://www.britannica.com/biography/Karl-Benz.

3. —. Model T. [Online] July 20, 1998. [Cited: October 19, 2020.] https://www.britannica.com/technology/Model-T/additional-info#history.

4. United States Environmental Protection Agency. Fast Facts on Transportation Greenhouse Gas Emissions. [Online] June 2020. [Cited: October 19, 2020.] https://www.epa.gov/greenvehicles/fast-facts-transportation-greenhouse-gas-emissions.

5. European Parliament. CO2 emissions from cars: facts and figures (infographics). [Online] March 22, 2019. [Cited: October 19, 2020.] https://www.europarl.europa.eu/news/en/headlines/society/20190313STO31218/co2-emissions-from-cars-facts-and-figures-infographics.

6. European Commission. Reducing CO2 emissions from passenger cars - before 2020. [Online] [Cited: October 19, 2020.] https://ec.europa.eu/clima/policies/transport/vehicles/cars_en.

7. US National Highway Traffic Safety Administration. *2017 and Later Model Year Light-Duty Vehicle Greenhouse Gas Emissions and Corporate Average Fuel Economy Standards.* Washington DC, USA : National Highway Traffic Safety Administration, 2012.

8. Fan, J. *Lightweight Composite Structures in Transport: Design, Manufacturing, Analysis and Performance.* J. Njuguna. Duxford, UK : Elsevier, 2016. pp. 3-34.

9. World Health Organization. Road traffic injuries. [Online] February 7, 2020. [Cited: October 19, 2020.] https://www.who.int/news-room/fact-sheets/detail/road-traffic-injuries#:~:text=Approximately%201.35%20million%20people%20die,road%20traffic%20crashes%20by%202020..

10. EUROCOMPULSION. ALFA ROMEO 4C CARBON FIBER CHASSIS INFORMATION. [Online] August 02, 2016. [Cited: October 19, 2020.] https://shopeurocompulsion.net/blogs/technical-articles/alfa-romeo-4c-carbon-fiber-chassis-info.

11. BMW. BMW 7 Series' Carbon Core more important that you might think. *BMW Blog.* [Online] September 01, 2015. [Cited: October 19, 2020.] https://www.bmwblog.com/2015/09/01/bmw-7-series-carbon-core-more-important-that-you-might-think/.

12. Almajid , A. A. and Friedrich, K. - *Manufacturing Aspects of Advanced Polymer Composites for Automotive Applications.* Applied Composite Materials, February 10, 2013, Vol. 20, pp. 107-128.

13. Guillon, D, et al. Cetim, Momentive develop composite crashbox concept. *Automotice Engineering.* August 01, 2014.

14. J. K. Kim and T. X. Yu - *Energy Absorption Characteristics of Crash Worthy Structural Composite Materials,* Key Engineering Materials, Ramakrishna S. and Hamada, Hiroyuki. September 1997, Vols. 141-143, pp. 585-622.

15. Savage, G, Bomphray, I and Oxley, M. - *Exploiting the fracture properties of carbon fibre composites to design lightweight energy absorbing structures.* Engineering Failure Analysis, 2004, Vol. 11, pp. 677-694.

16. Heeps, G. Carbon Footprint. *Crashtest Technology International.* August 19, 2012, pp. 36-40.

17. Rouchon, J. - *Certification of Large airplane Composite Structures, Recent Progress and New Trends in Compliance Philosophy.* proc. of 17th Congress of the International Council of the Aeronautical Sciences. 1990.

18. Arteiro, A, et al. - *Simulation of the Mechanical Response of Thin-Ply Composites: From Computational Micro-Mechanics to Structural Analysis.* Archives of Computational Methods in Engineering, 2019, Vol. 26, pp. 1445-1487.

19. Andersson, M and Liedberg, P. - *Crash behavior of composite structures - A CAE benchmarking study.* Goteborg, Sweden : Chalmers University of Technology, 2014. Master's Thesis.

20. Bames, G, et al. - *Crash safety assurance strategies for future plastic and composite intensive vehicles (PCIVs).* United States National Highway Traffic Safety Administration, 2010.

21. Wade, B. - *Capturing the Energy Absorbing Mechanisms of Composite Structures under Crash Loading, University of Washington.* Seattle, WA, USA : University of Washington, 2014. PhD Thesis.

22. Cherniaev, A, Butcher, C and Montesano, J. *Predicting the axial crush response of CFRP tubes using three damage-based constitutive models.* Thin-Walled Structures, 2018, Vol. 129, pp. 349-364.

23. Boria, S. - *Sensitivity Analysis of Material Model Parameters to Reproduce Crushing of Composite Tubes.* Journal of Materials Engineering and Performance, 2019, Vol. 28, pp. 3267–3280.

24. Feraboli, P, et al. - *LS-DYNA MAT54 modeling of the axial crushing of a composite tape sinusoidal specimen.* Composites Part A: Applied Science and Manufacturing, 2011, Vol. 42, pp. 1809-1825.

25. *Thomson, R,* Joosten, MW, et al. *Experimental evaluation of the crush energy absorption of triggered composite sandwich panels under quasi-static edgewise compressive loading.* Composites Part A: Applied Sciences and Manufacturing, 2010, Vol. 41, pp. 1099-1106.

26. Waimer, M, Siemann, MH and Feser, T. *Simulation of CFRP components subjected to dynamic crash loads.* International Journal of Impact Engineering, 2017, Vol. 101, pp. 115-131.

27. David, M. *Experimental and Numerical Investigation of Polymer Composite Energy Absorbers under Dynamic Loading.* Institute of Aircraft Design, University of Stuttgart. Stuttgart, 2014. PhD Thesis.

28. US National Highway Safety Administration. Standard No. 208; Occupant crash protection. Washington DC, USA : US Department of Transportation.

29. Euro NCAP. Lexus IS 300h - Frontal Crash Test 2013 - after Crash. [Online] [Cited: September 28, 2020.] https://euroncap.newsmarket.com/multimedia/images-and-videos/lexus-is-300h---frontal-crash-test-2013---after-crash/a/48294ce0-1680-463f-a98a-2c592d0e7189.

30. Farley, G. L. and Jones, R. M. *Energy-absorption capability of composite tubes and beams.* NASA Technical Publications, 1989. pp. 1-248. TM 101634.

31. Hull, D. *A unified approach to progressive crushing of fibre-reinforced.* 1991, Composites Science and Technology, Vol. 40 (4), pp. 377-421.

32. Allix, O and Ladevèze, P. *Interlaminar interface modelling for the prediction of delamination.* 1992, Composite Structures, Vol. 22 (4), pp. 235-242.

33. Mamalis, A.G., et al. *Analysis of failure mechanisms observed in axial collapse of thin-walled circular.* 1996, Thin-walled Structures, Vol. 24 (4), pp. 335-352.

34. Brown, R.T. *Design and manufacturing of 3-D braided preforms.* Philadelphia, USA, 1991. Proceedings from Fifth Textile Structural Composites Symposium.

35. Ren, Y, Jiang, H and Liu, Z. *Evaluation of double- and triple-coupled triggering mechanisms to improve crashworthiness of composite tubes.* 2019, International Journal of Mechanical Sciences, Vols. 157-158, pp. 1-12.

36. Lau, S.T.W., Said, M.R. and Yaakob, M.Y. *On the effect of geometrical designs and failure modes in composite axial crushing: A literature review.* 2012, Composite Structures, Vol. 94, pp. 803-812.

37. Kim, J.S., Yoon, H.J. and Shin, K.B. *A study on crushing behaviors of composite circular tubes with different reinforcing fibers.* 2011, International Journal of Impact Engineering, Vol. 38 (4), pp. 198-207.

38. Palanivelu, S, et al. *Experimental study on the axial crushing behaviour of pultruded composite tubes.* 2010, Polymer Testing, pp. 224-234.

39. Waimer, M, et al. *Contribution to an improved crash design for a composite transport aircraft fuselage—development of a kinematics model and an experimental component test setup.* 2013, CEAS Aeronautical Journal, Vol. 4 (3), pp. 265-275.

40. Engineering Networl. Carbon Fiber Angles. [Online] [Cited: October 22, 2020.] https://www.engnetglobal.com/c/c.aspx/COM090/productdetail/carbon-fiber-angles.

41. Feraboli, P. *Development of a modified flat-plate test specimen and fixture for composite materials crush energy absorption.* Journal of Composite Materials, 2009, Journal of Composite Materials, Vol. 43, pp. 1967-1990.

42. Bolukbasi, A.O. and Laananen, D.H. *Energy Absorption in Composite Stiffeners.* 1995, Composites, Vol. 26 (4), pp. 291-301.

43. Daniel, L, Hogg, P.J. and Curtis, P.T. *The relative effects of through-thickness properties and fibre orientation on energy absorption by continuous fibre composites.* 1999, Composites. Part B: Engineering, Vol. 30 (3), pp. 257-266.

44. Hogg, P.J. and Savona, S.C. *Investigation of plate geometry on the crushing of flat composite plates.* 2006, Composites Science and Technology, Vol. 66 (11), pp. 1636-1650.

45. Jacob, G.C., et al. *New test method for determining energy absorption mechanisms in polymer composite plates.* 2004, Polymer Composites, Vol. 24 (6), pp. 706-715.

46. Jacob, G.C., et al. *Crashworthiness of Automotive Composite Material Systems.* 2004, Journal of Applied Polymer Science, Vol. 92 (5), pp. 3218-3225.

47. Barnes, G. *Composite Crush Coupon Testing.* Santa Monica, California, USA. 2005. Proceedings of the 49th MIL-HDBK-17 Coordination Meeting - Crashworthiness Working Group.

48. Babaei, I, et al. *Newly developed anti-buckling fixture to assess the in-plane crashworthiness of flat composite specimens.* 2020, Applied Sciences.

49. Bru, T, et al. *Development of a test method for evaluating the crushing behaviour of unidirectional laminates.* 2017, Journal of Composite Materials, Vol. 51 (29), pp. 4041-4051.

50. Dalli, D, et al. *Assessing the current modelling approach for predicting the crashworthiness of Formula One composite structures.* 2020, Composites. Part B: Engineering, Vol. 201.

51. Catalanotti, G. *On the generation of RVE-based models of composites reinforced.* 2016, Composite Structures, Vol. 138, pp. 84-95.

52. McCarthy, C.T. and Vaughan, T.J. *A combined experimental-numerical approach for generating statistically equivalent fibre distributions for high strength laminated composite materials.* 2010, Composites Science and Technology, Vol. 70 (2), pp. 291-297.

53. Trias Mansilla, D. *Analysis and Simulation of Transverse Random Fracture of Long Fibre Reinforced Composites.* Universitat de Girona, 2005. PhD Thesis.

54. Vaughan, T.J. and McCarthy, C.T. *Micromechanical modelling of the transverse damage behaviour in fibre reinforced composites.* 2011, Composites Science and Technology, Vol. 71 (3), pp. 388 - 396.

55. Abdin, Y, et al. *Mean-field based micro-mechanical modelling of short wavy fiber reinforced composites.* 2016, Composites. Part A: Applied Science and Manufacturing, Vol. 91 (2), pp. 472-483.

56. Tabiei, A and Chen, Q. *Micromechanics Based Composite Material Model for Impact and Crashworthiness Explicit Finite Element Simulation.* Detroit, Michigan, USA. 2000. 6th International LS-DYNA Conference.

57. Tabiei, A and Babu, S.A. *A strain-rate dependent micro-mechanical model with progressive post-failure behavior for predicting impact response of unidirectional composite laminates.* 2009, Composite Structures, Vol. 88 (1), pp. 65-82.

58. Li, X and Liu, D. *Zigzag theory for composite laminates.* Michigan, USA. 1995, American Institute of Aeronautics and Astronautics Journal, Vol. 33 (6), pp. 1163-1165.

59. Carrera, E and Cinefra, M. *Finite Element Analysis of Structures Through Unified Formulation.* John Wiley & Sons, Inc., 2014. ISBN: : 1-119-94121-0.

60. Hashin, Z. *Failure criteria for unidirectional fiber composites.* June 1980, Journal of Applied Mechanics, Vol. 47 (2), pp. 329-334.

61. Puck, A and Schürmann, H. *Failure analysis of FRP laminates by means of physically based phenomenological models.* July 1998, Composites Science and Technology, Vol. 58 (7), pp. 1045-1067.

62. Ladeveze, P and LeDantec, E. *Damage modelling of the elementary ply for laminated composites.* 1992, Composites Science and Technology, Vol. 43 (3), pp. 257-267.

63. Johnson, A.F., Pickett, A.K. and Rozycki, P. *Computational methods for predicting impact damage in composite structures.* 2001, Composites Science and Technology, Vol. 61 (15), pp. 2183-2192.

64. Farley, G.L. and Jones, R.M. *Prediction of the Energy-Absorption Capability of Composite Tubes.* 1992, Journal of Composite Materials, Vol. 26 (3), pp. 388-404.

65. Morthorst, M and Horst, P. *Crushing of conical composites shells: a numerical analysis of the governing factors.* 2006, Aerospace Science and Technology, Vol. 10 (2), pp. 127-135.

66. Kim, J.K. and Sham, M.L. *Impact and delamination failure of woven-fabric composites.* 2000, Composites Science and Technology, Vol. 60 (5), pp. 745-761.

67. Meyer, C.S., et al. *Mesoscale ballistic damage mechanisms of a single-layer woven glass/epoxy composite.* 2018, International Journal of Impact Engineering, Vol. 113, pp. 118-131.

68. Kinvi-Dossou, G, et al. *A mesoscale modelling approach of glass fibre/Elium acrylic woven laminates for low velocity impact simulation.* 2020, Composite Structures, Vol. 252.

69. Srivastava, C. *Multiscale Modeling for Impact Simulations of Composite Aero-Structures.* Berlin, Germany, May 03, 2018. Presentation at ICONIC Meeting.

70. CMH-17-3G. *Composite materials handbook.* SAE International, 2012. Volume 3 of 6.

71. Walker, T.H., et al. *Tension fracture of laminates for transport fuselage. Part I: material screening.* Lake Tahoe, Nevada, USA, 1991. Proceedings of the 9th DoD/NASA/FAA conference on fibrous composites in structural design. Vol. II. pp 747-787.

72. Chang, F.K. and Chang, K.Y. *A Progressive Damage Model for Laminated Composites Containing Stress Concentrations.* September 1, 1987, Journal of Composite Materials, Vol. 21 (9), pp. 834-855.

73. Wolfe, W.E. and Butalia, T.S. *A strain-energy based failure criterion for non-linear analysis of composite laminates subjected to biaxial loading.* 1998, Composites Science and Technology, Vol. 58 (7), pp. 1107-1125.

74. Mahe, M, et al. *Evaluation of finite element modelling methodologie for the design of crashworthy composite commercial airraft fuselage.* Yokohama, Japan, 2004. 24th International Congress of the Aeronautical Sciences.

75. Commercial aircraft - design for crash survivability | Project FP4 CORDIS . [Online] European Commission, 2000. https://cordis.europa.eu/project/id/BRPR960207.

76. Orifici, A.C., Herszberg, I and Thomson, R.S. *Review of methodologies for composite material modelling incorporating failure.* 2008, Composite Structures, Vol. 86 (1), pp. 194-210.

77. Talreja, R. *A continuum mechanics characterization of damage in composite materials.* 1985, Proceedings of the Royal Society of London. Series A: Mathematica, Physical and Engineering Sciences, Vol. 399 (1817), pp. 195-216.

78. Talreja, R. *Damage development in composites: Mechanisms and modelling.* 1989, The Journal of Strain Analysis for Engineering Design, Vol. 24 (4), pp. 215-222.

79. Multiscale Modeling of Composites. [book auth.] J Aboudi, S.M. Arnold and B.A. Bednarcyk. *Micromechanics of Composite Materials - A Generalized Multiscale Analysis Approach.* Oxford, UK : Elsevier, 2013, Vol. 1, pp. 447-460.

80. Laurin, F, et al. *A multiscale hybrid approach for damage and final failure predictions of composite structures.* 20-21. Journal of Composite Materials, 2012, Vol. 47, pp. 2713–2747.

81. Ivančević, D and Smojver, I. *Explicit multiscale modelling of impact damage on laminated composites – Part II: Multiscale analyses.* Elsevier, 2016, Composite Structures, Vol. 145, pp. 259-268.

82. Boria, S, Obradovic, J and Belingardi, G. *Experimental and numerical investigations of the impact behaviour of composite frontal crash structures.* Composites Part B: Engineering, 2015, Composites. Part B: Engineering, Vol. 79, pp. 20-27.

83. Johnson, A, Toso-Pentecôte, N and Kilchert, S. *Validation of damage modelling in composite fuselage structures under high velocity impact.* 2013, CEAS Aeronautical Journal, Vol. 4 (3), pp. 253-264.

84. Patel, S, Vusa, V.R. and Soares, C.G. *Crashworthiness analysis of polymer composites under axial and oblique impact loading.* Elsevier, 2019, International Journal of Mechanical Sciences, Vol. 156, pp. 221–234.

85. ASTM. *Standard Test Method for Determining the Compressive Properties of Polymer Matrix Composite Laminates Using a Combined Loading Compression (CLC) Test Fixture.* West Conshohocken, PA, USA : ASTM International, 2016. ASTM D6641 / D6641M - 16e1.

86. Kaddour, A.S., et al. *The world-wide failure exercises: how can composites design and manufacture communities build their strength.* Sevilla, Spain : QinetiQ Ltd 2014, 22-26 June 2014. ECCM16 - 16th European conference on composite materials.

87. Johnson, A.F. and David, M. *Failure mechanisms in energy-absorbing composite structures.* Abingdon, England : Taylor & Francis Group, 11 07, 2010, Philosophical Magazine , Vol. 90 (31-32), pp. 4245-2461.

88. Garattoni, F. *Crashworthiness and composite materials: development of an experimental test method for the energy absorption determination and implementation of the relative numerical model.* Bologna, Italy : s.n., 2011. PhD Thesis.

89. Boria, S and Belingardi, G. *Numerical investigation of energy absorbers in composite materials for automotive applications.* Taylor & Francis, Jan 09, 2012, International Journal of Crashworthiness, Vol. 17 (4), pp. 345-356.

90. Fleming, D.C. *Modelling composite crushing initiation using a cohesive element formulation.* 2011, International Journal of Crashworthiness, Vol. 16 (5), pp. 475-485.

91. Joosten, M.W., et al. *Experimental and numerical investigation of the crushing response of an open section composite energy absorbing element.* Elsevier, 2011, Composite Structures, Vol. 93, pp. 682-689.

92. Tan, W, Falzon, B.G. and Price, M. *Predicting the crushing behaviour of composite material using high-fidelity finite element modelling.* Taylor & Francis, 2015, International Journal of Crashworthiness, Vol. 20 (1), pp. 60-77.

93. Chiu, L.N.S., et al. *Finite element modelling of composite structures under crushing load.* Elsevier, 2015, Composite Structures, Vol. 131, pp. 215-228.

94. Reuter, C, Sauerland, K.H. and Tröster, T. *Experimental and numerical crushing analysis of circular CFRP tubes under axial impact loading.* Elsevier, 2017, Composite Structures, Vol. 174, pp. 33-44.

95. Babaei, I. *Structural testing of composite crash structures.* DIMEAS, Politecnico di Torino. Turin, Italy : s.n., 2021. PhD Thesis.

96. Ueda, M, Anzai, S and Kubo, T. *Progressive crushing of a unidirectional CFRP plate with V-shaped trigger.* Taylor & Francis, Feburary 2014, Advanced Composite Materials, Vol. 24 (1), pp. 85-95.

97. Bussadori, B.P., Schuffenhauer, K and Scattina, A. *Modelling of CFRP crushing structures in explicit crash analysis.* Elsevier, January 16, 2014, Composites: Part B, Vol. 60, pp. 725-735.

98. Garg, R, et al. *Predicting composite component behaviour using element level crashworthiness tests, FEA and parametric optimization.* MDPI, October 11, 2020, Materials, Vol. 13 (20), pp. 4501-4520.

99. Microtex Composites. GG 630 T . *Microtex Composites.* [Online] [Cited: January 29, 2019.] https://microtexcomposites.com/en/p/gg-630-t/.

100. Johnson, G.R. and Cook, W.H. *Fracture characteristics of three metals subjected to various strains, strain rates, temperatures and pressures.* Pergamon Press Ltd., 1985, Engineering Fracture Mechanics, Vol. 21 (1), pp. 31-48.

101. Murugesan, M and Jung, D.W. *Johnson Cook Material and Failure Model Parameters Estimation of AISI-1045 Medium Carbon Steel for Metal Forming Applications.* MDPI, February 18, 2019, Materials, Vol. 12 (4609), pp. 609-626.

102. Altair Engineering Inc. *Radioss Reference Guide.* Altair, 2017. pp. 195-212; 218-227; 277-288; 337-342; 576-599; 651-655; 663-664; 854-858; 1062-1065; 1078-1088; 1145-1147, Reference Manual.

103. Wang, W, et al. *Strain Rate Effect on Tensile Behavior for a High Specific Strength Steel: From Quasi-Static to Intermediate Strain Rates.* MDPI, December 29, 2017, Metals, Vol. 8 (1), pp. 11-24.

104. Total Materia. C40 Steel Mechanical Properties. *Total Materia.* [Online] [Cited: 17 February, 2019.] https://search.totalmateria.com/MaterialDetails/MaterialDetail?vkKey=1320394&keyNum=502&type=12&599 hs=1.

105. Tsai, S.W. and Wu, E.M. *A General Theory of Strength for Anisotropic Materials.* Air Force Systems Command, Air Force Materials Laboratory. Ohio, USA : Washington University, August 1972. Technical Report AFML-TR-71-12.

106. Singh, V. *Literature survey of strain rate effects on composites.* RISE Research Institutes of Sweden. July 2019. TR18-001.

107. Jacob, G.C., et al. *Energy Absorption in Polymer Composites for Automotive Crashworthiness.* 2002, Journal of Composite Materials, Vol. 36 (7), pp. 813-850.

108. Savage, G.M. *Safety and survivability in Formula One motor racing. Metals and Materials.* 1992, Metals and Materials, Vol. 8 (3), p. 147.

109. Ciardiello, R, Drzal, L.T. and Belingardi, G. *Effects of carbon black and graphene nano-platelet fillers on the mechanical properties of syntactic foam.* 2017, Composite Structures, Vol. 178, pp. 9-19.

110. Oral, I, Guzel, H and Ahmetli, G. *Determining the mechanical properties of epoxy resin (DGEBA) composites by ultrasonic velocity measurement.* 2013, Journal of Applied Polymer Science, Vol. 127, pp. 1667-1675.

111. Overview of material for Epoxy Adhesive. *MatWeb.* [Online] [Cited: November 1, 2019.] http://www.matweb.com/search/datasheettext.aspx?matguid=c1ec1ad603c74f628578663aaf44f261.

112. Schueler, D, Toso-Pentecote, N and Voggenreiter, H. *Effects of static preloads on the high velocity impact repose of composite plates.* 2016, Composites Structures, Vol. 153, pp. 549-556.

113. Altair Engineering, Inc. *Introduction to RADIOSS for Impact Analysis: Interface (Contact) Modeling.* Turin, Italy : Altair Engineering, Inc., 2018. Training Presentation.

114. Schön, J. *Coefficient of friction for aluminum in contact with a carbon fiber epoxy composite.* Elsevier, May 2004, Tribology International, Vol. 37 (5), pp. 395-404.

115. Dhieb, H, et al. *Surface damage of unidirectional carbon fiber reinforced epoxy composites under reciprocating sliding in ambient air.* Elsevier, October 24, 2011, Composites Science and Technology, Vol. 71 (15), pp. 1769-1776.

116. Zhun, N.W., et al. *Tribological properties of short carbon fibers reinforced epoxy composites.* Springer, April 01, 2014, Friction, Vol. 2, pp. 226-239.

117. Mamalis, A.G., et al. *The static and dynamic axial crumbling of thin-walled fibreglass composite square tubes.* 1997, Composites Part B: Engineering, Vol. 28 (4), pp. 439-451.

118. Chowdhury, M.A., et al. *Experimental investigation of friction coefficient and wear rate of composite materials sliding smooth and rough mild steel counterfaces.* 2013, Tribology in industry, Vol. 35 (4), pp. 286-296.

119. Nuruzzaman, D.M., et al. *Experimental investigation on friction coefficient of composite materials sliding against SS 201 and SS 301 counterfaces.* 2015, Procedia Engineering, Vol. 105, pp. 858-864.

120. Obradovic, J. *Innovative developments in lightweight design of car body structure.* DIMEAS, Politecnico di Torino. Turin, Italy : s.n., 2011. pp. 125-150, PhD Thesis.

121. Berg, C.A., Batra, S and Tirosh, J. *Friction and Wear of Graphite Fiber Composites.* May 16, 1972, JOURNAL OF RESEARCH of the Notional Bureau of Standards-C. Engineering and Instrumentation, Vol. 76C (1-2), pp. 41-52.

122. Box, G.E.P. and Wilson, K.B. *On the Experimental Attainment of Optimum Conditions.* 1951, Journal of the Royal Statistical Society. Series B (Methodological), Vol. 13 (1), pp. 1-45.

123. Wang, G.G., Dong, Z and Aitchison, P. *Adaptive Response Surface Method – A Global Optimization Scheme for Approximation-based Design Problems.* Taylor & Francis Group, 2001, Engineering Optimization, Vol. 33 (6), pp. 707-733.

124. Shi, L, Yang, R.J. and Zhu, P. *An adaptive response surface method for crashworthiness optimization.* September 06, 2012, Engineering Optimization, Vol. 45 (11), pp. 1365-1377.

125. Keshtegar, B, et al. *An adaptive response surface method and Gaussian global-best harmony search algorithm for optimization of aircraft stiffened panels.* Elsevier, February 15, 2018, Applied Soft Computing, Vol. 66, pp. 196-207.

126. Altair Engineering Inc. *Altair HyperStudy 2020: User Guide.* Altair Engineering Inc., 2020. Reference Manual.

127. Mallawaarachchi , V. Introduction to Genetic Algorithms — Including Example Code. *www.towardsdatascience.com.* [Online] July 08, 2017. [Cited: February 01, 2021.] https://towardsdatascience.com/introduction-to-genetic-algorithms-including-example-code-e396e98d8bf3.

128. Altair Engineering, Inc. Introduction To Radioss for Impact Analysis: Interface (Contact) Modeling. [Presentation]. Turin, Italy : s.n., 2018.

129. Morton, J and Lavoie, J.A. *Design and Application of a Quasistatic Crush Test Fixture for Investigating Scale Effects in Energy Absorbing Composite Plates.* Deptartment of Engineering Science and Mechanics, Virginia Polytechnic Inst. and State University. Blacksburg : NASA Langley Research Center, 1993. M.S. Thesis.

130. Mouillet, J.B. and Fokin, D. Validation of Delamination Criteria. [Training Presentation]. Turin, Italy : Altair Engineering Inc., 2018.

131. Milan, R, et al. *Development of composite energy absorber.* ScienceDirect, 2014, Procedia Engineering, Vol. 96, pp. 392 – 399.

9. Appendix

9.1. Comparison between calibrated and uncalibrated flat-plate macroscale model

The approach mentioned in section 5 was able to calibrate the material card with a good degree of accuracy and this calibrated model, expectedly, showed marked improvement over the uncalibrated model, which used default values for the calibrated parameters. Figure **9.1** shows the comparison of the calibrated model with the uncalibrated model in modeling the experimental force-displacement results. Even though, the uncalibrated model resulted in damage initiation from the bottom, after 10 mm of displacement, the composite plate started getting crushed from the top, unlike what was observed in the physical flat-plate. The switch in the sides of the damage can also be seen in the graph as an increase in the force at 10 mm.

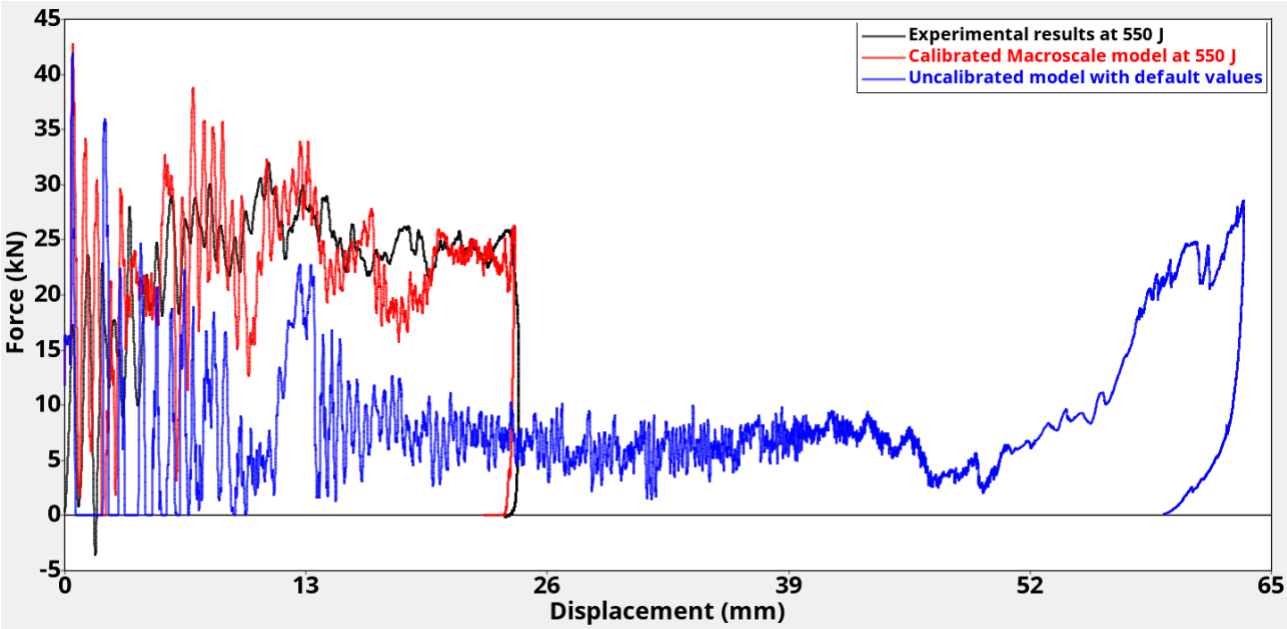

Figure 9.1: *Force-displacement data comparison of calibrated and uncalibrated flat-plate macroscale model with experimental results*

9.2. Impact attenuator force-displacement results at all impact velocities

This section presents the comparison between experimental and numerical (macroscale, mesoscale with AMS activation and mesoscale without AMS activation) models for the impact attenuator at three impact velocities: 7.101, 7.77 and 8.04 m/s. The general trend, as mentioned in section 6.3, is the same across the velocities and models: stepwise increase in mean crush force over three sections with variability of results decreasing from the mesoscale model with AMS activation to the mesoscale model without AMS activation to the macroscale models, which showed the lowest variability in mean crush force. A detailed discussion of observations from these graphs can be found in section 6.3.

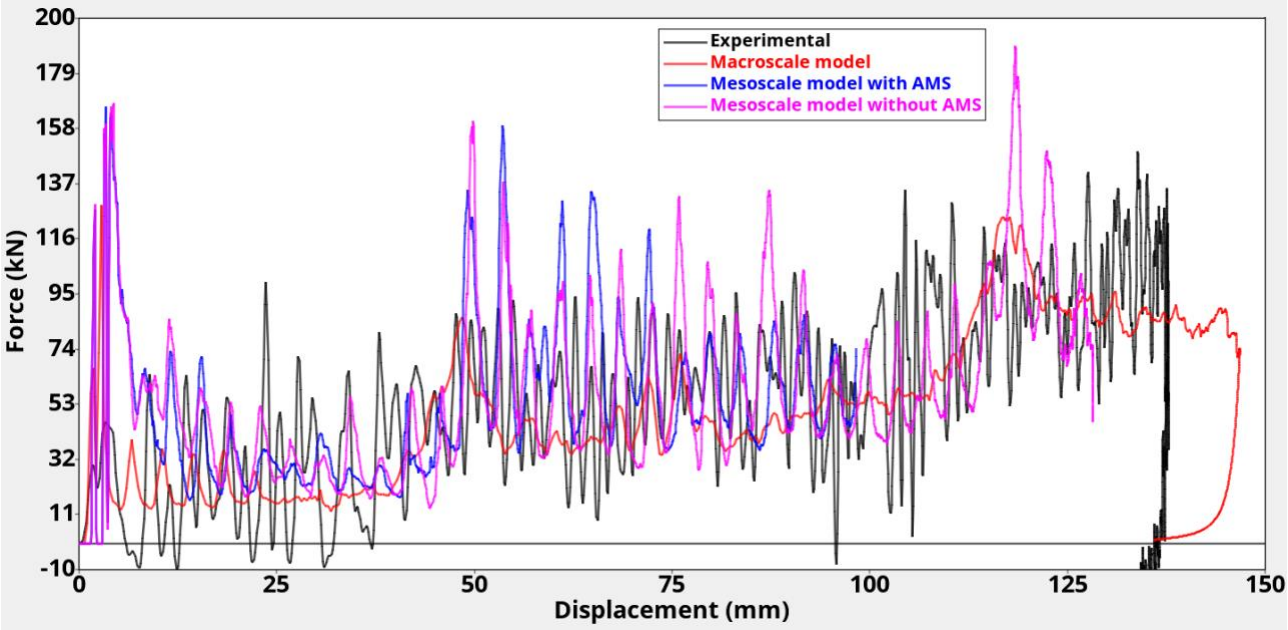

Figure 9.2: *Force-displacement result comparison at 7.101 m/s impact velocity*

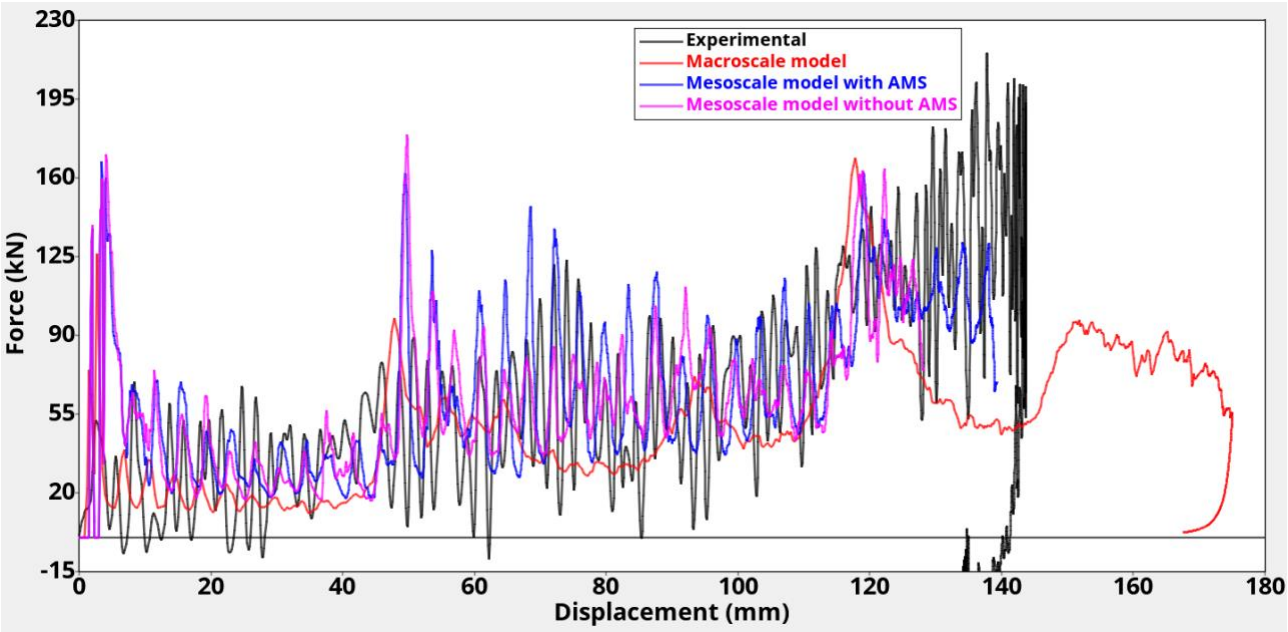

Figure 9.3: *Force-displacement result comparison at 7.77 m/s impact velocity*

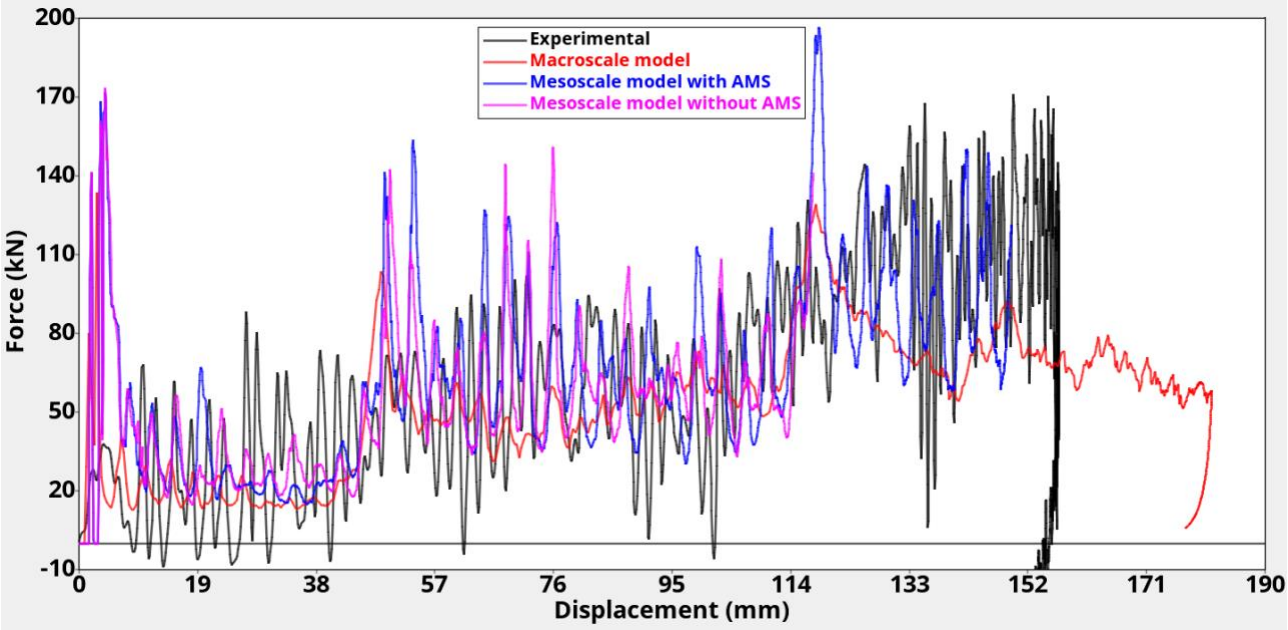

Figure 9.4: *Force-displacement result comparison at 8.04 m/s impact velocity*